

**ÇUKUROVA UNIVERSITY
INSTITUTE OF NATURAL AND APPLIED SCIENCES**

PhD THESIS

Hulusi DELİBAŞ

**DEVELOPMENT OF A NEW SHEET METAL FORMING
TECHNIQUE USING LOW MELTING ALLOY 3D PRINTERS**

DEPARTMENT OF MECHANICAL ENGINEERING

ADANA-2022

ABSTRACT

PhD THESIS

DEVELOPMENT OF A NEW SHEET METAL FORMING TECHNIQUE USING LOW MELTING ALLOY 3D PRINTERS

Hulusi DELİBAŞ

ÇUKUROVA UNIVERSITY
INSTITUTE OF NATURAL AND APPLIED SCIENCES
DEPARTMENT OF MECHANICAL ENGINEERING

Supervisor : Prof. Dr. Necdet GEREN
Year: 2022, Page: 137
Jury : Prof. Dr. Necdet GEREN
: Prof. Dr. Melih BAYRAMOĞLU
: Prof. Dr. Hakan YAVUZ
: Prof. Dr. Uğur EŞME
: Assoc. Prof. Dr. Erinc ULUDAMAR

The objective of this study is to produce a sheet metal forming mold made from the low melting point Bi58Sn42 alloy which proved to have sufficient strength in sheet metal forming operations by using open-source desktop type fused deposition modelling (FDM) 3-Dimensional (3D) printer and to evaluate the performance of the 3D printed mold for low volume sheet metal parts production. Thus, it was aimed to develop fast and inexpensive tooling methodology for small sized batch production. In this context, initially the 3D printing experiments were performed to produce the sheet metal forming mold. The encountered problems during the performed 3D printing experiments were analyzed. Accordingly, both tunings in print settings (extrusion temperature, extrusion multiplier, printing speed, infill rate, and etc.) and customizations on the extruder of the available FDM type 3D printer were made to print the Bi58Sn42 alloy properly. Subsequently, the performance of the 3D printed mold was evaluated according to the dimensional change on it during the performed pressing operations. Results showed that the 3D printed mold was rigid enough for low volume sheet metal parts production.

Key Words: Bi58Sn42 alloy, customization on extruder, FDM, sheet metal forming mold, small sized batch production

ÖZ

DOKTORA TEZİ

**YENİ BİR SAC METAL ŞEKLİLENDİRME TEKNİĞİNİN DÜŞÜK
ERİME NOKTASINA SAHİP ALAŞIM VE 3B YAZICI KULLANARAK
GELİŞTİRİLMESİ**

Hulusi DELİBAŞ

**ÇUKUROVA ÜNİVERSİTESİ
FEN BİLİMLERİ ENSTİTÜSÜ
MAKİNE MÜHENDİSLİĞİ ANABİLİM DALI**

Danışman : Prof. Dr. Necdet GEREN
Yıl:2022, Sayfa: 137
Juri : Prof. Dr. Necdet GEREN
: Prof. Dr. Melih BAYRAMOĞLU
: Prof. Dr. Hakan YAVUZ
: Prof. Dr. Uğur EŞME
: Doç. Dr. Erine ULUDAMAR

Bu çalışmanın amacı, sac şekillendirme işlemlerinde yeterli dayanıma sahip olduğu kanıtlanmış düşük ergime noktalı Bi58Sn42 alaşımından, açık kaynaklı masaüstü eriyik biriktirmeli modelleme (FDM) tipi 3 boyutlu (3B) yazıcı kullanarak sac şekillendirme kalıbı üretmek ve düşük hacimli sac parça üretimi için 3B baskılı kalıbın performansını değerlendirmektir. Böylece küçük boyutlu parti üretimi için hızlı ve ucuz kalıplama metodolojisinin geliştirilmesi hedeflenmiştir. Bu kapsamda öncelikle sac şekillendirme kalıbının üretilmesi için 3 boyutlu baskı deneyleri yapılmıştır. Gerçekleştirilen 3B baskı deneyleri sırasında karşılaşılan sorunlar analiz edilmiştir. Buna göre Bi58Sn42 alaşımını düzgün bir şekilde basmak için hem baskı ayarlarında (ekstrüzyon sıcaklığı ve çarpanı, baskı hızı, doluluk oranı vb.) ayarlamalar hem de mevcut FDM tipi 3B yazıcının ekstrüderinde özelleştirmeler yapılmıştır. Daha sonra gerçekleştirilen presleme işlemleri sırasında 3B baskılı kalıbın üzerindeki boyutsal değişime göre performansı değerlendirilmiştir. Sonuçlar, 3B baskılı kalıbın düşük hacimli sac parça üretimi için yeterince dayanıklı olduğunu göstermiştir.

Anahtar Kelimeler: Bi58Sn42 alaşımı, ekstrüderde özelleştirme, FDM, sac şekillendirme kalıbı, küçük boyutlu toplu üretim

EXTENDED ABSTRACT

Additive manufacturing (AM) is an alternative approach to manufacture an object. The part is built by adding layer upon layer depending on the part's computer-aided design (CAD) data. The bonding between the adjacent layers can be obtained by partial melting, photopolymerization, liquid binder and sintering according to the utilized AM process. The most commonly used AM materials are thermoplastic polymers, metals, ceramics and biochemicals. Application areas of AM involves aerospace, automotive and medical industries. While each lathe makes limited job (drilling, turning, milling and etc.) in traditional manufacturing, AM makes the jobs that are machined on different machines at once. Therefore, labor cost, manufacturing cost, the need for large work area and product lead time decreases in AM. Using AM makes companies more competitive and efficient in the global market, especially in sectors that require innovation, where parts with high performance (low weight and high strength) and complex geometries are used. As the objects are built layer by layer in AM, complex shapes with internal intricate features can be produced easily in contrast to traditional manufacturing. Even traditional manufacturing methods may be insufficient according to the complexity of the part. AM is also suitable for small sized batch production or flexible manufacturing since the finished part is manufactured directly just in time. There is no need to invest tooling or any jigs and fixtures.

Sheet metal forming is a manufacturing process that is commonly used for producing shaped components. It plays an important role in aerospace, automotive, construction and manufacturing industries. Conventional sheet metal forming process is not applicable for the small sized batch production due to the high cost. Furthermore, dies are machined in computer numerical control (CNC) and lead times increase because of backlog.

In this study, it was proposed to produce sheet metal forming mold using AM process for low volume sheet metal parts production. Thus, it was aimed to

quick response to customized demands with cost-effective for small sized batch production.

There are different AM processes available. Among these, fused deposition modelling (FDM) process was preferred as it is both economical and allows customization and the use of different materials.

The mold materials used in the conventional sheet metal forming process are highly durable and costly. But this high cost is amortized by the high production volume. In this study, low melting point Bi58SSn42 eutectic alloy was selected as mold material for the following reasons:

- FDM has limited heating power. Therefore, direct 3D printing of high melting point materials is not possible.
- In the studies conducted by the automotive companies and researchers, it was seen that the performance of the molds produced by casting from Bi58Sn 42 alloy was sufficient for low volume sheet metal part production.
- Although the Bi58Sn42 alloy's cost in filament form is high, its cost can be compensated by repeated uses since the alloy is recyclable.

It has been observed in the literature that high-strength materials such as titanium and stainless steel are 3D printed in two ways. The first one is using industrial type 3D printers such as SLS, EBM, and etc. where expensive equipment is used. The latter is to develop a composite filament composed of particles of these materials blended with polymer binders then printing of the developed composite filaments in FDM type 3D printer. However, in order to remove the polymer binders and strengthen the bond between the metal particles, a part printed in this way must undergo post-processing such as debinding and sintering which prolongs the production process. Therefore, in this study, it was aimed to use the mold produced in the 3D printer directly without being subjected to any post-processing.

In this study, initially, sheet metal forming molds were produced then the performance of the 3D printed mold was evaluated according to the dimensional change during the performed pressing operations for low volume sheet metal parts production. Both 0.2 mm and 0.3 mm thick aluminum 8006 sheets were pressed 101 times.

Comprehensive 3D printing experiments were performed to print the sheet metal forming mold. The 3D printing experiments were commenced to print a uniform line without any blob or dash line formation by tuning extrusion temperature (ET), extrusion multiplier (EM) and printing speed (PS) in the standard (unmodified) extruder of the available FDM type 3D printer. Later, single and multi-layered shell structures were printed using the print settings that gave the optimum result during the performed line printing experiments. The best dimensional quality was obtained in vase mode for layer thickness of 0.2 mm, printing speed of 100 mm/min, extrusion multiplier of 1, extrusion temperature of 160 °C, platform temperature of 75 °C, and road width of 0.4 mm during the performed shell printing experiments. After printing a shell structure that consists of 125 layers successfully, infill printing experiments were commenced using the print settings that gave the optimum result during the performed shell structure printing experiments. However, the desired result was not achieved in the implemented infill printing experiments. There was fluctuation in the extruded road's size due to the acceleration and deceleration during the extruder's sharp turning movements. Accordingly, this situation affected the extruded road's size in the remaining section of the part. Also, dash lines were observed on the printed geometries during the performed repetitive experiments using the same print settings. It was inferred that the hot zone (melt chamber volume) of the standard extruder was insufficient. For this reason, volume of the hot zone on the available extruder was enlarged and experiments were continued with customized extruder.

As in the standard extruder, the same parameters (ET, EM and PS) were optimized to print an uninterrupted uniform line in the modified extruder. Later, the experiments were continued to print a solid single-layer square object. Fluctuations

were seen on extruded road's size during the extruder's sharp turning movements in the performed infill printing experiments. Moreover, it was observed that the deposited road could not maintain its shape. For these reasons, dimensional accuracy of the printed sample was adversely affected. Therefore, sample geometry was altered to circle with concentric infill pattern from the square with rectilinear infill pattern to minimize the extruder's sharp turning movements. And consequently, the single-layer solid circular sample with infill rate of 97.451 % was obtained for ET of 170 °C, platform temperature (PT) of 75 °C, layer thickness (LT) of 0.2 mm, PS of 100 mm/min, EM of 2. Subsequently, the printing experiments were carried on for multi-layered solid hemisphere production and solid hemisphere sample with a diameter of 10.68 mm printed in start-stop mode using PS of 500 mm/min, LT of 0.2 mm, PT of 75°C, ET of 170 °C, IR of 50%, EM of 1. On the other hand, the female of this 3D printed solid hemisphere mold was produced by casting due to the FDM hardware's low reliability (no pressure drop feedback in the extruder) and poor material characteristics of Bi58Sn42 alloy (eutectic phase and low viscosity). Then pressing operations were carried out to shape 0.2 mm and 0.3 mm thick AL 8006 sheets.

Deviation in 3D printed hemisphere mold's diameter was 0.14 mm after applying 101 pressing operations onto the 0.2 mm thick AL 8006 sheets. For 0.3 mm thick AL 8006 sheets, deviation in 3D printed hemisphere mold's diameter was 0.42 mm after applying 101 pressing operations. As a result, the performance of the 3D printed mold was sufficient for the low volume sheet metal parts production. Nevertheless, the applied method for the production of sheet metal forming mold was not found reliable due to the poor material characteristics of Bi58Sn42 alloy.

GENİŞLETİLMİŞ ÖZET

Katmanlı imalat (AM), bir nesneyi imal etmek için alternatif bir yaklaşımdır. Parça, parçanın bilgisayar destekli tasarım (CAD) verilerine bağlı olarak katman katman eklenerek oluşturulur. Bitişik katmanlar arasındaki bağ, kullanılan AM işlemine göre kısmi eritme, fotopolimerizasyon, sıvı bağlayıcı ve sinterleme ile elde edilebilir. En yaygın olarak kullanılan AM malzemeleri termoplastik polimerler, metaller, seramikler ve biyokimyasallardır. AM' in uygulama alanları havacılık, otomotiv ve tıp endüstrilerini içerir. Geleneksel imalatta her tezgâh sınırlı iş (delme, tornalama, frezeleme vb.) yaparken, AM farklı makinelerde işlenen işleri tek seferde yapar. Bu nedenle, AM' de işçilik maliyeti, üretim maliyeti, geniş çalışma alanı ihtiyacı ve ürün teslim süresi azalır. AM kullanımı, özellikle yenilikçilik gerektiren, yüksek performanslı (düşük ağırlık ve yüksek mukavemetli) ve karmaşık geometrilere sahip parçaların kullanıldığı sektörlerde, şirketleri küresel pazarda daha rekabetçi ve verimli hale getirir. Nesneler AM' de katman katman oluşturulduğundan, geleneksel üretimin aksine dahili karmaşık özelliklere sahip karmaşık şekiller kolayca üretilebilir. Parçanın karmaşıklığına göre geleneksel imalat yöntemleri yetersiz kalabilmektedir. AM, bitmiş parça doğrudan tam zamanında üretildiğinden, küçük boyutlu seri üretim veya esnek üretim için de uygundur. Alet veya herhangi bir aparat ve fiktür yatırımına gerek yoktur.

Sac metal şekillendirme, şekillendirilmiş bileşenler üretmek için yaygın olarak kullanılan bir üretim sürecidir. Havacılık, otomotiv, inşaat ve imalat endüstrilerinde önemli bir rol oynar. Küçük boyutlu seri üretimlerde yüksek maliyet nedeniyle geleneksel sac şekillendirme işlemi uygulanamamaktadır. Ayrıca, kalıplar bilgisayarlı sayısal kontrolde (CNC) işlenir ve iş yoğunluğu nedeniyle teslimat süreleri uzar.

Bu çalışmada, düşük hacimli sac parça üretimi için AM prosesi kullanılarak sac şekillendirme kalıbı üretilmesi önerilmiştir. Böylece küçük boyutlu parti üretimler için özel taleplere uygun maliyetli ve hızlı cevap verilmesi hedeflenmiştir.

Farklı AM prosesleri mevcuttur. Bunlar arasında hem ekonomik olması hem de özelleştirmeye ve farklı malzemelerin kullanımına olanak sağlaması nedeniyle eriyik biriktirmeli modelleme (FDM) işlemi tercih edilmiştir.

Geleneksel sac şekillendirme işleminde kullanılan kalıp malzemeleri oldukça dayanıklı ve maliyetlidir. Ancak bu yüksek maliyet, yüksek üretim hacmi ile kendini amorti etmektedir. Bu çalışmada, kalıp malzemesi olarak düşük erime noktalı Bi58Sn42 ötektik alaşımı aşağıdaki nedenlerle seçilmiştir:

- FDM'nin sınırlı ısıtma gücü vardır. Bu nedenle, yüksek erime noktalı malzemelerin doğrudan 3B baskısı mümkün değildir.
- Otomotiv firmaları ve araştırmacılar tarafından yapılan çalışmalarda Bi58Sn42 alaşımından döküm yapılarak üretilen kalıpların performansının düşük hacimli sac parça üretimi için yeterli olduğu görülmüştür.
- Bi58Sn42 alaşımının filament formundaki maliyeti yüksek olmasına rağmen, alaşım geri dönüştürülebilir olduğu için tekrarlanan kullanımlarla maliyeti telafi edilebilir.

Literatürde titanyum ve paslanmaz çelik gibi yüksek mukavemetli malzemelerin iki şekilde 3B olarak basıldığı gözlemlenmiştir. Birincisi, pahalı ekipmanların kullanıldığı SLS, EBM vb. endüstriyel tip 3B yazıcıların kullanılmasıdır. İkincisi, polimer bağlayıcılarla harmanlanmış bu malzemelerin parçacıklarından oluşan bir kompozit filament geliştirmek ve ardından geliştirilen kompozit filamentlerin FDM tipi 3B yazıcıda basılmasıdır. Ancak polimer bağlayıcıların uzaklaştırılması ve metal partiküller arasındaki bağın güçlendirilmesi için bu şekilde basılan bir parçanın, üretim sürecini uzatan debinding ve sinterleme gibi ardıl işlemlerden geçmesi gerekir. Bu nedenle bu çalışmada 3B yazıcıda üretilen

kalıbın herhangi bir ardıl işleme tabi tutulmadan direkt olarak kullanılması amaçlanmıştır.

Bu çalışmada, öncelikle sac şekillendirme kalıpları üretilmiş, daha sonra düşük hacimli sac parça üretimi için gerçekleştirilen pres işlemleri sırasında boyut değişimine göre 3B baskı kalıbın performansı değerlendirilmiştir. Hem 0,2 mm hem de 0,3 mm kalınlığında alüminyum 8006 levhalar 101 kez preslenmiştir.

Sac şekillendirme kalıbını basmak için kapsamlı 3B baskı deneyleri yapılmıştır. Mevcut FDM tipi 3B yazıcı' nın standart (değiştirilmemiş) ekstrüderinde ekstrüzyon sıcaklığı (ET), ekstrüzyon çarpanı (EM) ve baskı hızı (PS) ayarlanarak herhangi bir damla veya kesik çizgi oluşumu olmadan tek tip bir çizgi yazdırmak için 3B baskı deneyleri başlatılmıştır. Daha sonra gerçekleştirilen çizgi baskı deneyleri sırasında optimum sonucu veren baskı ayarları kullanılarak tek ve çok katmanlı kabuk yapıları basılmıştır. Gerçekleştirilen kabuk baskı deneyleri sırasında, en iyi boyutsal kalite, 0,2 mm katman kalınlığı, 100 mm/dk baskı hızı, 1 ekstrüzyon çarpanı, 160 °C ekstrüzyon sıcaklığı, 75 °C platform sıcaklığı ve 0,4 mm yol genişliği için vazo modunda elde edilmiştir. 125 katmandan oluşan bir kabuk yapısının başarılı bir şekilde yazdırılmasının ardından, yapılan kabuk yapı baskı deneyleri sırasında optimum sonucu veren baskı ayarları kullanılarak dolgu baskı denemelerine geçilmiştir. Ancak gerçekleştirilen dolgu baskı deneylerinde istenilen sonuca ulaşılamamıştır. Ekstrüderin keskin dönüş hareketleri sırasında hızlanma ve yavaşlama nedeniyle ekstrüde edilen eriyiğin boyutunda dalgalanma olmuştur. Bu durum, parçanın geri kalan kısmındaki ekstrüde edilen eriyik boyutunu da etkilemiştir. Ayrıca, aynı baskı ayarları kullanılarak gerçekleştirilen tekrarlı deneyler sırasında basılı geometriler üzerinde kesikli çizgiler gözlemlenmiştir. Dolayısıyla standart ekstrüderin sıcak bölgesinin (eriyik odası hacmi) yetersiz olduğu sonucuna varılmıştır. Bu nedenle mevcut ekstrüder üzerindeki sıcak bölgenin hacmi büyütülmüş ve özelleştirilmiş ekstrüder ile deneylere devam edilmiştir.

Standart ekstrüderde olduğu gibi, aynı parametreler (ET, EM ve PS), modifiye edilmiş ekstrüderde kesintisiz tek tip bir çizgi basmak için optimize

edilmiştir. Daha sonra, tek katmanlı bir kare nesneyi basmak için deneylere devam edilmiştir. Yapılan dolgu baskı deneylerinde ekstrüder'in keskin dönüş hareketleri sırasında ekstrüde edilen eriyiğin boyutunda dalgalanmalar görülmüştür. Ayrıca, ekstrüde edilen ergiyiğin şeklini koruyamadığı da gözlemlenmiştir. Buna bağlı olarak, basılan numunenin boyutsal hassasiyeti olumsuz etkilenmiştir. Bu nedenle, ekstrüder'in keskin dönüş hareketlerini en aza indirmek için numune geometrisi, doğrusal dolgu desenli kare'den eşmerkez dolgu desenli daire şeklinde değiştirilmiştir. Sonuç olarak, 170 °C' lik ET, 75 °C' lik platform sıcaklığı (PT), 0.2 mm' lik katman kalınlığı (LT), 2' lik EM ve 100 mm/dakika' lık PS için % 97.451 dolgu oranına sahip tek katmanlı katı dairesel numune elde edilmiştir. Ardından, çok katmanlı katı yarım küre üretimi için baskı deneyleri yapılmış ve 500 mm/dak PS, 0,2 mm LT, 75 °C PT, 170 °C ET, %50 IR ve 1 EM kullanılarak başla-dur modunda 10,68 mm çapında katı yarım küre numunesi basılmıştır. Öte yandan, bu 3B baskılı katı yarım küre kalıbının dışı, FDM donanımının düşük güvenilirliği (Ekstrüderde basınç düşüşü için geri besleme sistemi yok) ve Bi58Sn42 alaşımının zayıf malzeme karakteristik özelliklerinden dolayı (ötektik faz ve düşük viskozite) döküm yoluyla üretilmiştir. Daha sonra 0,2 mm ve 0,3 mm kalınlığındaki AL 8006 levhalara şekil vermek için presleme işlemleri yapılmıştır.

0,2 mm kalınlığındaki AL 8006 levhalara 101 presleme işlemi uygulandıktan sonra 3B baskılı yarım küre kalıbının çapındaki sapma 0,14 mm olmuştur. 0,3 mm kalınlığındaki AL 8006 levhalar için ise, 101 presleme işlemi uygulandıktan sonra 3B baskılı yarım küre kalıbın çapındaki sapma 0,42 mm olmuştur. Sonuç olarak, düşük hacimli sac parça üretimi için 3B baskılı kalıbın performansı yeterli görülmüştür. Bununla birlikte sac şekillendirme kalıbı üretimi için uygulanan yöntem, Bi58Sn42 alaşımının zayıf malzeme karakteristik özelliklerinden dolayı güvenilir bulunmamıştır.

ACKNOWLEDGMENT

Foremost, I would like to present my gratitude to my advisor, Prof. Dr. Necdet GEREN who always shared his knowledge and experience, guided my work with patience and kindness at every stage of the thesis, and never spared his help.

I am also thankful to thesis monitoring committee members, Prof.Dr. Melih BAYRAMOĞLU and Prof. Dr. Hakan YAVUZ who contributed with their evaluations and suggestions during this thesis study. In addition, I would like to thank to thesis jury members Prof. Dr. Uğur EŞME and Assoc. Prof. Dr. Erineç ULUDAMAR for their evaluating my thesis.

I am really grateful to my fellows, Mete Han BOZTEPE, Durmuş Can ACER, İsmail AKTİTİZ, Ahmet ÇETİN, Alparslan TOPCU, Fatih DARICIK, Fırat EKİNCİ, Nazım KURTULMUŞ, Ayşe Nur ACAR, Çağrı UZAY for their motivation and continuous support. Friends like you are not easy to find. I wish also thank to Sefa MERAL, Muhammet YILDIRIMCAN, Murat YILMAZ and Hasan DAŞ for their help in sample preparation and experimental setup. I am also appreciate to Suat US, Ersin ÖLMEZ from Panda Alüminyum and Hasan EŞME from ERVO makina. Your help was invaluable.

Besides I would like to thank the Unit of Scientific Research Projects department (BAP) for the financial support.

I would like to thank from deep down in my heart my family and my wife Merve DELİBAŞ, who have put up with everything for me and are always there for me. So glad I have you. I love you too much...

CONTENS	PAGE
ABSTRACT.....	I
ÖZ	II
EXTENDED ABSTRACT	III
GENİŞLETİLMİŞ ÖZET	VII
ACKNOWLEDGMENT.....	XI
CONTENS	XII
LIST OF TABLES	XVI
LIST OF FIGURES	XVIII
1. INTRODUCTION	1
1.1. Importance of AM.....	2
1.2. Additive Manufacturing working principle.....	4
1.3. AM Processes.....	5
2. PREVIOUS STUDIES.....	13
2.1. The state of the Art in Metal Additive Manufacturing	13
2.2. Fused deposition modeling (FDM) hardware and crucial process parameters.....	15
2.2.1. Effect of process parameters on dimensional accuracy, surface roughness, and resolution of the printed part in FDM type 3D printers.....	18
2.2.2. Effect of process parameters on mechanical properties of the printed part in FDM type 3D printers	23
2.3. Materials and Required filament properties in FDM type 3D printers	26
2.3.1. Commercial polymer materials printed in FDM type 3D printers.....	29
2.3.2. Composite materials developed for use in the FDM type 3D printers.....	31
2.3.2.1. Fused deposition of metals (FDMet) with composite filaments.....	33

2.4. Direct printing of fusible alloys in FDM type 3D printers	36
2.5. Evaluation of the metal printing in FDM systems	39
2.6. Significance and Goal of The Study	42
3. MATERIALS AND METHODS	47
3.1. Characteristics of the fusible alloy	48
3.2. Customization of FDM extruder	50
3.3. Printing experiments for male mold production and casting process for the production of the female mold	54
3.3.1. Experimental equipment used for the printing trials	54
3.3.2. Experimental procedure for the printing experiments	55
3.3.3 The manufacturing of the female mold by casting process	57
3.4. Sheet metal forming process	59
3.5. Evaluation of the dimensional change on printed and cast male molds according to the number of sheet metal forming	60
4. RESULTS AND DISCUSSIONS	63
4.1. Differential scanning calorimetry (DSC) analysis of the Bi58Sn42 alloy ..	63
4.2. 3D printing experiments performed to manufacture sheet metal forming mold	65
4.2.1. 3D Printing trials performed using the standard (unmodified) extruder	65
4.2.1.1. Multi-layered shell printing trials performed using the standard (unmodified) extruder	82
4.2.1.2. Infill printing trials performed using the standard (unmodified) extruder	87
4.2.2. Printing trials performed using the customized extruder	90
4.2.2.1. Infill printing trials performed using the customized extruder	95
4.3. The effect of print settings on 3D printed sample geometry	109
4.4. The performance evaluation of the 3D printed mold in low volume sheet metal part production	110

5. CONCLUSION.....	115
REFERENCES	121
CURRICULUM VITAE.....	137





LIST OF TABLES	PAGE
Table 1.1. Additive manufacturing technologies.....	6
Table 2.1. Characteristic feature and application area of the thermoplastic materials printed in FDM machine	29
Table 2.2. Components of the binder with their effects in filament making and thermal degradation temperatures of components	34
Table 2.3. Available commercial printable metal materials	36
Table 2.4. Samples printed with FDM.....	41
Table 2.5. Samples printed with continuous jetting.....	42
Table 2.6. Samples printed with DOD.....	42
Table 3.1. Technical specification of photopolymer resin.....	50
Table 3.2. Mechanical properties of AA 8006.....	50
Table 3.3. Classification of the customizations made on FDM type 3D printers .	51
Table 3.4. Technical specification of the EMKO ECO PID controller	53
Table 3.5. Technical features of the 3DISON PRO 3D printing machine	55
Table 3.6. Optimized print settings and their limits	56
Table 3.7. Technical features of the Anycubic Photon S (Website, 2021f).....	58
Table 3.8. Technical features of the WANHAO UV LED CURING BOX	58
Table 3.9. Technical specifications of the Instron 8801 axial fatigue test device	59
Table 3.10. Technical specifications of the Romer absolute arm coordinate measurement machine compact RA-7312	61
Table 4.1. Print settings and their effects on the printed sample geometry	109
Table 5.1. Issues experienced during the performed printing trials.....	117



LIST OF FIGURES

PAGE

Figure 1.1. Classification of shaping processes	1
Figure 1.2. Performance evaluation of the traditionally and additively manufactured cylinder head.....	3
Figure 1.3. Generalized AM process flow chart	4
Figure 1.4. Vat photopolymerization process	7
Figure 1.5. Fused deposition modelling process.....	8
Figure 1.6. Nano particle jetting process	9
Figure 1.7. Binder jetting process	10
Figure 1.8. Powder bed fusion process	11
Figure 1.9. Direct energy deposition process.....	11
Figure 1.10. Sheet lamination process representation.....	12
Figure 2.1. Concepts of the extrusion systems based on a) filament, b) mixture, and c) pellet materials	16
Figure 2.2. a) 3D cad data of the object to be printed, b) conversion of CAD data to multiple data (slicing), c) structure of the nth layer, and d) line, triangular and cross raster patterns respectively	18
Figure 2.3. Dimensional difference cause of; a) STL file conversion of the CAD data, b) staircase effect of the layered manufacturing	19
Figure 2.4. The ratio between feeding speed and print head velocity a) 2, b) 1 and c) 0.5	20
Figure 2.5. Dimensional fluctuation in the printed bead causes acceleration- deceleration in the print head a) start, b) acceleration of the print head, c) steady print head velocity, d) deceleration of the print head and e) stop.	21
Figure 2.6. Effect of distance between the nozzle and the build platform on the printed road a) bad levelling, b) good levelling.....	23

Figure 2.7. a) Printed sample geometry (Le Duigou et al., 2016) and bond formation between adjacent roads (b1) surface contact (b2) neck growth, (b3) diffusion at the interface, and randomization	24
Figure 2.8. (a) Void formation at the intersection of infill and outline perimeter (contour), (b) minimization of the void with negative offset, and (c) minimization o the void with the altered tool path	25
Figure 2.9. Build orientations of the part on platform	26
Figure 2.10. Melt extrusion failure types in FDM machine.....	28
Figure 2.11. Ideal conditions for the printing of material in the FFF method	28
Figure 2.12. Materials used in FDM technology	32
Figure 2.13. Steps of the extrusion based additive manufacturing; a) printed part (green part), b) debinding in a solvent, c) sintering and d) optional finishing processes.....	33
Figure 2.14. Machine Cost of the AM technologies	43
Figure 3.1. The Bismuth – Tin phase diagram.....	48
Figure 3.2. The viscosity of the Bi58Sn42 alloy depending on the temperature and rotational speed of the rheometer.....	49
Figure 3.3. Image of the customized extruder.....	53
Figure 3.4. Image of the EMKO ECO PID controller	53
Figure 3.5. 3DISON PRO desktop type FDM printer.....	55
Figure 3.6. Applied casting process for the female mold production	58
Figure 3.7. Instron 8801 axial fatigue test device	59
Figure 3.8. Press forming operation for low volume sheet metal parts production.....	60
Figure 3.9. Romer absolute arm compact coordinate measurement machine.....	61
Figure 4.1. DSC tracks for the Bi58Sn42 alloy heated to 350 °C in the open atmosphere and the Bi58Sn42 alloys with a diameter of 1.67 and 2 mm supplied from two different manufacturers	64

Figure 4.2. The layout of the lines printed on the built platform with different process parameters.....	66
Figure 4.3. Lines printed in the ET of 140 °C using 1.02 mm diameter brass nozzle.....	67
Figure 4.4. Lines printed in the ET of 145 °C using 1.02 mm diameter brass nozzle.....	67
Figure 4.5. Lines printed in the ET of 143 °C using 1.02 mm diameter brass nozzle.....	68
Figure 4.6. The shoe geometry printed at 143 °C of ET, PS of 200 mm/min, EM of 1.4, LT of 0.2 mm using 1.02 mm diameter brass nozzle	69
Figure 4.7. a) Simplify3D image of the square object to be printed, b) Square sample printed in ET of 143 °C, PS of 200 mm/min, EM of 1, LT of 0.2 mm using 1.02 mm diameter brass nozzle	70
Figure 4.8. a) The square sample printed in ET of 143 °C, PS of 200 mm/min, EM of 1.15, LT of 0.2 mm using a 1.02 mm diameter brass nozzle, b) Square sample printed in EM of 1.15 and printing gap of 0.15 mm.....	71
Figure 4.9. a) Standard (unmodified) extruder assembly with Stainless Steel screw barrel with heater cartridge and Brass nozzle, b) Mono-block Aluminum nozzle instead of using screw barrel and nozzle assembly	72
Figure 4.10. Printed circle pattern using the new nozzle made from AL 7075, PSs varied from 300 mm/min to 1300 mm/min	73
Figure 4.11. Thermal image of brass and aluminum nozzles from left to right, respectively	73
Figure 4.12. a) Thermal paste between the heater block and Aluminum nozzle b) Thermal image of brass and aluminum nozzle from left to right respectively after the thermal paste application of the assembly interfaces.....	74

Figure 4.13. Deformed Bi58Sn42 filament due to the pushing and retraction movements during the printing process	75
Figure 4.14. The layout of the desired maze structures on the build platform according to the different printing speeds and start point locations ...	78
Figure 4.15. Printed maze structures based on 150, 300, 450, 600, 750, and 900 mm/min printing speeds	79
Figure 4.16. Close-up of a printed wireframe with a printing speed of 150 mm/min at 185 °C.....	80
Figure 4.17. The desired layout of the maze structures on the build platform according to the exact and different start point locations	80
Figure 4.18. Printed maze structures based on the identical and different start point locations at ET of 185 °C	81
Figure 4.19. Printed maze structures based on the exact starting point locations at ET of 185 °C	82
Figure 4.20. Ring samples printed in vase mode	83
Figure 4.21. The hollow cylinder printed in vase mode	83
Figure 4.22. Separation of the printed part's first layer from the middle section of the copper-clad board due to the improper leveling during printing of a open shell box with 78 layers at ET of 180 °C ; a) front view and b) back view	84
Figure 4.23. Layer separation on the printed structure; a) front view and b) side view.....	85
Figure 4.24. The printed male shell consists of 125 layers; a) front view and b) back view.....	85
Figure 4.25. The printed female shell consists of 125 layers; a) front view and b) back view.....	86
Figure 4.26. Images of the printed curvilinear shell specimens; a) Failed print at the initial stage of the process, b) Failed print at 47% of the print process, and c) Failed print at 70% of the print process	87

Figure 4.27. Infill samples printed using EM of 1, PS of 100 mm/min, LT of 0.2, PT of 75°C, ET of 160 °C.....	89
Figure 4.28. A maze shape to be printed to evaluate the continuity in the printed sample.....	91
Figure 4.29. Printed maze geometry at an extrusion temperature of 140 °C	91
Figure 4.30. Printed maze geometry at an extrusion temperature of 150 °C	92
Figure 4.31. The layout of the maze shape to be printed	93
Figure 4.32. Printed specimen for EM:2, PS: 100 mm/min, Temp:160 °C, LT: 0,2 and table temp: 75 °C	93
Figure 4.33. Image of the sample printed at printing speed: 100 mm/min, extrusion multiplier: 4, layer thickness: 0,2 mm, table temp: 75 °C and extrusion temperature 170 °C a) top view and b) side view	94
Figure 4.34. Sample printed at printing speed: 100 mm/min, extrusion multiplier: 1, layer thickness: 0,2 mm, table temp: 75 °C and extrusion temperature 200 °C	95
Figure 4.35. Sample printed at printing speed: 100 mm/min, extrusion multiplier: 4, layer thickness: 0,2 mm, platform temp: 75 °C and extrusion temperature 200 °C; a) top view and b) side view	96
Figure 4.36. Square sample printed at printing speed of 100 mm/min, extrusion multiplier of 4, the layer thickness of 0,2 mm, platform temp of 75 °C, extrusion temperature 200 °C, and %50 infill	97
Figure 4.37. a) The process simulation image of the part to be printed and b) Square sample printed at printing speed of 100 mm/min, extrusion multiplier of 1, the layer thickness of 0,2 mm, platform temp of 75 °C, extrusion temperature 200 °C, and %75 infill.....	97
Figure 4.38. a) Simplify3D image of the object and b) the obtained result for the solid square sample using extrusion temperature 200 °C and table temperature 75 °C with a printing speed of 100 mm/min, extrusion multiplier 1 and % 100 infill rate, respectively.....	98

Figure 4.39. Obtained results for the solid square sample using extrusion temperature of 200 °C and table temperature of 75 °C with a printing speed of 100 mm/min, extrusion multiplier 1, and % 100 infill rate, respectively	99
Figure 4.40. a) The process simulation image of the part to be printed and b) The solid square sample was 3D printed using an extrusion temperature of 200 °C, table temperature of 75 °C, printing speed of 100 mm/min, extrusion multiplier of 1, extrusion width of 0.5 mm, and % 100 infill rate	100
Figure 4.41. a) The process simulation image of the part to be printed and b) The solid square sample was 3D printed at an extrusion temperature of 200 °C, platform temperature of 75 °C, printing speed of 100 mm/min, extrusion multiplier of 1, extrusion width of 0.3 mm, and 100 % infill rate	101
Figure 4.42. The solid square sample was 3D printed at an extrusion temperature of 180 °C, platform temperature of 75 °C, the printing speed of 100 mm/min, extrusion multiplier of 1, extrusion width of 0.3 mm, and 100% infill	102
Figure 4.43. Image of the infill patterns: a) concentric infill, b) rectilinear infill .	104
Figure 4.44. Images of the 3D printed single-layer solid circle with a) concentric and b) rectilinear infill patterns, respectively	105
Figure 4.45. Simplify3d images of the hemisphere for a) vase mode and b) start-stop mode	106
Figure 4.46. Hemisphere sample with a diameter of 20 mm printed in vase mode using PS of 100 mm/min, LT of 0.2 mm, PT of 75°C, ET of 170 °C, and EM of 1; a) top view and b) side view	107
Figure 4.47. Solid hemisphere sample with a diameter of 10 mm printed in start-stop mode using PS of 100 mm/min, LT of 0.2 mm, PT	

of 75°C, ET of 170 °C, IR of 100 %, and EM of 1; a) isometric view and b) top view	107
Figure 4.48. Solid hemisphere sample with a diameter of 10 mm printed in start-stop mode using PS of 500 mm/min, LT of 0.2 mm, PT of 75°C, ET of 170 °C, IR of 50%, and EM of 1; a) isometric view and b) side view	108
Figure 4.49. Solid hemisphere sample with a diameter of 20 mm printed in start-stop mode using PS of 500 mm/min, LT of 0.2 mm, PT of 75°C, ET of 170 °C, IR of 50%, and EM of 1; a) isometric view and b) side view	109
Figure 4.50. Deviation in the stamped 0.2 mm thickness Aluminum 8006 sheets' diameter.....	111
Figure 4.51. Deviation in the stamped 0.3 mm thickness Aluminum 8006 sheets' diameter.....	112
Figure 4.52. Sheet metal formed components.....	113



1. INTRODUCTION

Engineering design process is a challenging process that begins with the definition of the problems and ends up with the manufacturing of the product. The available subtractive, formative and additive manufacturing processes were illustrated in Fig. 1.1.

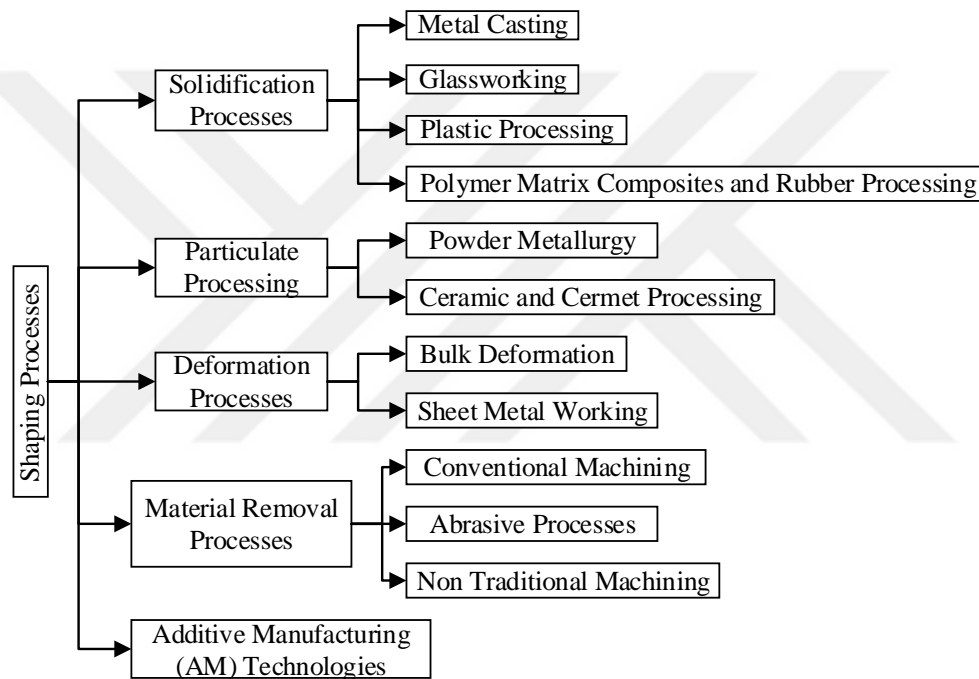


Figure 1.1. Classification of shaping processes (Groover, 2012)

Knowing that the design process is an iterative process, some steps can be repeated until the desired performance is achieved. For this reason, both release date of the product into the market is delayed and the cost of the product increases. Furthermore, the designed product may even become outdated until a company releases it.

Hence when the companies develop new products, they must present their products to the market in a short time. To survive in this competitive global

environment, it has become compulsory for some companies to move from mass production to flexible manufacturing systems such as additive manufacturing (AM).

AM is defined as fusion of materials to build parts depending on the CAD data in contradistinction to subtractive and formative manufacturing methodologies due to ISO/ASTM 52900:2015.

1.1. Importance of AM

Main application areas of AM technology can be briefly separated into rapid prototyping (RP) and rapid manufacturing (RM). In RP area AM facilitates understanding and evaluation of the prototype. Thus, essential modifications can be made on the concept design (prototype) according to judgements from different departments in the facility before the release date of the product. In RM area AM can be used to produce end user product, finish parts that require assembly or for producing mold (Rapid Tooling). Also printed objects can be used as master models. Secondary processes like vacuum casting, silicon rubber molding etc. is applied to master model to produce mold or prototype part. These methods are called as indirect tooling and indirect prototyping processes respectively (Gebhardt, 2011).

Besides AM's contribution to mold and prototype production, it can be used to repair damaged or worn region of the any component with minimal heat effect (Website, 2019a).

Manufacturing of the complex geometries is limited in conventional manufacturing methods. Therefore, performance of some developed solutions to new generation problems are lower than AM technology. For instance, cylinder head both designed by conventional and AM were given in Fig. 1.2. Additively manufactured cylinder head both is lighter and can work in higher speed with improved cooling surface area. So, AM makes companies more competitive in the market.

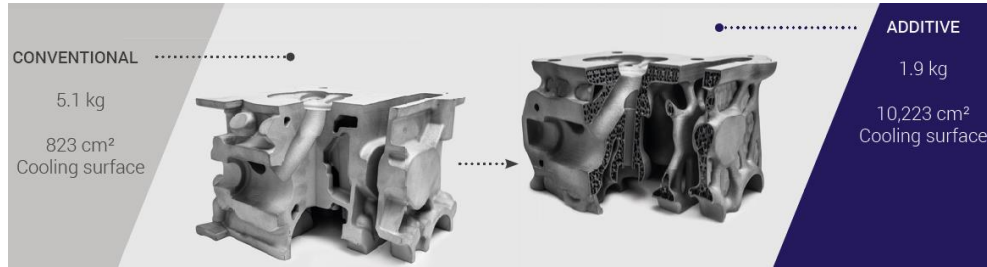


Figure 1.2. Performance evaluation of the traditionally and additively manufactured cylinder head (Website, 2015)

The more complexity means the higher cost and lead time to market in conventional manufacturing methods in contrast to AM technology (Bryden et al., 2000).

Since the part can be built just in time in AM, both stocking and transportation (logistic) costs decrease. This is especially useful for the critical operations such as military etc. There is no need to wait for spare parts which cause delay in operation for days (Website, 2019b; Website, 2019c).

Moreover, investment in tooling equipment (jigs and fixtures etc.) decreases so that no longer need to large inventory (Attaran, 2017).

Despite the advantages of AM described above, it has following drawbacks:

- Diversity of printable materials are restricted when it is compared with conventional systems.
- Production time is high cause of the layered manufacturing.
- Poor dimensional accuracy and surface roughness according to conventional processes.
- Low level of accuracy in repeatability (Baumers et al., 2016).

But both academia and companies continue to work to overcome these problems.

1.2. Additive Manufacturing working principle

To build or print a part (3D object), most AM processes involve the following 5 steps as shown in Fig. 1.3.

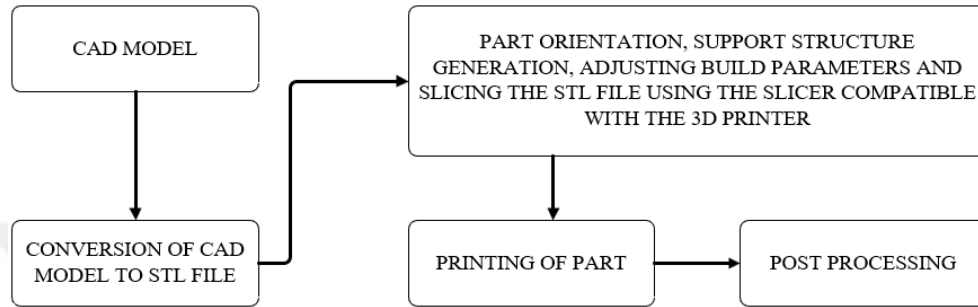


Figure 1.3. Generalized AM process flow chart (Gibson et al., 2021)

1. CAD model: The CAD file that describes the geometry of the part to be printed or build is required.

2. Conversion of CAD data to STL format: Using most computer-aided design program, CAD file is transformed to STL file format that involves data about the surface geometry of a three-dimensional model by the unit normal and vertices of the triangles according to the three-dimensional Cartesian coordinate system without any CAD model features such as color, texture etc. (Iancu et al., 2010).

3. Preprocessing: This step can be divided into four subsections;

- **Part orientation** is the rotation of the part due to axes of the machine's coordinate system in the build volume (Leutenecker et al., 2016) and the orientation is adjusted in the build volume via software of the AM machine. Orientation of the part before printing is crucial since proper orientation improves dimensional accuracy, reduces the build time and the support structure needed for building the model. Thus, cost of the printing process will decrease (Jibin, 2005).
- **Support structures** are fine scaffold structures which are used for heat dissipation and fixation of the part in the build volume, especially for

supporting horizontally oriented and overhanging surfaces (Herzog et al., 2016). After determining orientation of the part to be printed, if it is required, support structure from the build material (for single nozzle extrusion AM systems etc.) or soluble material (for multi-nozzle extrusion AM systems etc.) must be employed to form complex geometries such as undercuts, and printed part assemblies with moving components etc (Gao et al., 2015). Proper support structure placement is critical since it affects the build time, material consumption and quality of the printed part (Leary et al., 2014).

- **Build parameters** or printing parameters are adjusted by the user in the software of the AM machine so that the machine operates according to these set values. Setting these parameters is very important since it affects the quality of the build object.
- **Slicing process:** In this step, parallel planes are formed based on the orientation of the digital model then each two parallel planes are intersected with STL file of the model. Intersection of each plane with triangles of STL file gives set of lines / points which are used to create contour of the one slice or layer (Bandyopadhyay et al., 2015).

4. Printing of part is commenced due to the adjusted settings by the operator.

5. Post processing: Due to used AM technique and material, proper post processing methods such as surface or heat treatment processes etc. can be applied to the printed part to improve its surface roughness, dimensional accuracy and mechanical properties (Kumbhar and Mulay, 2018; Bagherifard et al., 2018).

1.3. AM Processes

American Society for Testing and Materials (ASTM) group classified the current and future AM methods in 7 categories (Website, 2020a). The categories and technologies covered are given in Table 1.1.

Table 1.1. Additive manufacturing technologies (Website, 2020b)

Main Catagory	AM processes	Built Material
Vat Photopolymerization	Stereolithography (SLA)	Plastic
	Digital Light Processing (DLP)	
	Continuous Digital Light Processing (CDLP) or (DLS)	
Material Extrusion	Fused Deposition Modelling (FDM) or (FFF)	Composite, Plastic
Material Jetting	Material Jetting (MJ)	Plastic
	Nano Particle Jetting (NPJ)	Metal, Ceramic
	Drop On Demand (DOD)	Wax
Binder Jetting	Binder Jetting (BJ)	Gypsum, Sand, Metal
Powder Bed Fusion	Multi Jet Fusion (MJF)	Plastic
	Selective Laser Sintering (SLS)	
	Direct Metal Laser Sintering (DMLS) / Selective Laser Melting (SLM)	Metal
	Electron Beam Melting (EBM)	
Direct Energy Deposition	Laser Engineering Net Shape (LENS)	Metal
	Electron Beam Additive Manufacturing (EBAM)	
Sheet Lamination	Laminated Object Manufacturing (LOM)	Composite, Paper

➤ **Vat Photopolymerization:**

The UV laser beam is reflected to the liquid photopolymer material in the tank (vat) according to CAD data. Hence photopolymer material is cured by laser beam. After one layer is obtained, build platform moves downward by adjusted layer

thickness. Then process continues until the desired geometry is obtained. Schematic representation of the process was given in Fig. 1.4.

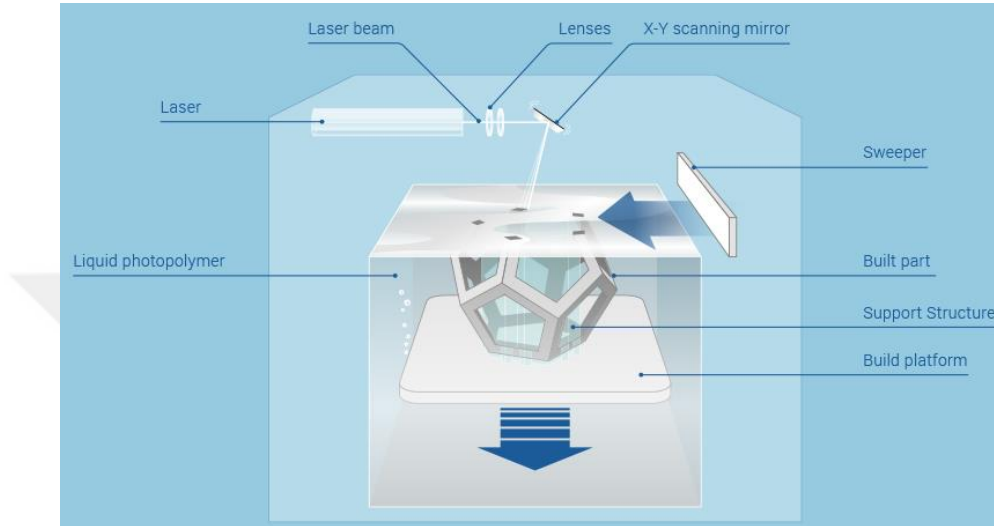


Figure 1.4. Vat photopolymerization process (Website, 2020c)

➤ **Material Extrusion:**

In extrusion-based systems, polymer-based filament is heated above its glass transition temperature or melting point then it flows to the appropriate place on the build platform via controlled motion of the both drive wheels and extruder head depending on the CAD data. After one layer is deposited, build platform moves downward with set layer thickness. The process continues till the part is built completely. Typical material extrusion-based process was given in Fig. 1.5.

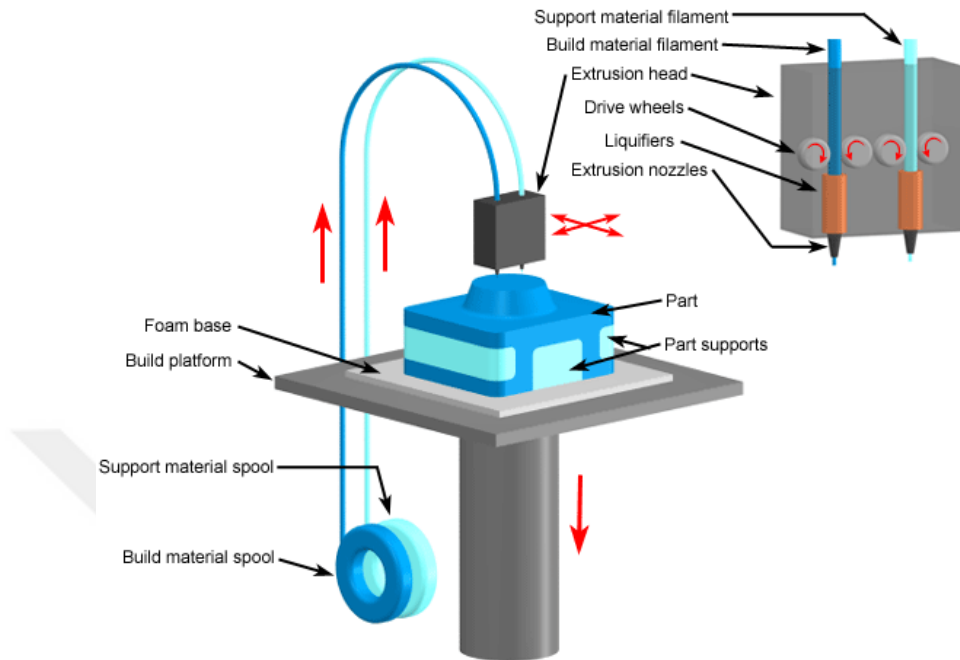


Figure 1.5. Fused deposition modelling process (Website, 2020d)

➤ Material Jetting

Material jetting is similar to inkjet printers. Droplets of suspension that includes either support or build nano particles, are jetted to the build platform selectively due to CAD data via continuous or drop on demand (DOD) method from thousands of nozzles. Solidification is achieved by ultra violet light for resin or temperature control for metal and ceramic materials. Temperature controlled environment (for metal or ceramic) evaporates the binder in suspension to form one layer. After one layer is deposited, the process is repeated until the whole part is printed. Post processing is required to strengthen the part and remove support structure. Material jetting method is shown in Fig. 1.6.

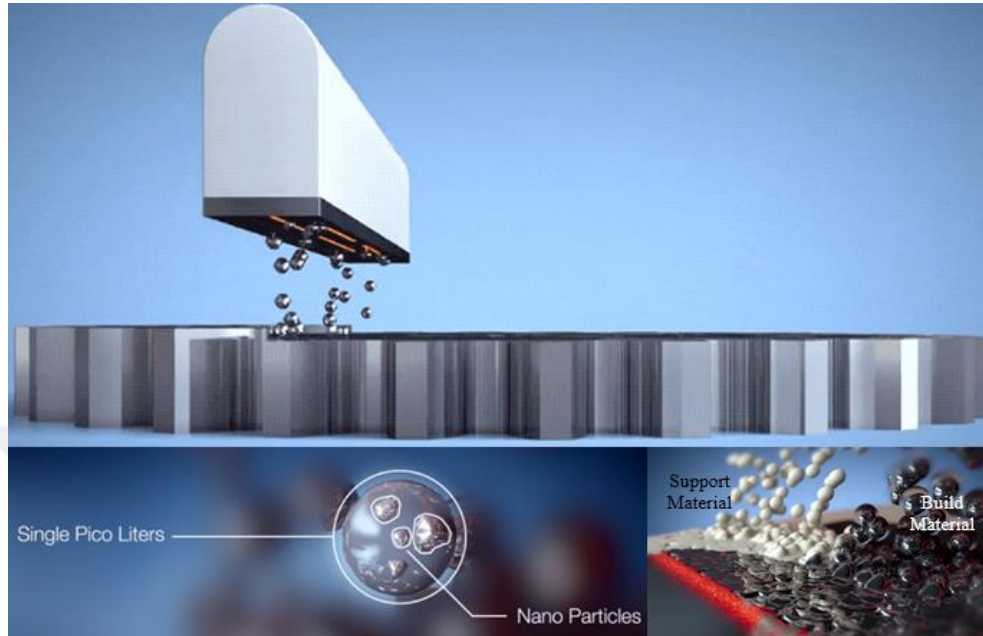


Figure 1.6. Nano particle jetting process (Website, 2020e)

➤ **Binder Jetting**

The main material is in powder form at this type of systems. Process commences with spreading of the powder material by a roller as seen on Fig. 1.7. Binder that has special formula selectively deposited onto powder layer according to CAD data. Then the build platform lowers one-layer thickness and process continues until the whole geometry is achieved. Post processing is required to strengthen the printed object.

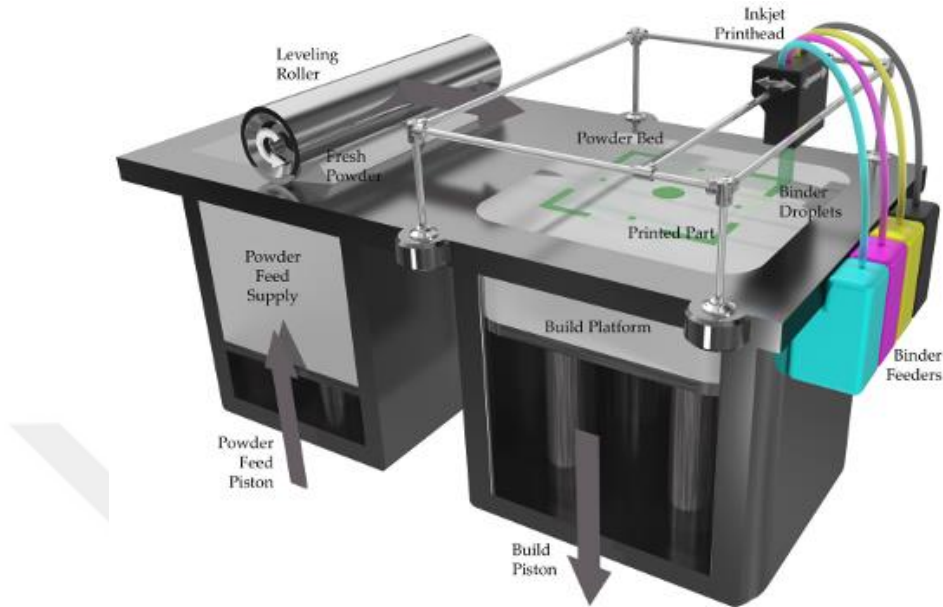


Figure 1.7. Binder jetting process (Website, 2020f)

➤ **Powder Bed Fusion**

Powder bed fusion processes requires the spreading of the powder material like in binder jetting. Laser or electron beam is used for the selectively formation of bond between powder particles. Mechanical properties of the build part are close to traditionally manufactured part. Post processing is performed to remove support structures, release residual stresses, improve metallurgical structure, and surface roughness. The powder bed fusion system is shown in Fig. 1.8.

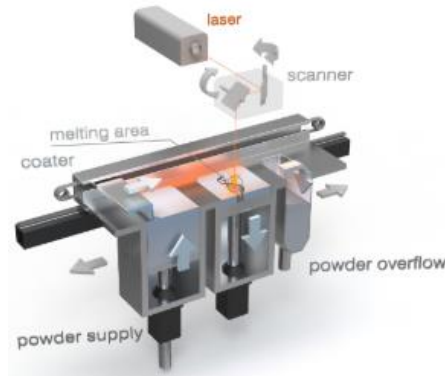


Figure 1.8. Powder bed fusion process (Website, 2020g)

➤ **Direct Energy Deposition**

Working principle of the system is similar to FDM. But nozzle can move in multiple direction since it is mounted onto 4, 5 axis machines. Used material form can be wire or powder in these systems. When the material is deposited from a nozzle to existing surface of the object, in the same time plasma arc, electron beam or a laser is applied to melt the material. Also, the system can be used for repairing or creating new feature on the existing object. Some companies adapted these systems to their CNC machines and called as hybrid systems (Website, 2020h). Direct energy deposition process is shown in Fig. 1.9.

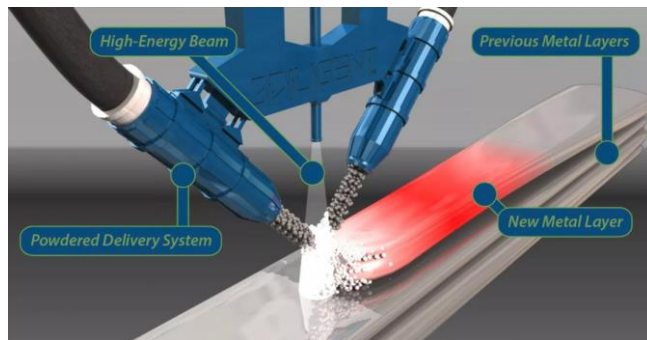


Figure 1.9. Direct energy deposition process (Website, 2020i)

➤ **Sheet Lamination**

Form of the raw material is sheet form in LOM. Feeding of the sheets onto build platform is supplied by rolls as it is seen from Fig. 1.10. Laser or knife is used to cut the sheet in desired shape. Bond formation between the layers occurs when heated roller applies pressure to adhesive coated sheet material and activate heat sensitive adhesive.

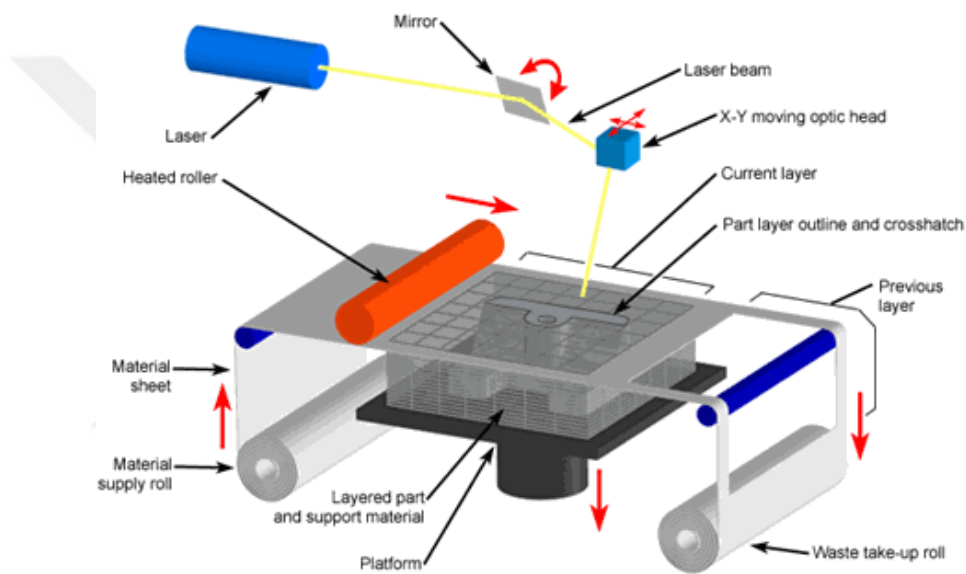


Figure 1.10. Sheet lamination process representation (Website, 2020j)

2. PREVIOUS STUDIES

In this section, alternative metal additive manufacturing methods were reported. Furthermore, detailed information about the FDM process was presented.

Initially, the extruder head structure of the FDM hardware was examined. Then important process parameters and their effects on the quality of the printed part were specified. This is followed by the material properties required for the successful deposition in the FDM type printer. Lastly, customizations made to print metal structures in FDM type 3D printers were researched and evaluated.

2.1. The state of the Art in Metal Additive Manufacturing

The main categories of the Additive Manufacturing (AM) systems and their members were presented briefly in section 1.3. However, all-metal printing processes were not introduced in the ASTM standard. Therefore, the remaining metal printing processes were mentioned under this topic.

Among the existing AM methods, the most widely employed metal printing process is beam-laser based systems. On the other hand, it has been observed that the use of alternative metal AM methods has increased over the years. In order of use, these methods are Material Extrusion (ME), Binder Jetting (BJ), Material Jetting (MJ), Electrochemical AM (EAM), Cold Spray AM (CSAM), Ultrasonic AM (UAM), Additive Friction Stir Deposition (AFSD), Wire AM (WAM) (Vaezi et al., 2020).

While the UAM and WAM are categorized under sheet lamination and directed energy deposition category respectively, EAM, CSAM, and AFSD are not classified under any category.

In the UAM process, the thin metal foil is pressed onto another one under constant force. Then ultrasonic motion is applied to break the oxide layer on each surface of the foils and to form solid-state bond between the metal foils. It doesn't require any special environment in contrast to beam-laser based systems. In addition,

the bonding temperature is significantly lower than the melting temperature of the material. Hence, there won't be changes in phase and grain size. Moreover, bonds can be created between dissimilar metals without any undesirable metallurgical properties. Machining can be performed to obtain better dimensional accuracy (Website, 2020k).

WAM technology builds 3D free form part geometry by joining the wire feedstocks using an electric arc. It can be applied to all weldable metals and alloys. During the joining of wire feedstocks, inert gas has to be used locally to prevent oxide formation. Therefore, an enclosed chamber is not essential and large-scale metal part production is possible. In addition to the creation of the 3d model, it can be also utilized for repair. Diverse gas mixtures and controlled cooling can be exerted for enhancement of the properties of the finished part (Website, 2012).

The origin of the CSAM process depends on the solid-state coating process. Powder particles that have high kinetic energy sprayed to the substrate from the specially designed supersonic nozzle in an open atmosphere. A supersonic gas jet is used to accelerate the powder particles whose diameters in the range of (1-50) μm diameters. The velocity of the particles varies between 300 and 1200 m/s due to the applied pressure. The deterioration of the oxide layer on the particle surface due to impact and the effect of high contact pressure cause bond formation between the particles. As the kinetic energy of the particles is lower than the required melting energy for the particle, melting doesn't occur (Singh et al., 2013). Therefore, problems such as residual thermal stresses, phase transformation, and re-crystallization are not encountered. Despite these advantages, it is quite challenging to build fully dense parts from the super alloys, Ti alloys, and stainless steel. Post-processing such as heat treatments and machining is required to improve ductility and obtain desired tolerance values respectively. Furthermore, the cost of driving gas is expensive (Vaezi et al., 2020).

AFSD is also a solid-state (low-heat) process. The large-scale fully dense metal part can be manufactured in an open atmosphere. Feedstock material can be in

either powder or solid bar form. A combination of high contact force and dynamic friction forms the bond between layers. Because of the stirring action, the grain size of the deposited material is lower than the raw material. Therefore, the mechanical strength of the raw material increases after the AFSD process. Grains are oriented uniformly on all axis. Isotropic parts are generated. Aluminum, titanium, steel, and nickel-based superalloys can be deposited. The application area of the AFSD involves coating, metal joining, part repair, custom metal alloy, and metal matrix composite billet fabrication. Machining is required to reach the desired surface quality (Website, 2020l).

EFAB (a trademark of Microfabrica) is a microscale EAM technology. Two types of metals are employed in this process. While one of them is sacrificial, the other forms the main structure. Both of them are electrodeposited selectively. Then, a sacrificial partition of the final part is removed by a selective etching process. Feedstock materials are specially developed by Microfabrica (Cohen et al., 2010).

In conclusion, it was observed that different types of metal AM technologies are available and each of them has its pros and cons. For this reason, the appropriate system should be selected by considering specific requirements. In this study, the material extrusion method is selected since it is simple, low cost, and allows customization. Therefore, studies related to FDM are presented in detail in the following sections.

2.2. Fused deposition modeling (FDM) hardware and crucial process parameters

The FDM process was patented by Scott Crump in 1989 (Gibson et al., 2010). As mentioned in section 1.2, after generating CAD data on any CAD software for the object to be printed in the AM system, a slicer (commercially available software) is used to convert the CAD data to multiple layer data that is transferred to drive motors as signals. Each of the formed layer data involves its own specific geometric and individual data that is defined partially by the user in the slicer. The

whole FDM process was shown in Fig. 2.2a – 2.2c. Every single layer is formed via the motion of the dispensing head (extruder) and the build-platform according to generated drive signals in the slicer while the material is being extruded from the nozzle. The material is heated above the solidification temperature by a heater on the extruder. Upon extrusion, onto the build platform or deposited layer, the printed material is solidified considerably. Thermoplastic materials, waxes, and metals may be printed (Crump, 1992). According to the form of the feedstock (material to be printed), alternative extrusion systems such as roller, piston, and screw for feeding of filament, mixture, and pellets respectively are available as seen from figure 2.1.

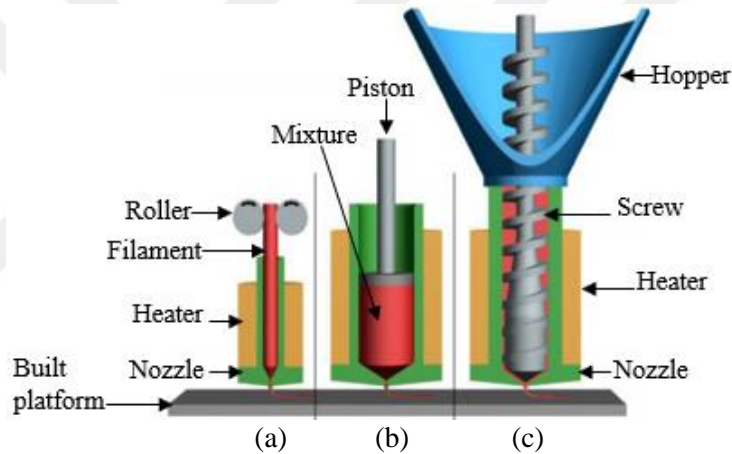


Figure 2.1. Concepts of the extrusion systems based on a) filament, b) mixture, and c) pellet materials (Valkenaers et al., 2013)

When studies between 1994 and 2019 years related to optimization of process parameters to improve dimensional accuracy, surface roughness, and mechanical properties of the object printed in FDM hardware are examined (Vyavahare et al., 2020), the main factors affecting the quality of the printed object were determined and summarized as:

- Layer thickness refers to the height of the single layer, as shown in Fig. 2.2b.
- Extruder temperature is a setting so that the filament is heated up to this value in a controlled manner.
- Road width is the width of the extruded single bead, as shown in Fig. 2.2d.
- Raster (infill) is the template used for filling the internal region of the object. Various types of raster pattern are available as seen from Fig. 2.2d.
- Infill percentage indicates the filled volume of the printed part.
- Raster angle means the angle of the selected raster pattern due to the x-axis of the layer.
- Printing speed is the movement speed of the print head in the gantry while the melt material flowing from the nozzle.
- The extrusion multiplier is the modification factor used for the adjustment of the required amount of filament for the entire print. Slicer automatically calculates the required amount of filament according to the size of the object, road width, layer thickness, infill percentage, raster pattern, etc. However, it may be necessary to modify this factor according to the used filament material.

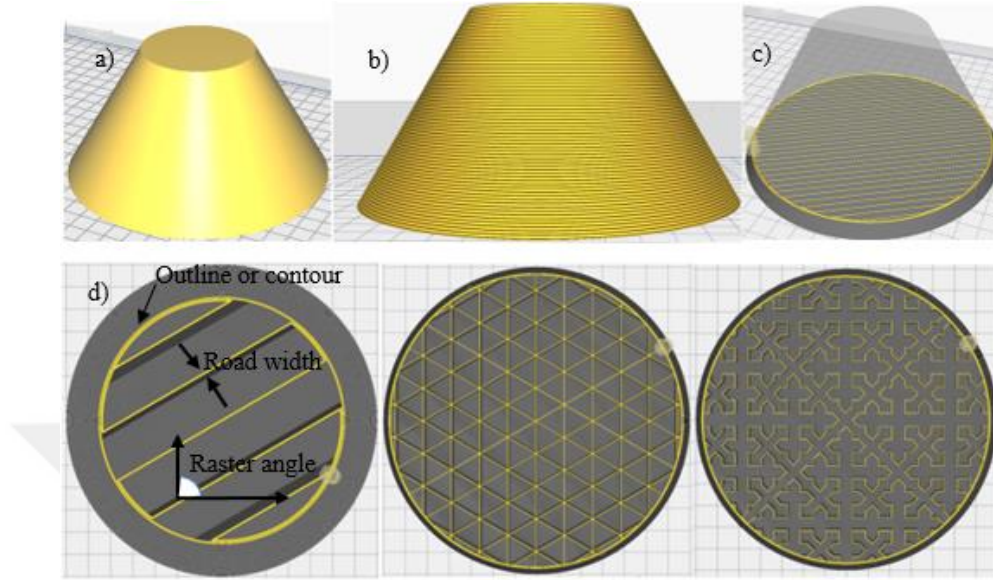


Figure 2.2. a) 3D cad data of the object to be printed, b) conversion of CAD data to multiple data (slicing), c) structure of the nth layer, and d) line, triangular and cross raster patterns respectively

2.2.1. Effect of process parameters on dimensional accuracy, surface roughness, and resolution of the printed part in FDM type 3D printers

The main reasons for the dimensional difference between CAD data and printed objects arise from the conversion of the CAD data to STL file format and approximation of the curved region in build direction during slicing as seen from Figs. 2.3a and 2.3b respectively.

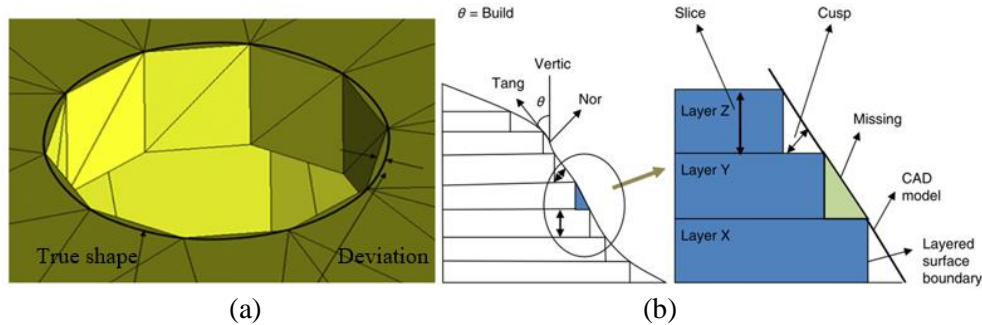


Figure 2.3. Dimensional difference cause of; a) STL file conversion of the CAD data, b) staircase effect of the layered manufacturing (Nasr et al., 2014)

Anitha et al. (2001) reported that decreasing layer thickness improved the surface roughness of the printed object. Yet since using uniform layer thickness through all print increases the build time, an alternative slicing method that is called adaptive slicing that allows printing the object with different layer thicknesses to improve dimensional accuracy and decrease build time was developed (Sabourin et al., 1996). Melgoza et al. (2014) developed the continuous tool path deposition strategy for the printing of shell structures with improved surface quality.

It was also shown that part orientation in the build volume is the most effective factor in the dimensional accuracy of the FDM printed part (Sahu et al., 2013). However, orientation may necessitate the use of support structure depending on the geometric shape of the part and dimensional accuracy can be affected adversely. Therefore, Leary et al. (2014) applied topology optimization for the component to be printed so that part has a self-support structure in itself and there is no need to use support material.

A variation on the flow rate from the nozzle also affects dimensional accuracy, resolution, and surface roughness on the printed part as these variations will affect the layer thickness and road width. The factors cause the deviations are listed below:

- The force that must be applied to the filament in the cold region of the liquefier by the drive motor to drain the melt from the nozzle depends on the pressure drop in the liquefier channel and the entrance area of the channel. Although the pressure-drop changes dynamically, the force applied by the feeding motor is constant due to the absence of pressure drop feedback in the system (Ramanath et al., 2008).
- Movement speeds of the feeding roller and print head must be accommodated otherwise printed road is affected adversely as seen from Fig. 2.4. But the slicing engine allows only the adjustment of the print head velocity by the user while there is no direct control for the feeding roller speed.

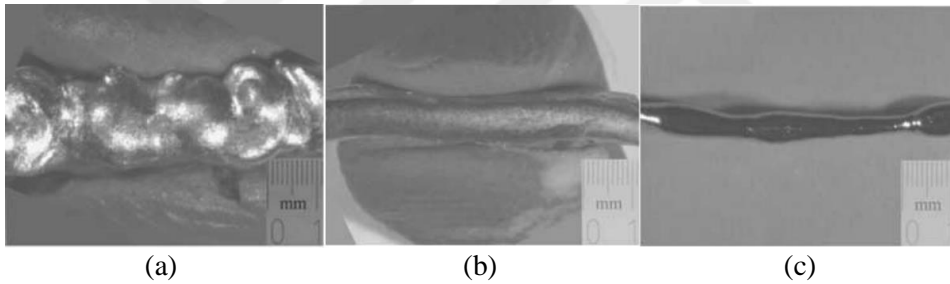


Figure 2.4. The ratio between feeding speed and print head velocity a) 2, b) 1 and c) 0.5 (Finke and Feenstra, 2002)

- To maintain printing speed at a current level defined by the user on the slicing engine, acceleration-deceleration occurs on the print head at the start and end of the printing process or during sharp turns depending on the geometry of the object to be printed. Feed rollers commence the feeding filament to the nozzle slightly before the motion of the print head. Similarly, rollers stop feeding the filament to the nozzle before the print head reaches the end of the segment. Optimization must be done carefully for both situations to obtain uniform roads or beads. Nevertheless, even if optimization is performed, uniform line structure

(road width and layer thickness) may not be obtained due to the flow characteristics of the material as seen from Fig. 2.5 (Agarwala et al., 1996).

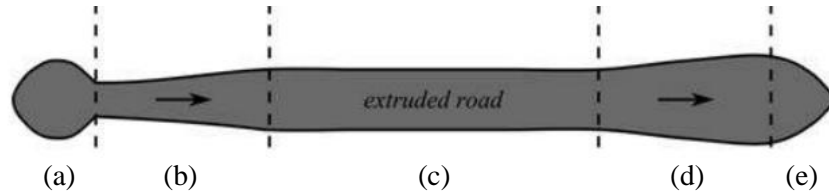


Figure 2.5. Dimensional fluctuation in the printed bead causes acceleration-deceleration in the print head a) start, b) acceleration of the print head, c) steady print head velocity, d) deceleration of the print head and e) stop (Turner and Gold, 2015).

- The teeth of the roller must grip the filament perfectly so that the filament cannot slip between the rollers during feeding. As deviation in filament diameter affects the flow rate, tight tolerance is required on the filament (Agarwala et al., 1996).

During the printing process, the thermal gradient occurs for the following reasons:

- Coalescence of layers or roads (solidified segment and segment being printed) at different temperatures. Moreover, as the number of layers increases, the thermal gradient increases (Sood et al., 2010).
- Depending on both geometry of the printed part and the different convective cooling rates in the built environment, the variation of cooling rates within the printed part also generates the thermal gradient.

The thermal gradient induces internal stresses within the printed part cause of non-uniform expansion and solidification shrinkage. Depending on the magnitude of the stress that occurs, the product may be warped, delaminated, or cracked.

Industrial level systems have the ambient temperature-controlled environment and fans to minimize the thermal gradient within the build object especially for the polymers that have a high melting point like unfilled polyetherimide (ULTEM). On the other hand, the open-source systems have a temperature-controlled build platform to minimize the thermal gradient. Hence this restricts both the size of the object to be printed and extrusion temperature that can be set (Turner et al., 2014). The characteristic features of the filament material (glass transition temperature & shrinkage rate) also affect the warping deformation of the printed part. Therefore, the filament that has a low glass transition temperature and shrinkage rate (0.3 % - 0.5%) is better for the FDM process. A short raster pattern length must be employed in the internal region of the object to minimize the warp deformation (Wang et al., 2007).

The accuracy of the system components (timing belt, pulley, ball screw, and step motor, etc.) further influences the quality of the printed part (Cunico et al., 2013).

The distance between the nozzle and the build platform should be adjusted so well that both the surface of the printed road is flat and the flow is more stable as seen from Figs 2.6a and 2.6b. Besides, both the printing speed and feeding speed should be adjusted according to the distance set between the nozzle and the table. Otherwise, the print may fail (Peng et al., 2014). Advanced systems can create surface topography of the build platform by laser scanning. Hence, the distance between the build platform and the nozzle is adjusted automatically at each point of the platform (Website, 2020m). Wearing of the nozzle is another problem encountered during the printing of different filament materials from thermoplastic filaments (Gnanasekaran et al., 2017). Hence, it may be necessary to install a new nozzle.

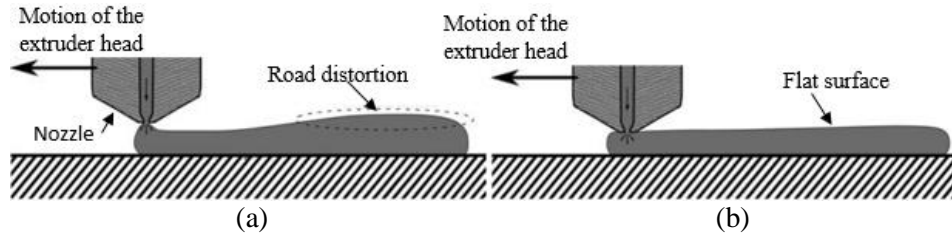


Figure 2.6. Effect of distance between the nozzle and the build platform on the printed road a) bad levelling, b) good levelling (Turner et al., 2014)

The resolution of the printed part can be improved by decreasing the nozzle diameter. But the probability of clogging increases as the smaller nozzle diameter increases pressure drop (Tlegenov et al., 2017).

Fundamental factors affect the dimensional accuracy, resolution, and surface roughness were mentioned. It was observed that the parameters were contradictory to each other. For example, while reducing the layer thickness decreases the staircase effect, simultaneously it increases both warping deformations due to increased thermal gradient and builds time. Therefore, the optimizing process parameters are complex. Though to obtain a better surface finish, post-processing can be performed such as sanding, acetone dipping, milling, electroplating, painting, etc. (Chohan and Singh, 2017).

2.2.2. Effect of process parameters on mechanical properties of the printed part in FDM type 3D printers

When the structure manufactured on the FDM machine is investigated at the macroscopic level, it can be seen that it consists of voids and partially bonded filaments as seen from Fig. 2.7a. Therefore, the mechanical properties of the printed components depend on filament material features (viscosity, surface tension), voids, and bond strength between adjacent filaments (Garzon-Hernandez et al., 2020).

Bond formation between two adjacent extruded filaments (road) occurs in three levels as shown from Figs. 2.7.b1 – 2.7.b3.

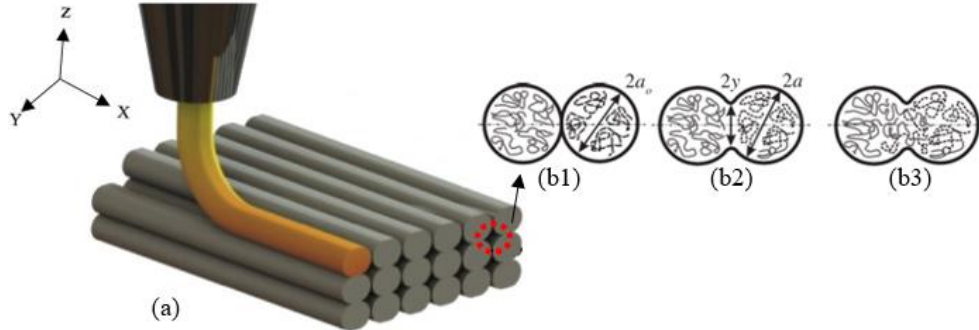


Figure 2.7. a) Printed sample geometry (Le Duigou et al., 2016) and bond formation between adjacent roads (b1) surface contact (b2) neck growth, (b3) diffusion at the interface, and randomization (Bellehumeur et al., 2004)

Wittbrodt and Pearce (2015) observed that stronger bonds were formed between the adjacent filaments as the extruder temperature is increased. Fang et al. (2017) optimized both extrusion temperature and the printing speed of the nozzle to obtain good metallurgical bonding between adjacent filaments. Hence, molten metal has sufficient energy to remelt the thin layer of the previously solidified filament.

Yan et al. (2000) was reported that layer thickness (LT) and road width (RW) should be adjusted so that while their multiplication (LT.RW) was maximized to improve heat transfer between adjacent roads, at the same time their ratio (LT/RW) should be minimized to decrease thermal resistance between the neighboring roads. Moreover, they found that a low convection coefficient must be provided in the forming environment to improve bonding between adjacent filaments.

Rankouhi et al (2016), Torres et al. (2016), and Li et al. (2018) stated that a decrease in layer thickness improved the strength of the printed structure. The reason is explained by Mazzanti et al. (2019) as a reduction of the voids with decreasing in LT for the resulting structure. However, Sood et al. (2010) specified that the strength of the printed part was adversely affected with lower layer thickness since it increases both the thermal gradient between the layers and the number of heating

and cooling cycles which further provoke distortion and residual stress on the object during the printing.

Structures printed with denser infill showed higher strength than partially filled samples as the void density decreases within the part according to Carneiro et al. (2015), Mahmood et al. (2017), and Rinaldi et al. (2018).

Similarly, Agarwala et al. (1996) advised an alternative material path to decrease void at the intersection region between infill and outline perimeter (contour) of the object as seen from Fig. 2.8.

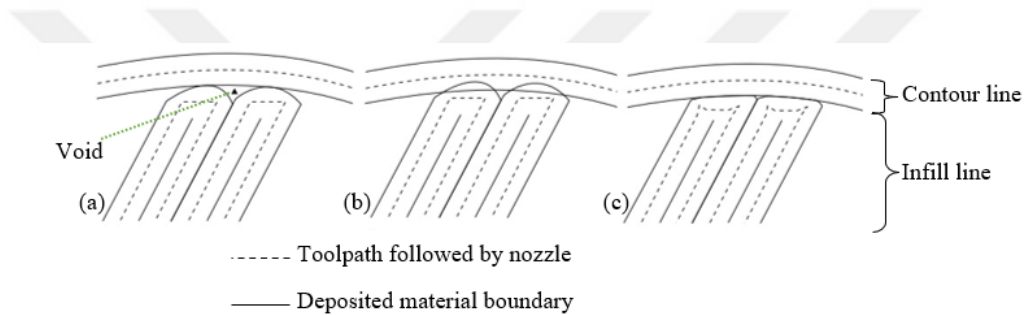


Figure 2.8. (a) Void formation at the intersection of infill and outline perimeter (contour), (b) minimization of the void with negative offset, and (c) minimization of the void with the altered tool path (Agarwala et al., 1996)

Fernandez-Vicente et al. (2016) printed tensile test specimens with different infill patterns such as line, rectilinear, honeycomb and determined that variation on the tensile strength was less than 5% for the applied infill patterns.

Durgun and Ertan (2014), Rezayat et al. (2015), and Afroze et al. (2016) investigated the effect of raster angle on strength of the printed part. The strength of the specimens printed with 0° raster angle was higher than the others (30° , 45° , 60° , and 90°) since the direction of the deposited filaments same as the direction of the applied load. This argument is also supported by Liu, Z et al. (2019) as while there is continuous fusion in the X direction or deposition direction, there is a discontinuity in the bonding of filament in Y and Z directions as seen from Fig. 2.7. (a). Therefore, bonding strength in the x-direction is higher than y and z directions.

Furthermore, Gleadall et al. (2018) evaluated the samples manufactured at different raster angles with repeated sequences such as (0/90), (0/60/120), and (0/45/90/135). They revealed that the filaments passing through the same points formed a rigid column in the structure from top to bottom. Therefore, the scaffolds printed with the order of (0/90) and (0/60/120) showed more resistance to the applied compressive loads in contrast to the structure built with the sequence of (0/45/90/135) whose filaments on different layers that don't pass through the same points.

Chacón et al. (2017), Arif et al. (2018), and Cantrell et al. (2017) surveyed the effect of print orientation on strength of the printed part. The samples were printed at flat, on-edge, and upright orientation as seen from Fig. 2.9. The strength of the samples printed at flat and on edge orientation was higher than specimens printed in an upright orientation. The result was consistent with the observation of Sood et al. (2010) since the higher number of layers in upright orientation caused an increase in both thermal gradient and residual stresses on the printed part.

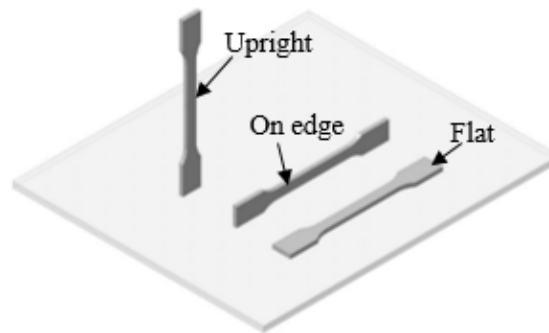


Figure 2.9. Build orientations of the part on platform

2.3. Materials and Required filament properties in FDM type 3D printers

Viscosity, adhesion behavior, and strength of the filament material are crucial features for successful FDM operation (Agarwala et al., 1996b).

Three main extrusion failures can be encountered based on filament material features in the extruder head of the FDM machine during the printing of a filament, which was given in Fig. 2.10.

The filament must have tight diametric tolerances ($\pm 0,05$ mm and lower) as inconsistent diameter makes trouble in feeding like in Fig. 2.10a (Website, 2020n).

Another factor that induces unsteady flow during printing is backflow that was shown in Fig. 2.10b. If the temperature in the backflow zone is lower than the melting temperature of the filament, the material may solidify and terminate the printing process. The most important factors that affect the formation of the backflow are the viscosity of the melt and the annular area between the diameter of the filament and the nozzle wall. When the melt flows into the nozzle, the reduction in cross-section of the nozzle triggers an increase in shear rate. If the melt material shows shear thinning behavior instead of Newtonian behavior against the rising shear rate, the viscosity of the melt decreases with increasing shear rate. Hence backflow risk will decrease. Further, the annular area between filament diameter and nozzle wall must be minimized as possible to decrease the possibility of backflow formation (Gilmer, et al., 2018).

The filament in a cold region of the liquefier, transfers the pressure applied by the feeding stepper, to melt for extrusion of the molten material from the nozzle. Both exerted force by feeding stepper and viscosity of the melt depending on nozzle geometry with relevant printing parameters causes a compressive force on the filament in the cold region. Therefore, the filament must have sufficient compressive modulus to apparent viscosity ratio to fully perform the piston function (Venkataraman et al., 2000). Otherwise, filament buckles so that the printing process adversely affected as seen from Fig. 2.10c.

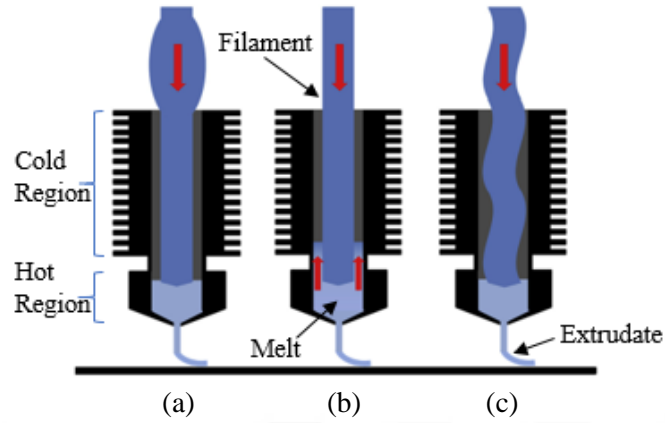


Figure 2.10. Melt extrusion failure types in FDM machine (Gilmer, et al., 2018)

Ideal conditions to print any material successfully in FDM or fused filament fabrication (FFF) system were presented briefly as the blue region in Fig. 2.11. According to Fig. 2.11, the material to be printed must have a certain viscosity value. Furthermore, the holding time of the material in the nozzle at a certain temperature during the printing process should be less than the time required for crystallization.

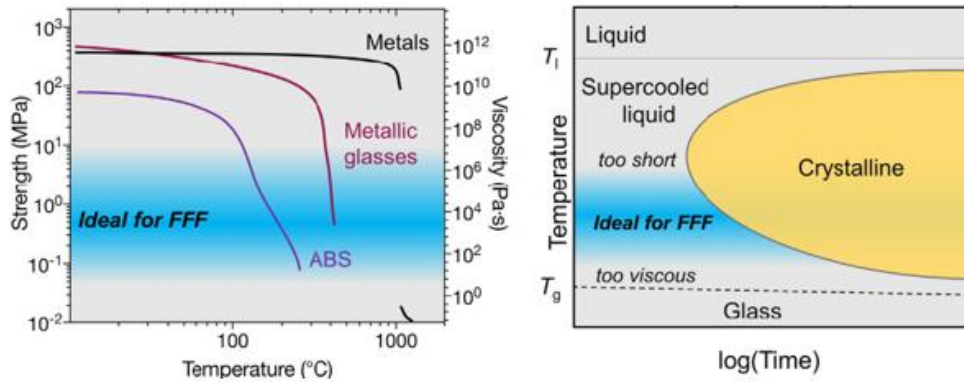


Figure 2.11. Ideal conditions for the printing of material in the FFF method (Gibson et al., 2018)

2.3.1. Commercial polymer materials printed in FDM type 3D printers

It was mentioned that FDM technology was designed for polymer-based materials. Available thermoplastic polymer materials used in FDM machines were listed with the characteristic feature and application areas in table 2.1.

Table 2.1. Characteristic feature and application area of the thermoplastic materials printed in FDM machine (Compiled from Stratasys datasheets and white papers, Website, 2020o)

Material	Characteristic Feature	Application Area
ABS-ESD7	<ul style="list-style-type: none"> Durable and prevents the formation of static electricity. 	Functional prototypes of cases, enclosures, packaging, jigs & fixtures for assembly of electronic components.
ABSi	<ul style="list-style-type: none"> Translucent. 	Light transmission or devices requiring flow monitoring in auto, aero, and medical industries.
ABS-M30	<ul style="list-style-type: none"> Greater tensile, impact, and flexural strength than standard ABS as layer bonding is stronger than ABS. 	Conceptual modeling, functional prototyping, manufacturing tools, and production parts.
ABS-M30i	<ul style="list-style-type: none"> High strength material property Biocompatible and sterilizable. 	Medical, pharmaceutical, and food packaging industries in addition to application areas of ABS M30.
ABSplus	<ul style="list-style-type: none"> Durable enough. 	Building 3D models and prototypes.
Antero 800NA	<ul style="list-style-type: none"> Excellent strength, toughness, and wear-resistant properties. High heat and chemical resistance. Low outgassing and high dimensional stability. 	Aircraft components exposed to jet fuel, oil and, hydraulic fluid, spacecraft parts that demand low outgassing and chemical-resistant industrial parts.
ASA	<ul style="list-style-type: none"> Aesthetics. Stable against the UV. Low flexural modulus, heat and chemical resistance. 	Outdoor and infrastructure cause of its UV-resistance. Also, the matte finish makes it ideal for attractive prototypes in consumer

		sporting goods, tools, automotive components, and accessories.
FDM Nylon 12	<ul style="list-style-type: none"> • The toughest nylon in AM and high fatigue resistance. • Lower flexural modulus. • Strong chemical resistance. • Lower aesthetics. • Moisture sensitive. 	Proper for repetitive snap fits, closures, and, vibration-resistant parts.
FDM Nylon 6	<ul style="list-style-type: none"> • Excellent strength and stiffness among the nylon materials. • Good impact strength. 	It is suitable for tools, prototypes, and production parts.
FDM TPU 92A	<ul style="list-style-type: none"> • Elastomer material with Shore A value of 92. • Extremely flexible, durable, and resilient. 	Flexible hoses, tubes, air ducts, seals, protective covers, and vibration dampeners.
Nylon 12 Carbon Fiber	<ul style="list-style-type: none"> • Highest flexural strength of any FDM thermoplastic. • Highest stiffness to weight ratio. 	Useful for strong but lightweight tooling applications and functional prototypes.
PC	<ul style="list-style-type: none"> • The moderate temperature resistance and mechanical strength. • Poor chemical resistance. • Moisture sensitive. 	Conceptual modeling, functional prototyping, manufacturing tools, and production parts.
PC-ABS	<ul style="list-style-type: none"> • Superior mechanical properties (impact resistance) and a heat resistance of PC. • The flexibility of ABS. 	Ideal for functional prototyping, tooling, and low-volume manufacturing.
PC-ISO	<ul style="list-style-type: none"> • Biocompatible and sterilizable. 	Food and drug packaging and medical device manufacturing.
PLA	<ul style="list-style-type: none"> • Higher stiffness than ABS. 	Early concept modeling and low-cost prototyping.
PPSF/PPSU	<ul style="list-style-type: none"> • The greatest heat and chemical resistance. • Mechanically superior material, the greatest strength. • Sterilizable. 	Applicable for caustic and high heat environments, under-hood automotive scenarios.
ST-130	<ul style="list-style-type: none"> • High heat and autoclave pressure resistance. • Removed easily after curing. 	It is sacrificial tooling material developed for facilitating the

		production of hollow composite parts.
Support Materials	<ul style="list-style-type: none"> • It can be removed manually or dissolving in a detergent bath. 	It was designed for the printing of complex structures with overhangs and small intricate openings.
ULTEM 1010 resin	<ul style="list-style-type: none"> • Excellent chemical and thermal resistance. • Biocompatible. • Lower impact resistance. 	It fits composite layup tools, high-temperature applications and, tooling that requires sterilization.
ULTEM 9085 resin	<ul style="list-style-type: none"> • High heat and chemical resistance. • The highest flexural strength, high tensile, and impact strength. • FST (flame, smoke, toxicity)-certified thermoplastic. 	Low volume production parts and functional prototypes, jigs, fixtures, end-of-arm tools, composite molds.

2.3.2. Composite materials developed for use in the FDM type 3D printers

Since the FDM technology is both low cost and customizable, it has attracted the attention of researchers and enabled the development of new materials such as polymers, composites, and blends different from existing commercial polymer materials. The materials used in FDM technology were given in Fig. 2.12.

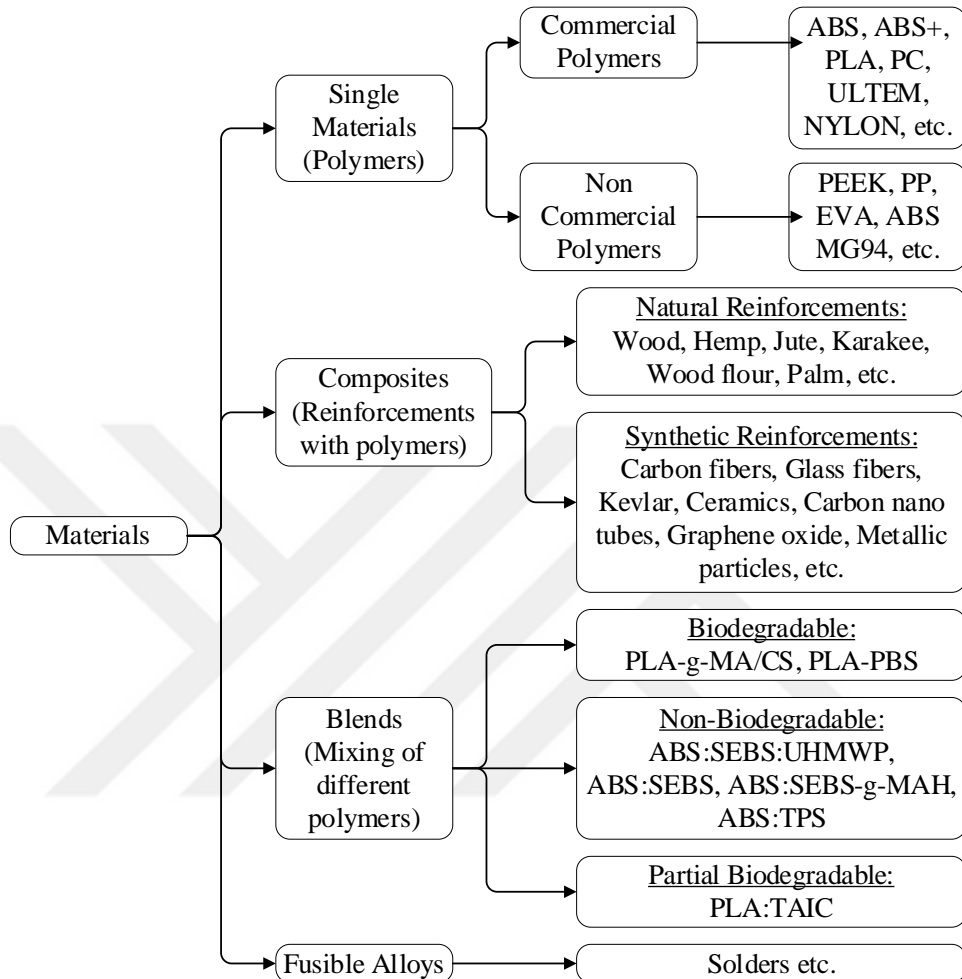


Figure 2.12. Materials used in FDM technology (Harris et al., 2019)

Studies associated with printing metal materials in the FDM technology were investigated to see the applied strategies or customizations to overcome encountered problems during the printing procedure of the metallic materials, as the initial aim of the study is to print Bi58Sn42 alloy using the FDM technology. Printed materials and applied methods for printing procedures were given in the following sections (2.5.2.1 and 2.6).

2.3.2.1. Fused deposition of metals (FDMet) with composite filaments

FDMet was developed as an alternative way to print metal parts in a FDM machine. The process consists of three main steps.

Initially rheology of the metal material is modified to meet the requirements of the FDM system by combining the metal powder with an appropriate binder, dispersant (to lower the viscosity), and surfactant. Compounding of the particles is a crucial process to achieve homogeneously dispersed particles in the produced filament. Subsequently, this mixture was extruded into filament and printed in the FDM machine. Lastly, debinding and sintering post-processing are made gradually to completely remove binders and obtain dense metallic structure without any structural damage (Agarwala et al., 1995; Agarwala et al., 1996b; Agarwala et al., 1996c). Supports must be used in hollow or thin-wall parts during the sintering process to prevent collapsing (Wu et al., 1998). The whole process is shown in Fig. 2.13.

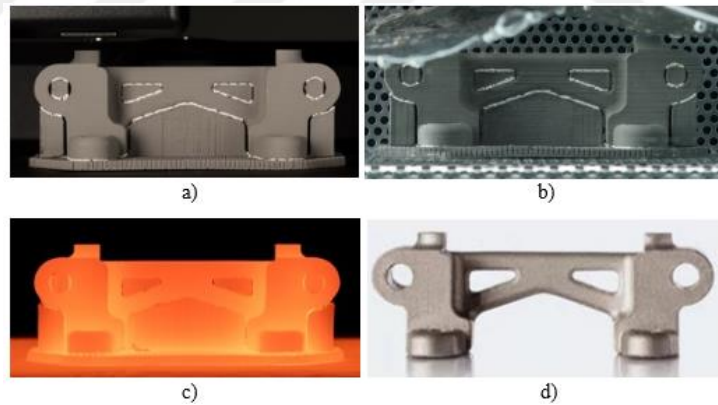


Figure 2.13. Steps of the extrusion based additive manufacturing; a) printed part (green part), b) debinding in a solvent, c) sintering and d) optional finishing processes (Website, 2020p)

Debinding is the most expensive and time-consuming process. Either solvent or thermal-based debinding method can be performed (Rane and Strano, 2019).

Shrinkage of the printed object is about % 10 - % 14 depending on the contents and components of the binder after post-processing. Components of the binder and their roles in filament making were presented in Table 2.2. Infiltration can be performed as an alternative to the sintering process to decrease the amount of shrinkage. But the melting point of the infiltrant must be lower than the main material (Greul et al., 1995).

Table 2.2. Components of the binder with their effects in filament making and thermal degradation temperatures of components (Agarwala et al., 1996d)

Component of binder	Effect of the component	Thermal degradation temperature range for binder removal
Polymer	Acts as a backbone	100 – 510 °C
Elastomer	Gives flexibility	275 – 500 °C
Wax	Viscosity modulator	200 – 500 °C
Tackifier	Promotes adhesion	190 – 475 °C

Fine (< 20 µm) and spherical powder particles were preferred to prevent clogging in the liquifier, to avoid interlocking among the powders, to reduce friction between particles, to facilitate flow from the nozzle, and to improve sinterability (Rane and Strano, 2019).

FDMet has attracted the attention of many researchers. Wu et al. (2002) mixed 58% volume SS17-4 particles with a binder system that involves poly-olefin, hydrocarbon resin, polyethylene, polybutylene. It was concluded that optimization of process parameters and machining is needed to obtain a better surface finish for the manufacturing of the complex part.

Masood and Song (2004) fabricated filament made from (30 % - 40%) volumes iron particles with P301 polyamide, surfactants, and plasticizers for producing the injection dies and inserts. It was stated that there was no need for any post processing since it was used in the production of plastic parts.

Similarly, Nikzad et al. (2011) also produced composite filaments for the manufacturing of injection tools and inserts. Copper and iron powders between 5 and

40 percent by volume were used for the production of the filaments. Components of the binder employed in the developed filaments were ABS, surfactant, and plasticizer. Developed composite materials with varying volume fractions have the potential to produce functional parts and rapid tooling applications.

Bandyopadhyay et al. (2006) composed 55% volumes silica powder with polypropylene, westo wax, tackifier, plasticizer, and elastomer for structural applications. AL 5052 infiltrated to the printed ceramic structure after debinding and sintering operations.

Li et al. (2010) developed a filament consists of 60% volume 316L stainless steel particles and 40% binder whose components are paraffin, high-density polyethylene, acetic acid-vinyl acetate copolymer, stearic acid. While shrinkage in the volume of the printed part was 29.31%, the density of the printed product was 73.75%.

Annoni et al. (2016) blended 79% volume AISI 630 powder with water-soluble polyethylene glycol. It was suggested that the amount of binder in the mixture should be optimized both to facilitate extrusion and to achieve good strength.

Ren et al. (2017) combined the 65% volume of copper powder with paraffin, polyethylene, stearic acid. The porosity of sintered parts was 8.5%.

Ryder et al. (2018) stirred 10, 15, and 23 weight percent of 420 stainless steel powders with ABS. Samples printed using the developed filaments were investigated for mechanical properties without being subjected to any post-processing such as debinding and sintering processes. It was found that increasing the particle content in the composite filament adversely affected the strength of the printed part since the bond between the metal and ABS particles was not good enough. The strength of the pure ABS part was higher.

Additionally, printable commercial composite materials via FDMet were given in Table 2.3.

Table 2.3. Available commercial printable metal materials (Website, 2020r; Website, 2020s)

Material	Application areas
17-4 PH stainless steel	Manufacturing machinery, chemical processing, food processing, pump components, valving, fasteners, jigs, and fixtures
316L stainless steel	<ul style="list-style-type: none"> Chemical and petrochemical processing, food processing, laboratory equipment, medical devices, marine applications, jewelry, power generation, petroleum refining, water treatment, pulp, and paper manufacturing
H13 tool steel	<ul style="list-style-type: none"> Extrusion dies, injection molds, hot forging dies, die casting cores, inserts, and cavities
D2 tool steel	Sheet metal fabrication, wear-resistant inserts, punches, and dies, shearing tools
A2 tool steel	<ul style="list-style-type: none"> Sheet metal fabrication punches and dies, forming prototypes
Alloy 625	<ul style="list-style-type: none"> Jet engines, navy marine applications, submarines, aerospace, extreme environment applications, nuclear reactors, substitute for tool steel, rapid temperature change, heat treat applications
4140	<ul style="list-style-type: none"> Jigs and fixtures, automotive, bolts/nuts, gears, steel couplings
Copper	<ul style="list-style-type: none"> Consumer and industrial electronics, heat exchangers, antennas, inductors

2.4. Direct printing of fusible alloys in FDM type 3D printers

Finke and Feenstra (2002) made printing experiments with Pb60Sn40. They found that print speed and extrusion speed should be compatible with each other to prevent irregularities in layer thickness and road width. It was also specified that accurate temperature control is required since the rheology of the semi-solid metal is affected by temperature variation. Moreover, segregation was observed during the experiments.

Kimball (2015) performed printing trials for the Sn79Bi21, Sn70Bi30, Sn85Zn15, Sn80Bi20, Sn76Bi20Ag<4, and Sn66Bi30Ag4. Brass, stainless steel, and aluminum nozzles were employed with coatings to prevent wearing at the nozzle during the extrusion. The best results were obtained at the anodized AL 6061 nozzle for Sn66Bi30Ag4 alloy. It was reported that the response of aluminum to thermal

cycling was better than the stainless steel and poor thermal conductivity of stainless steel caused clogging in the nozzle.

Chen et al. (2017) investigated the rheological behavior of Bi75Sn25 at different temperatures and shear rates using an oscillatory rheometer. Pressure was applied to extrude semi-solid alloy from the nozzle. The extruder head was modified by inserting a motor-driven grooved spindle inside the nozzle. Thus, both nozzle clogging was prevented and the viscosity of the slurry was controlled. The alloy was printed from a 1 mm nozzle diameter under pressure.

Jabbari and Abrinia (2018) modified the volume of the heated region on the extruder head. Coil and cartridge heaters were used to melt the Sn85Pb15, Pb60Sn40. To control the flow of the semi-solid alloy, filaments with fine globular microstructure were produced. Then the effect of extrusion temperature, extrusion multiplier, and print speed on the quality of the printed object was evaluated.

Daalkhaijav et al. (2018) printed gallium alloy using a syringe-type extruder with stainless steel needle after modifying its rheology by mixing it with metal particles that increase the viscosity and elasticity of the alloy.

Gibson et al. (2018) showed that metallic glasses can be printed on FDM printers like thermoplastics since they have a similar behavior (continuous softening upon heating) with polymers. Shell and solid parts were printed successfully from Zr44Ti11Cu10Ni10Be25 at room temperature. As the extrusion temperature of the alloy is 460 °C, extra heaters are mounted to the extruder head for better metallic bonding between the solidified layer and the newly deposited one.

Fang et al. (2017) developed a new metal fabrication technique called fused-coating-based additive manufacturing (FCAM). While the extruder head held fixed, the built platform was moving in the design. The alloy (Sn63Pb37) in the crucible was heated by induction and deposited to the platform in motion by applying pressure under an atmosphere-controlled environment. Shell structures were printed onto the copper-clad substrate with the designed system. During the printing trials,

only one parameter was changed to see the effect of the parameter while the others remained constant.

Wang and Liu (2014) utilized syringe-type extruder head to print Bi₃₅In_{48.6}Sn₁₆Zn_{0.4} whose melting temperature is 58.3 °C. The alloy was heated by coil heaters and ejected from the nozzle as droplets by applying pressure. There was no atmosphere-controlled environment. It was mentioned that oxidation of the alloy is negligible.

Lee (2008a) et al. employed a drop on demand (DOD) process that is categorized under material jetting in Table 1.1 to print Bi₅₈Sn₄₂ for microstructure applications. Molten metal droplets were ejected from a nozzle with 0.1 mm diameter by the oscillating motion of the piezoelectric actuator. A high-speed camera was utilized to observe the velocity and diameter of the droplets. They specified that pressure inside the molten metal chamber and the gap distance between the conical piston head and nozzle wall must be fixed to obtain an identical droplet.

Mireles et al. (2013) attempted to print six different solders containing Bi₃₆Pb₃₂Sn₃₁Ag₁, Bi₅₈Sn₄₂, Sn₆₃Pb₃₇, Sn₅₀Pb₅₀, Sn₆₀Bi₄₀, and Sn_{96.5}Ag_{3.5} through modification of the FDM parameters in an industrial level FDM 3D printer. It was reported that inconsistent deposition was observed during the printing of Sn-Pb solder at a varying flow rate and extrusion temperature. Besides coarsening of Sn-Pb solder within the hot region caused clogging in the nozzle. Similarly, the clogging also occurred during the deposition of Sn-Ag alloy due to Ag₃Sn formation within the nozzle whose melting temperature is higher than the set extrusion temperature. The depositing results showed that Bi₅₈Sn₄₂ and Sn₆₀Bi₄₀ can be deposited consistently. But more continuous lines with more consistent thickness were produced for Sn₆₀Bi₄₀ as its viscosity higher than eutectic Sn-Bi solder.

Warrier and Kate (2018) made trials for the printing of eutectic Bi₅₈Sn₄₂ alloy, non-eutectic Bi₄₀Sn₆₀, and Sb_{7.5}Sn₈₉ alloys. Initially to obtain continuous melt flow 2D maze structured were printed.

Later 3D specimens were tried. Extrusion temperature, bed (built platform) temperature, feed rate, extrusion velocity, layer thickness, and infill were optimized to print the Sn60Bi40. Both the extrusion velocity and feed rate were decreased to print the specimen. There was no successful print for the Bi58Sn42 alloy. Instead of printing Bi58Sn42 was poured into the PLA mold then post-processed. When the volume of the finished product was compared with 3D CAD data, there were 24,53 percent errors.

2.5. Evaluation of the metal printing in FDM systems

The studies related to the printing of low melting point alloys (fusible alloys) were mentioned in the previous section. The samples printed as a result of these studies were evaluated in this part.

It was determined that material extrusion (ME) or material jetting (MJ) category that involves continuous jetting and the drop on demand (DOD) methods were employed to print fusible (low melting point) alloys in the literature.

The samples manufactured by FDM, continuous jetting, and DOD printing methods were presented in Tables 2.4 to 2.6.

The inconsistent deposition was observed on samples printed with continuous jetting and DOD as seen from Tables 2.5 and 2.6. The reason for the inconsistent deposition in continuous jetting is explained by Lee, T. M. et al. (2008a). It was reported that there must be continuous material flow even if it is little or no printing is required. Also, they stated that it is hard to place the ejected droplets to the exact position when it is required.

Therefore, Lee, T. M. et al. (2008a) employed the DOD method to avoid the problems presented above. Nevertheless, the falling of the ejected droplets from a set height onto the build platform resulted from uneven size blob structures as seen from table 2.6. Furthermore, this non-uniform size solidified droplet formation (blobs) influenced the bonds between the neighbor droplets. As a result, both dimensional accuracy and strength of the printed part were adversely affected.

On the other hand, layer thickness, road width was more uniform for the samples printed with FDM as seen from table 2.4. Moreover, there was no interruption in bonding along the deposition direction in contrast to the DOD method.

Briefly, researchers employed alternative methods to print the metal materials as the investment costs of commercial metal 3d printers are high. It was recognized that FDM is one of the most preferred systems among the existing systems because it allows the printing of different materials and is inexpensive.

Two approaches were made to print the metal materials by FDM in the literature. The first approach is the use of fusible alloys directly in the FDM system by making some modifications to the system. The applied modifications included optimization of the process parameters in the slicer and modification of the hardware (heater type and nozzle material). In the second approach, the rheology of the material to be printed was customized via mixing it with binder systems to make it printable in the FDM system. Therefore, engineering-grade high melting point metals could be printed in FDM. However, post-processing such as debinding and sintering operations are required to obtain a 3d printed metal part in this approach. As mentioned before, these processes both increase the cost and extend the production time.

Since the material printed in the study was a fusible alloy, it was used directly in the FDM machine. Therefore, it wasn't require any debinding and sintering post-processing.

Table 2.4. Samples printed with FDM

Author	Material	Printed Sample
Mireles J. et al. (2012)	Bi58Sn42	
Kimball E. A. (2015)	Sn79Bi21 and Sn66Bi30Ag4 respectively	
Jabbari, A. and Abrinia, K. (2018)	Sn15Pb and Pb40Sn	
Daalkhaijav U. Et al. (2018)	Gallium alloy	
Warrier, N. and Kate, K. H. (2018)	Sn60Bi40	
Gibson M. A. et al. (2018)	Zr44Ti11Cu10Ni10Be25	

Table 2.5. Samples printed with continuous jetting

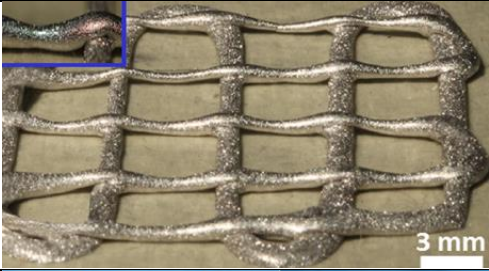
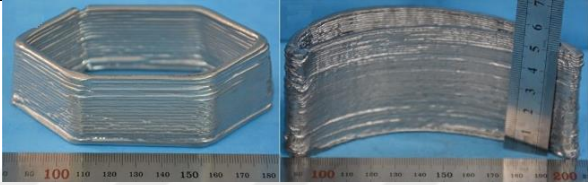
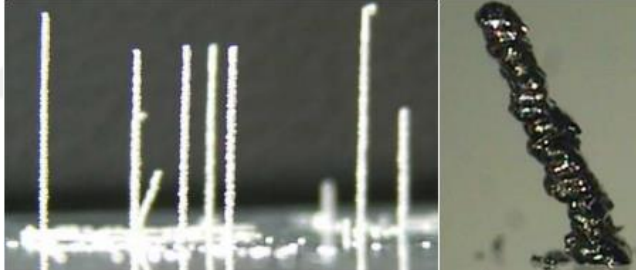

Author	Material	Printed Sample
Chen, W. et al. (2017)	Bi75Sn25	
Fang, X. et al. (2017)	Sn63Pb37	

Table 2.6. Samples printed with DOD

Author	Material	Printed Sample
Lee T. M. et al. (2008b)	Bi58Sn42	
Wang, L. and Liu, J. (2014)	Bi35In48.6Sn16Zn0.4	

2.6. Significance and Goal of The Study

Sheet metal forming process is commonly used in various industries to produce parts for white goods, computers, jewelry, construction, and vehicles. Typical forming processes can include bending, drawing, and stamping operations.

Conventional sheet forming processes requires dedicated tooling for each component. These processes are not suitable for low or medium-sized batch production (Desai et al., 2014). Mold production is both time-consuming and costly for low-volume production or rapid changing high-volume production during the development of a new product (Rosochowski and Matuszak, 2000).

Companies have need rapid and economical tooling during the product development period to release their product to the global market faster and efficiently (Rahmati, 2014).

Therefore, this study aims to benefit from additive manufacturing (AM) technology for fabricating sheet metal prototypes needed with a reduced product development period and cost in mold production.

In fact, some of the available AM technologies, such as selective laser sintering (SLS), selective laser melting (SLM), electron beam melting (EBM), BJ, and MJ, etc., can produce high strength molds in a relatively short time duration in contrast to traditional methods. However, these technologies are not applicable for most commercial applications due to their high costs, as seen from Fig. 2.14.

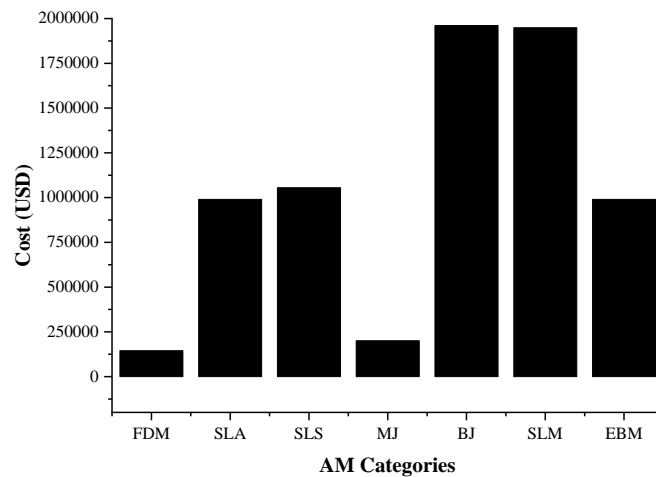


Figure 2.14. Machine Cost of the AM technologies (Website, 2020t)

We decided to use desktop type FDM 3D printer in this study as it is both low cost and allows customization.

Sheet metal part production volume is bigger than 10.000 parts in the traditional market. Therefore, molds were generally made from cast iron or steel, having the necessary strength for high volume production. However, as the molds' high investment costs can be compensated for high volume sized production, the stamping industry is forced to use alternative materials such as polymers, wood, and low melting point metals (fusible alloys) for increased product variants and economical low volume sized batch production (Pinto et al., 2008).

Early use of the fusible alloys goes back to 1940 for sheet metal forming tools. Tools can be used for several hundreds of pressings to shape steel, aluminum, and brass sheet metals. Additionally, they have advantages due to recycling them with minor loss (Anonymous, 1981).

BMW and Daimler Chrysler companies have used tools made from Bi58Sn42 alloy in the sheet metal forming process for prototype runs of 20-200 pressing (Website, 2020u).

Durgun et al. (2016) shaped cold rolled low carbon DC04 sheet steel using recyclable, low melting point Bi58Sn42 alloy molds. Molds and stamped sheet metal parts were evaluated for dimensional accuracy with a 3-D optical scanner. Experiments showed the potential to produce approximately 100 parts which are sufficient for the prototype phase (Müller and Sladojevic, 2001).

This study is interested in using low melting Bi58Sn42 alloy as a print material due to its success in low volume sheet metal parts production, as mentioned above. Therefore, the study examines the use of a low melting Bi58Sn42 alloy to create a 3D printed tool for rapid sheet metal parts production. In this context, the study firstly aims to develop a low melting alloy 3D printer. Then it aims to investigate the success of 3D printed low melting Bi58Sn42 mold for low volume sheet metal parts production with increased flexibility.

Briefly, developing a 3D printer for low melting Bi58Sn42 alloy may provide the necessary tool to support the need for low volume and low-cost sheet metal parts production with increased flexibility.

The critical part of the Ph.D. thesis is developing a 3D printing system for low melting Bi58Sn42 alloy. This may be achieved by customizing an open-source FDM-type 3D printer originally developed to print polymer materials. This stage also included test runs of the designed 3D printing machine to find and adjust optimum print settings for proper printing of Bi58Sn42 alloy. The print settings investigated were the printing speed, extrusion multiplier, extrusion temperature, etc.

After determining the optimum print settings for the calibration of the 3D printing machine, simple 3D molds were 3D printed using the Bi58Sn42 alloy. Then the printed tools were used in sheet metal forming press to test their life considering tears and wear on them. The tests were performed using aluminum sheets of 0.2- and 0.3-mm thicknesses.

The performance of the Bi58Sn42 mold manufactured in the 3D printer for the low volume sheet metal parts production was evaluated as follows:

- Initially, The Bi58Sn42 mold's dimensions were measured before starting the press forming operation.
- Then, the shaped aluminum sheets' dimensions were measured after every 10 pressing operations until the completion of 101 pressing numbers.
- Subsequently, the Bi58Sn42 mold's dimensions were measured again for dimensional changes after the 101 pressing operations.



3. MATERIALS AND METHODS

In this study, the performance of a mold produced by additive manufacturing (AM) was evaluated according to the dimensional change in the mold geometry depending on the number of pressings for low volume sheet metal forming process.

In this context, the study includes molds' production, the sheet metal forming process, the analysis of dimensional changes and issues on mold produced by AM according to the number of sheet metal forming processes.

While the male mold was additively manufactured in an open-source desktop type FDM 3D printer, the female mold was produced by casting due to the FDM hardware's low reliability and poor material characteristics of Bi58Sn42 alloy. Then aluminum alloy (AA) sheets were placed between the produced molds and formed. The reasons for manufacturing the female mold by casting are explained in detail in section 3.3.3.

The applied methodology's performance to form the AA sheets was assessed by measuring the dimensional change of the printed male mold exposed to pressure load during the sheet metal forming process.

The characteristics of the low melting point Bi58Sn42 (bismuth and tin) eutectic alloy were examined since it was used as a filament material in the FDM machine for the 3D printing of the male mold.

Customizations for the FDM machine were performed by evaluating performed 3D printing experiments using standard (unmodified) extruder and investigating similar studies given in the literature to print low melting point alloys.

The equipment used in this study was described for 3D printing, sheet metal forming, and performed dimensional measurements on the additively manufactured male mold.

The applied methodology, starting from the printing trials for the mold production and ends with the 3D printed mold's evaluation, was presented in detail. These include the modifications carried out in the commercial 3D printing machine

and essential object printing trials for the sheet metal forming mold production. Dimensional measurements performed on the 3D printed male mold after the sheet metal forming process was used to assess the mold's life for low volume sheet metal forming.

3.1. Characteristics of the fusible alloy

Bi58Sn42 fusible alloy, whose melting temperature is 135 °C, was employed as a filament material in FDM hardware for the mold's additively manufacturing in this research.

It is known that FDM has been developed for thermoplastic polymer materials that have a melting range. Therefore, polymers are at semi-solid conditions within the hot zone of the liquefier during the printing process.

On the other hand, the Bi58Sn42 is a eutectic alloy and has a specific melting temperature.

Besides, it doesn't have any region that involves both solid and liquid phases simultaneously, as seen from the blue dash line in Fig. 3.1. While it has only a liquid phase above the melting temperature, it is in a solid phase below the melting temperature.

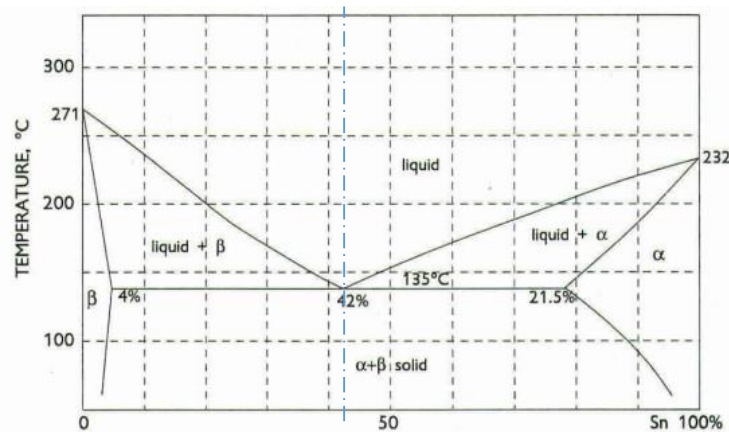


Figure 3.1. The Bismuth – Tin phase diagram (Website, 2021a)

The ideal viscosity range for a material employed as a filament material in FDM type 3D printers was shown in Fig. 2.11. While the ideal viscosity range must be between 40 and 40. 10^6 (Pa.s) in Fig. 2.11, the viscosity of the Bi58Sn42 is under 100 mPa.s (0.1 Pa.s) as given in Fig 3.2. It is quite low.

Furthermore, the viscosity of the Bi58Sn42 continues to decrease depending on the increase in shear rate (Lee et al., 2008a).

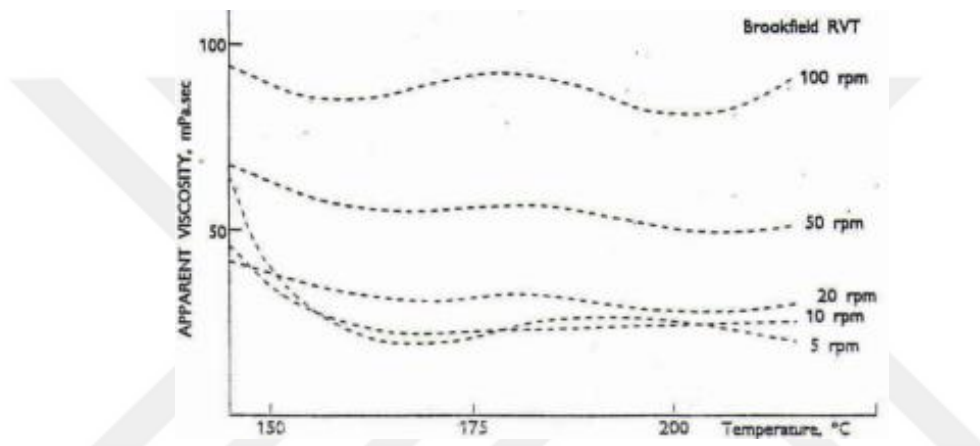


Figure 3.2. The viscosity of the Bi58Sn42 alloy depending on the temperature and rotational speed of the rheometer (Website, 2021a)

Due to the low reliability of the utilized FDM hardware with no feedback system and poor material characteristic of the fusible (Bi58Sn42) alloy, it was decided to produce the female mold by a casting process. Unfortunately, it was impossible to print the female mold additively in the FDM machine. Hence there was no alternative option other than using the casting process to produce the female mold.

Moreover, the object's built time to be printed from Bi58Sn42 alloy in the FDM printing machine was longer than printing polymer materials.

Technical specifications of photopolymer resin used for the production of female mold were given in Tables 3.1.

Table 3.1. Technical specification of photopolymer resin (Website, 2021b)

Net weight	1 L
Color attribute	Translucent
Color name	Clear
Elongation at Break	14.2 %
Liquid Density	1.100 g/cm ³
Shore Hardness	79D
Solid Density	1.184 g/cm ³
Tensile Strength	23.4 Mpa
Viscosity	552 mpa.s (25 °C)

0.2 mm and 0.3 mm thick AA 8006 sheets were shaped with the molds produced in the study. The mechanical properties of the aluminum alloy sheet are given in Table 3.2.

Table 3.2. Mechanical properties of AA 8006

Yield Strength (N / mm ²)	71
Tensile Strength (N / mm ²)	119
Elongation (%)	39.5

3.2. Customization of FDM extruder

The studies related to the printing of metal materials other than polymer materials at the FDM type 3D printers were mentioned in sections 2.3.2.1, 2.4 and 2.5.

Three main categories were determined to define the FDM type 3D printers' customizations in the existing literature, and these customizations were given in Table 3.3.

Table 3.3. Classification of the customizations made on FDM type 3D printers

Customization category	Altered region
Hardware	Extrusion system
	Heating system
	Nozzle design
Software	Optimization of printing parameters if open-source printers are used
Material	Improvements made on the printability of the material by mixing it with the binder system

Alternative extrusion designs utilized on desktop type FDM 3D printers were illustrated in Fig. 2.1.

While piston-type extrusion systems are used to print dense (high-viscosity) materials such as pastes, clays, etc., screw-based extrusion systems are used to print the semi-solid materials that involve both solid and liquid phases in the hot zone of the extruder head.

In screw-based extrusion systems, the rotation motion of the screw breaks the bond between the small solid particles so that agglomeration and clogging in the nozzle are eliminated.

When the samples printed from low melting point alloys using these alternative extrusion systems are examined from Tables 2.4, 2.5, and 2.6, it was seen that the model manufactured with the wire feeding mechanism was more uniform than the piston or screw-based systems. Irregularities in the sample's dimensions produced with the drop on demand (DOD) system were observed. Also, the bonding among the neighbor droplets was weak in the structure printed.

Since the material to be printed has low viscosity and shows eutectic phase behavior, a filament-based extrusion system was preferred in this study. Therefore, no customization has been carried out for the extrusion system, and the existing wire feeding system of the 3D printing machine was utilized in this study.

A heater cartridge is a standard component to melt the filament for desktop-type FDM 3D printers. They are available in the market as 12V/24V-40W and 12V-

50W powers. A coil or induction heater was also employed instead of a heater cartridge to melt the fusible alloy. In literature, Mireles et al. (2013), Wang and Liu (2014), Jabbari and Abrinia (2018) employed coil heaters instead of a heater cartridge to have a bigger melt chamber. Besides, Gibson, M.A. et al. (2018) mounted an extra heater near the nozzle to improve the metallic bond between the solidified previous layer and printed layer as the melting point of the material was 460 °C. Therefore, both the heater cartridge and coil heater were also employed to melt the Bi58Sn42 alloy in our research.

Kimball E. Andersen (2015) mentioned that the nozzle material's thermal conductivity affects the printing process. Therefore, different nozzle materials such as brass, stainless steel, and aluminum were employed to print the fusible alloys. Nozzles were manufactured according to the dimensions of the e3d nozzle design (Website, 2021c). Similarly, the same nozzle materials with the exact geometric dimensions were also used in our research.

The most commonly optimized parameters in the performed studies were determined as printing speed (nozzle moving speed during the printing), extrusion multiplier (modification factor for the automatically calculated material feed rate), and extrusion temperature. Therefore, these parameters were set and tuned optimally to achieve the best performance to print the Bi58Sn42 successfully.

In this research, two types of extruders were used for the printing trials. While one is a commonly handled design on the market, the other is a customized print head that includes a coil heater to have a bigger melt chamber. The images of the customized and commonly utilized extruder designs are presented in Figs. 3.3 and Fig.3.5, respectively.

The K-type thermocouple was connected directly to the nozzle of the customized extruder for monitoring the temperature at the nozzle during the printing process. PID controller was also used to control the extrusion temperature accurately. The image of the PID controller and its technical features were given in Fig. 3.4 and Table 3.4 respectively.

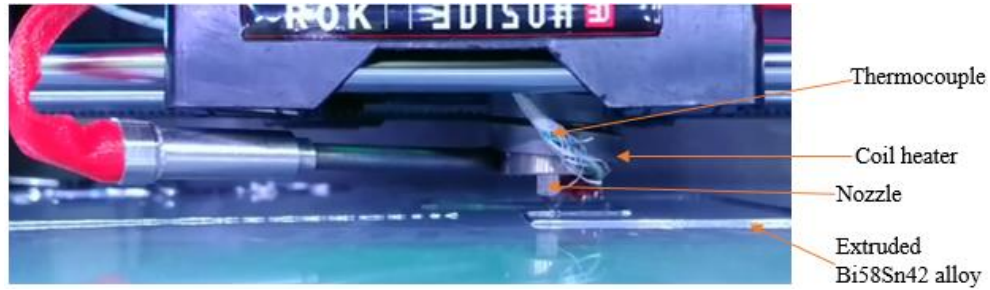


Figure 3.3. Image of the customized extruder



Figure 3.4. Image of the EMKO ECO PID controller

Table 3.4. Technical specification of the EMKO ECO PID controller (Website, 2021d)

Sensor Inputs	TC, RTD Thermocouple (TC): J, K, R, S and T(IEC584.1)(ITS90) thermoresistance(RTD) PT-100 (IEC751)(ITS90)
Scale	FeCuNi -200°C,900°C NiCrNi -200°C,1300°C Pt13%Rh 0°C,1700°C Pt10%Rh 0°C,1700°C CuCuNi -200°C,400°C PT100 -200°C,650°C PT 100 -199.9°C,650.0°C
Accuracy	Thermocouple (TC):($\pm 0.25\%$ of full scale or $\pm 3^{\circ}\text{C}$, which one is greater) ± 1 digit max. Thermoresistance (RTD):($\pm 0.25\%$ of full scale or $\pm 2^{\circ}\text{C}$, which one is greater) ± 1 digit
Control Form	Programmable On / Off, P, PI, PD, and PID
Reading Frequency	10 readings per second

3.3. Printing experiments for male mold production and casting process for the production of the female mold

This section provides equipment employed for the printing experiments with the applied methodology to print a male mold and performing casting process.

3.3.1. Experimental equipment used for the printing trials

Printing experiments were performed using 3DISON PRO that is a desktop type FDM 3D printer. It has a dual extruder head. While one of the extruders is utilized to print the support structure, the remaining one is used to print the main form. It builds the 3D part in an open atmosphere.

There is no monitoring and feedback system in the 3D printing machine to automatically adjust the distance between the nozzle and build platform like industrial 3D printers with build platform leveling. The correct distance considering the leveling is adjusted manually by the user using the four knobs at the corners of the build platform before the printing commences and it is set.

PLA, ABS, Nylon, Flexible-plastic, PVA, Heat-resistant PLA, Wood in the form of dust chip fibers, Stone in the form of dust, Engineering-plastic (Thermoplastic), etc., can be employed as a printing material. Moreover, metal paste such as silver, bronze, copper, chocolate paste, etc., can also be printed. However, time-consuming post-treatment must be applied to the metal pastes to obtain fully dense metal parts.

The printer system and its technical features were given in Fig. 3.5 and Table 3.5, respectively.

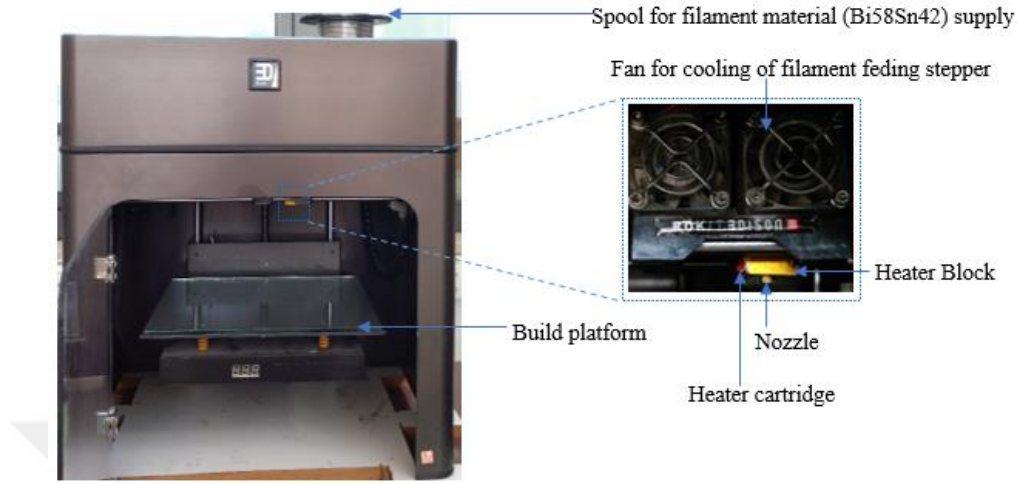


Figure 3.5. 3DISON PRO desktop type FDM printer

Table 3.5. Technical features of the 3DISON PRO 3D printing machine (Website, 2019d)

Build size	X:270, Y:200 and Z:245 mm
Printing speed	40~1000 mm/sec
Layer thickness	100~300 microns recommended
Positioning precision	X, Y:11 micron, Z: 2.5 micron
Extruder Temperature	200 °C~300 °C
Heat Bed Temperature	70 – 80 °C for PLA, 145 – 150 °C for ABS
Supported File format	STL, OBJ
Connectivity	Stand-alone SD card or USB cable

Simplify3d was utilized during the printing trials as a slicer software that converts 3D CAD data to build data that involve g-codes, feed rate, printing speed, etc. (Website, 2021e).

3.3.2. Experimental procedure for the printing experiments

Print settings in Simplify3D software were optimized to manufacture the desired part geometry. Optimized parameters and their limit values during the performed 3D printing experiments were presented in Table 3.6.

Table 3.6. Optimized print settings and their limits

Parameters	Limit Values (Minimum - Maximum)
Extrusion Temperature (ET)	140 - 200 °C
Extrusion Multiplier (EM)	1 - 4
Printing Speed (PS)	100 - 1300 mm/min
Road Width (RW)	0.3 – 1.02 mm
Infill Rate	0 % - 100 %
Printing Modes	Vase mode – Start stop printing mode

Initially, printing experiments were performed to print uniform extruded road as Finke and Feenstra (2002) mentioned. In this context, EM, ET and PS were optimized simultaneously to print simple geometric shapes such as line, maze and multi-layered shell structures.

Later printing experiments were carried out to print single-layered solid samples such as square and circle objects. RW, IR, EM, ET and PS were optimized to print the solid samples.

After printing of multi-layered solid samples, the 3D printing experiments were completed.

Optimum print settings determined in performed experiments were also used for the next 3D printing experiment and optimization of print settings continued until the desired sample geometry was built.

It was observed that the different outcomes were obtained during the performed repetitive 3D printing experiments in the same print settings. This was due to the poor material characteristics of Bi58Sn42 alloy and low reliability of the available FDM hardware. Therefore, the 3D printing experiments couldn't be performed systematically.

3.3.3 The manufacturing of the female mold by casting process

In this study casting process was applied to produce a female mold due to the printability of the Bi58Sn42 alloy was adversely affected from the following reasons:

- There were deviations in the extruded road's size during the performed 3D printing experiments due to the filament feeding into the nozzle didn't occur according to the pressure changes in the nozzle. This situation was also reported by Ramanath et al. (2008).
- As the Bi58Sn42 alloy's viscosity is quite low, deposited road cannot maintain its shape and it fuses with the newly deposited road. Therefore, dimensional accuracy and surface roughness of the printed sample was bad.
- Deviation on the extruded road's size was also occurred due to the acceleration and deceleration caused by the extruder's sharp turning movements depending on the part geometry.

As a result, the reliability of the printing process was low, since the above-mentioned reasons cumulatively affected the printing of the other layers.

For the production of female mold by casting, initially, dimension of the 3D printed male mold was measured then it was offset by the sheet metal thickness and the mold geometry was redrawn in a CAD program to be used in SLA type 3D printer. Later, the printed female mold was placed to ultraviolet (UV) light chamber for a half hour to complete polymerization. After complete curing of the 3D printed mold, the molten Bi58Sn42 alloy was poured into the 3D printed female mold. Lastly, surface roughness of the 3D printed mold was improved by milling operation. The performed casting process was illustrated in Fig. 3.6. In addition, technical features of the SLA 3D printer and UV light chamber were given in Tables 3.7 and 3.8 respectively.

3. MATERIALS AND METHODS

Hulusi DELİBAŞ

Table 3.7. Technical features of the Anycubic Photon S (Website, 2021f)

Light Source	UV integrated light (wavelength 405nm)
XY DPI	47um (2560*1440)
Y axis resolution	1.25um
Layer resolution	25 ~ 100um
Printing speed	20mm/h
Printing volume	115mm x 65mm x 165mm (4.52" x 2.56" x 6.1")
Printing material	405nm photosensitive resin

Table 3.8. Technical features of the WANHAO UV LED CURING BOX (Website, 2021g)

LIGHT SOURCE	UV
POWER(W)	200
WAVELENGTH	405 nm
EMITTING AREA(LxWxH)	32 x 20 x 20 cm
PERSPECTIVE SCREEN (LxW)	15 x 6 cm
BULB WARRANTY	2000 Hours



Figure 3.6. Applied casting process for the female mold production

3.4. Sheet metal forming process

The sheet metal forming process was performed with the Instron 8801 axial fatigue test device located in the laboratory of the Department of Mechanical Engineering at the Çukurova University.

The device's general view and technical specifications are presented in Fig. 3.7 and Table 3.9 respectively.



Figure 3.7. Instron 8801 axial fatigue test device

Table 3.9. Technical specifications of the Instron 8801 axial fatigue test device (Website, 2021h)

Dynamic load capacity	Double-acting servo-hydraulic actuator with force capacity up to ± 100 kN
Actuator stroke	150 mm of usable stroke
Configuration	Twin-Column High-Stiffness Load Frame with Actuator in Lower Table
Load Cell	Fatigue-Rated Load Cell Mounted to Upper Crosshead with Capacity to Suit Actuator
Load Weighing Accuracy	$\pm 0.002\%$ of Load Cell Capacity or 0.5% of Indicated Load, whichever is Greater - Down to $1/250$ th of Full Scale
Hydraulic Pressure Supply	207 bar

Both male and female molds are mounted to the crossheads of the testing device using magnets. Then aluminum sheets were shaped by the upward motion of the lower crosshead with 80 mm/min speed. The applied sheet metal forming process was illustrated in Fig. 3.8.

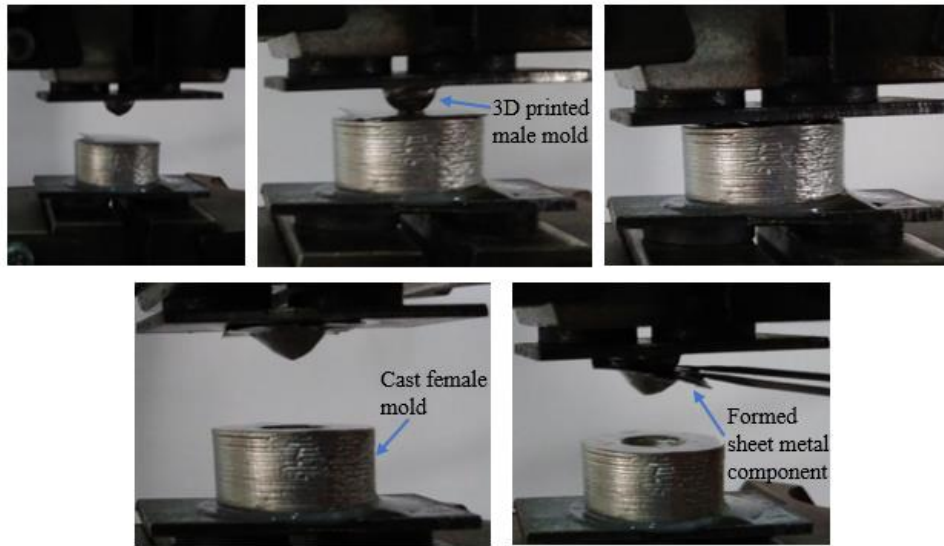


Figure 3.8. Press forming operation for low volume sheet metal parts production

3.5. Evaluation of the dimensional change on printed and cast male molds according to the number of sheet metal forming

After the sheet metal forming process, the dimension of the 3D printed mold exposed to compression load was measured using compact and contact type of coordinate measurement machine (CMM) (Romer absolute arm compact RA-7312) located in the laboratory of the Mechanical Engineering Department of Çukurova University. The measurements were taken from the 3d printed mold after successive completion 101 sheet metal forming process which is sufficient for low volume sheet metal parts production. During the measurements of the 3D printed mold, a 3 mm probe of the CMM was utilized. However, it was determined that the 3 mm probe made an incorrect measurement as it could not fully grip the base of the 3D printed

sphere. Therefore, measurements were performed using electronic caliper with 10 micron precision.

The Romer absolute arm coordinate measurement machine's general view and technical features are presented in Fig. 3.9 and Table 3.10 respectively.



Figure 3.9. Romer absolute arm compact coordinate measurement machine

Table 3.10. Technical specifications of the Romer absolute arm coordinate measurement machine compact RA-7312 (Website, 2021i)

Range of measurement device	1.2 m
Single point repeatability	0.014 mm / 0.0006 in
Volumetric accuracy	± 0.025 mm / 0.0010 in
Volumetric probing error (Form error of the CMM or MPE_p)	8 μ m
Maximum permitted error of length (MPE_e)	$5 + L / 40 \leq 18$ μ m



4. RESULTS AND DISCUSSIONS

The studies performed in the literature related to 3D printing the fusible (low melting point) alloys in FDM-type 3D printers were expressed in sections 2.6 and 2.7. In addition, the problems encountered in these studies and the customizations made by the researchers were also assessed. Then, the customizations have been made into the available extruder to print the Bi58Sn42 alloy according to the issues experienced during the performed printing experiments using the available standard extruder, and implemented customizations were explained in section 3.2.

In this section, a differential scanning calorimetry (DSC) analysis of the Bi58Sn42 alloy was given. Then performed 3D printing trials to print the sheet metal forming mold using both standard (unmodified) and customized extruders were presented in detail. Finally, the performance of the 3D printed mold was evaluated in the press forming operations.

4.1. Differential scanning calorimetry (DSC) analysis of the Bi58Sn42 alloy

The Bi58Sn42 alloys with a diameter of 1.67 and 2 mm supplied from two different manufacturers were utilized during the 3D printing trials in this study.

DSC analysis was performed to determine both the Bi58Sn42 alloy's melting range (the temperature at which melting begins and melting point) and the melting temperature of the compound that may form due to oxidation as the Bi58Sn42 alloy was 3D printed in an open atmosphere. Therefore, it was intended to find the Bi58Sn42 alloy's optimum extrusion temperature for the prevention of clogging in the nozzle during the 3D printing if the formed oxide compound's melting point is higher than the set extrusion temperature throughout the 3D printing of the Bi58Sn42 alloy in the open atmosphere.

In this context, the DSC analysis was implemented onto the Bi58Sn42 alloy, which was provided from two different manufacturers, heated up to 350 °C on a hotplate in an open atmosphere to examine whether an oxidized compound is formed

that can melt at a higher temperature than the set extrusion temperature and the Bi58Sn42 alloys.

The DSC analysis was performed at a heating rate of 10 K/min in Nitrogen in the temperature range of 25 - 350 °C. So, the DSC graph belonging to the Bi58Sn42 alloy was given in Fig. 4.1.

For the Bi58Sn42 alloy with a diameter of 1.67 mm, the melting start at 143.65 °C, and the melting temperature is 144.75 °C.

For the Bi58Sn42 alloy with a diameter of 2 mm, the melting start at 144.11 °C, and the melting temperature is 144.60 °C.

For the Bi58Sn42 alloy heated to 350 °C in the open atmosphere, the melting start temperature is 142.58 °C, and the melting temperature is 143.24 °C.

Similar results were obtained in the literature (Kamal et al., 2006) and no severe changes were observed in melting points of the materials prepared in different environments.

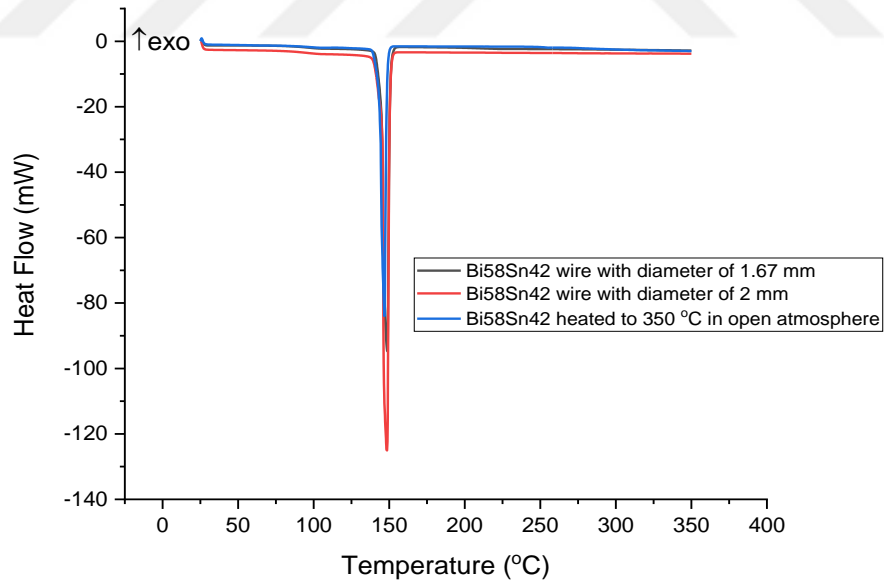


Figure 4.1. DSC tracks for the Bi58Sn42 alloy heated to 350 °C in the open atmosphere and the Bi58Sn42 alloys with a diameter of 1.67 and 2 mm supplied from two different manufacturers

4.2. 3D printing experiments performed to manufacture sheet metal forming mold

The additively manufactured objects at the end of the performed 3D printing trials according to the set print settings such as extrusion temperature (ET), extrusion multiplier (EM), printing speed (PS), layer thickness (LT), road width (RW) etc., in the Simplify3D (slicer) were given for both standard (unmodified) and customized extruder in detail at this section.

The 3D printing experiments commenced with the printing of simple single-layer geometric shapes like lines, maze contours. Then the experiments were carried out to print the single-layer fully dense (100 % infill rate) objects, and the 3D printing experiments were completed with the printing of multilayer objects.

4.2.1. 3D Printing trials performed using the standard (unmodified) extruder

Finke and Feenstra (2002) specified that the movement speed of the nozzle during the printing must accommodate the movement speed of the filament feeding roller so that the uniform line was printed. Therefore, the printing trials were performed to print the uniform lines by adjusting the extrusion multiplier, printing speed, and extrusion temperature settings in Simplify3D software.

Since the available extruder's barrel hole diameter is designed for the 1.75 mm filament diameter, the available filament diameter was initially reduced from 2.00 mm to 1.75 mm using manual wire drawing dies. Later, the wire with reduced diameter was inserted into the extruder to test the melting capability of the available heater cartridge having a 40-Watt (W) and 24 voltage (V) supply. 40W of the power was sufficient to melt the alloy. However, melt flow from the nozzle was non-uniform due to the varying filament diameter.

Therefore, instead of reducing the existing 2 mm filament diameter, it was decided to make a larger diameter barrel to print the 2 mm filament. In this context, a 20 mm long barrel was designed and produced, made of stainless steel having a metric 6 mm (M6) outer screw diameter and 4 mm inner hole diameter.

Also, a politetrafloretilen (PTFE-Teflon) tube with a 2.3 mm hole diameter was inserted into the barrel to reduce friction between the filament and the barrel wall during the feeding. Then, the barrel assembly was mounted to the 3D printer.

Currently available desktop type 3D printer came with 0.2, 0.4, and 0.6 mm brass nozzle options. In addition, a few MK-8 brass nozzles with 0.2 mm holes were obtained and drilled at different diameters (0.8, 1.00, 1.20, and 1.40 mm) to facilitate the flow of the fusible alloy through the nozzle.

Experiments were initiated for the printing of 60 mm long lines using 1.02 mm diameter brass nozzle according to the extrusion temperature (ET) settings of 140, 143, 145 °C, extrusion multiplier (EM) of 1.4, 1.5, 1.6 and printing speed (PS) of 150, 200, 250, 300 mm/min.

The printed lines' layout and corresponding print settings for each trial were given in Fig. 4.2. The snapshot shown in Fig. 4.2 was taken from the screen view of Simplify3D software.

The start point of each line and extruder movements were also illustrated in Fig. 4.2. While the cyan-colored circles represent the start point of each line, dotted thin lines (dash lines) represent the extruder movements.

Since the "Optimize start points for fastest printing speed" option was chosen on the Simplify3D, the simulation process was generated as in Fig. 4.2 to optimize the print time.

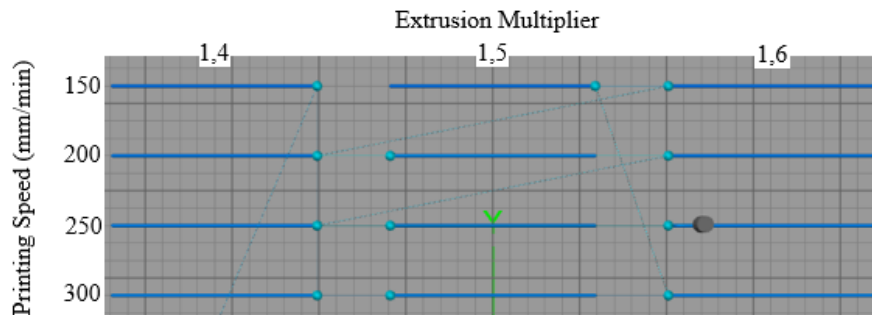


Figure 4.2. The layout of the lines printed on the built platform with different process parameters

The quality of printed lines can be seen from Figs. 4.3 to 4.5.

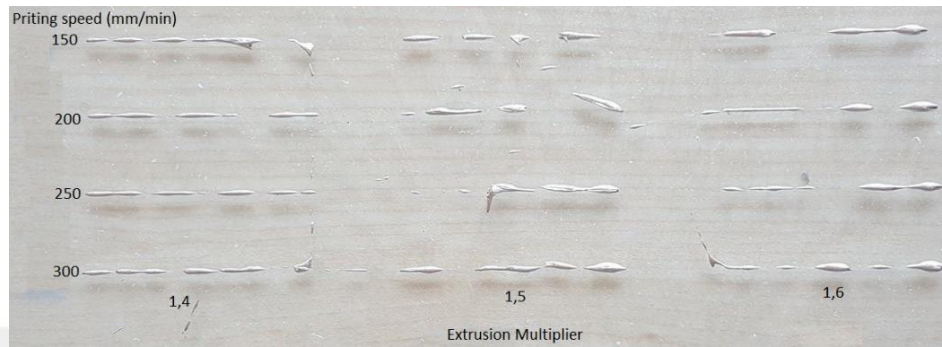


Figure 4.3. Lines printed in the ET of 140 °C using 1.02 mm diameter brass nozzle

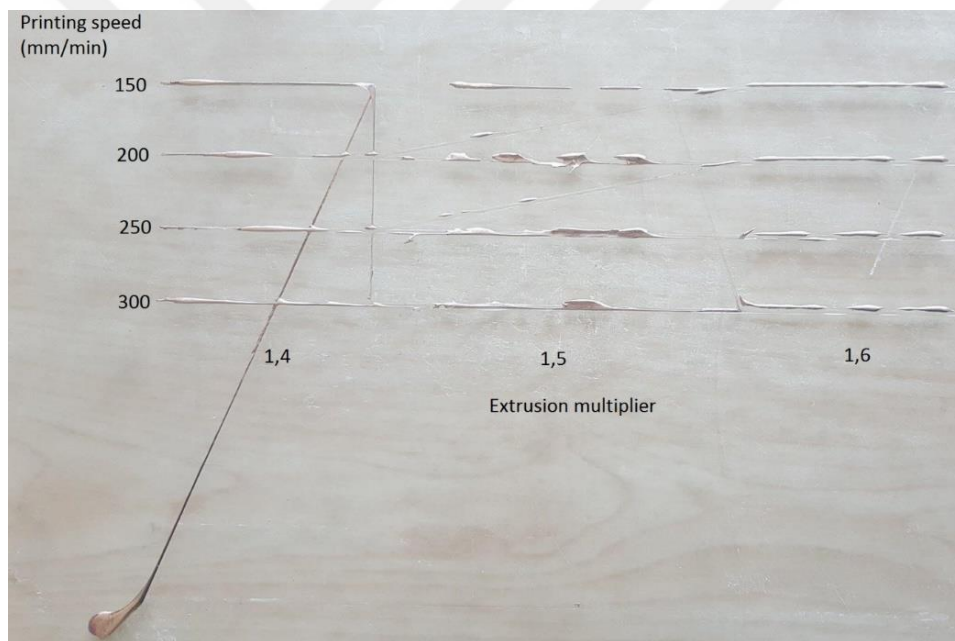


Figure 4.4. Lines printed in the ET of 145 °C using 1.02 mm diameter brass nozzle

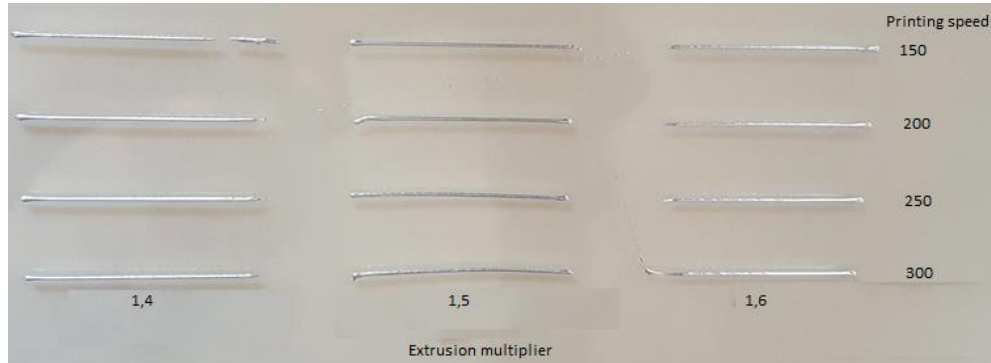


Figure 4.5. Lines printed in the ET of 143 °C using 1.02 mm diameter brass nozzle

As the Bi58Sn42 alloy is in the liquid phase above the melting temperature and the extruded alloy would not maintain its shape during the 3D printing at a temperature above its melting point, the first trial was performed at 140 °C of ET setting just below its melting point. The melt flow was insufficient and resulted in a non-uniform line structure, as seen from Fig. 4.3. For this reason, ET was increased to 145 °C to obtain continuous melt flow for the second trial. There was leakage from the nozzle during the printing trial at 145 °C of the ET setting, as seen in Fig. 4.4, and this adversely affected the printing process. Hence, ET was decreased to 143 °C to prevent leakage in the subsequent trial.

143 °C ET setting provided a much better line structure than the other performed printing trials, as seen from Fig. 4.5. In addition, the set EM and PS values were compatible with 143 °C extrusion temperature to print a straight line from the 1.02 mm nozzle. Thus, a more complex shape such as a shoe-in Fig. 4.6 was printed using the ET setting of 143 °C, EM of 1.4, and PS of 200 mm/min.

During the performed printing trials, melt flow was non-uniform. Sudden risings in mass flow rate led to the molten filament blobs adhering to the nozzle's outer cone. Further, the blobs adhered to the nozzle surface grew until they couldn't hold on the nozzle surface, then dropped and stuck to the build platform together with the melt flow from the nozzle. Consequently, fluctuation in the printed road size (layer thickness and road width) occurred. The non-uniform road size also caused

rubbing of the nozzle to the previously printed (solidified) layer during the printing of a second layer. Accordingly, the previously printed pattern separated from the built platform, as seen from Fig. 4.6.

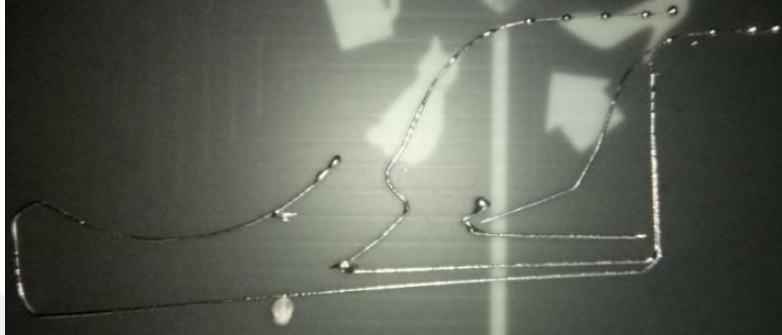


Figure 4.6. The shoe geometry printed at 143 °C of ET, PS of 200 mm/min, EM of 1.4, LT of 0.2 mm using 1.02 mm diameter brass nozzle

The above-performed printing experiments have provided reasonably suitable set parameters which could be used for the subsequent printing trials. In this regard, a square with dimensions of 40×40×0.2 mm was tried to be printed using EM of 1.4, PS of 200 mm/min, and ET of 143 °C, as highlighted in Fig. 4.7a. However, as over-extrusion occurred for these adjusted print settings, printed geometry was adversely affected. For this reason, the printing process was canceled. In addition, EM was decreased from 1.4 to 1 to prevent adherence of blobs to the nozzle's outer cone. But this time, under-extrusion occurred in the printed square sample, as seen from Fig. 4.7b.

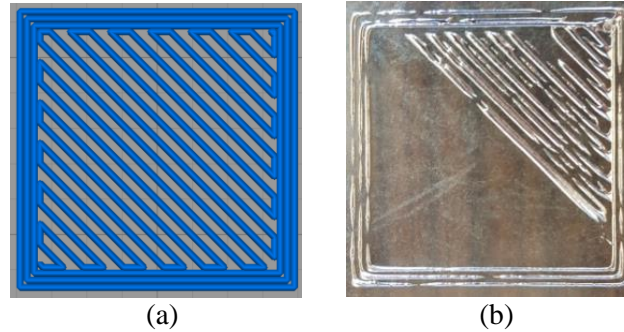


Figure 4.7. a) Simplify3D image of the square object to be printed, b) Square sample printed in ET of 143 °C, PS of 200 mm/min, EM of 1, LT of 0.2 mm using 1.02 mm diameter brass nozzle

The experiment was repeated by setting the EM from 1 to 1.3 while the other test parameters remained constant. It is expected that increasing the material flow rate by setting EM to a higher value may provide better printing results. However, the increasing material flow rate for the same distance (or printing gap) between the nozzle and built platform caused the blobs of filament materials around the nozzle. As a result of this, the printing of the square was not achieved. The experiment was repeated by setting the EM to 1.15. Contrary to the expectations, the resulting structure in Fig. 4.8a was worse than obtained with the EM setting of 1 in Fig. 4.7b. Material adherence to the outer cone of the nozzle was also observed.

The gap between the nozzle and the built platform was increased from 0.1 to 0.15 mm to overcome the adherence issue. Then, the experiment was repeated with the same parameters used in the previous trial. This setting reduced the material adherence on the nozzle, as seen in Fig. 4.8b. However, there was fluctuation in the melt flow rate.

Briefly, increasing the melt flow rate to obtain continuity on the 3D printed line structure caused material adherence on the nozzle when the printing gap remained at 0.1 mm. However, when the printing gap was increased to 0.15 mm to prevent melt adherence to the nozzle, the melt flow was still insufficient, as observed

in Fig. 4.8b. As a result, this was a vicious cycle. Also, during the square printing experiments, extrusion temperature fluctuated.



Figure 4.8. a) The square sample printed in ET of 143 °C, PS of 200 mm/min, EM of 1.15, LT of 0.2 mm using a 1.02 mm diameter brass nozzle, b) Square sample printed in EM of 1.15 and printing gap of 0.15 mm

As mentioned before in section 2.6, Anderson (2015) printed non-eutectic alloy using an aluminum nozzle and specified that the aluminum nozzle gave a better response against thermal variation during the printing. Therefore, a new nozzle made from AL7075 was utilized to print simple circular objects like a bracelet. In addition, a mono-block nozzle was designed instead of using a screw barrel and nozzle assembly to facilitate the disassembly of the extruder and prevent any leakage that may occur at the intersection region of the stainless-steel screw barrel and brass nozzle. The nozzle diameter was also decreased from 1 mm to 0.6 mm to reduce the blob formation on the nozzle's periphery during the 3D printing process. Available extruder assembly and mono-block Al nozzle were illustrated in Figs. 4.9a and 4.9b, respectively.

Circles with a diameter of 40 mm were printed using mono-block AL 7075 nozzle. While the EM and ET were set to 1, 143 °C respectively during the experiment, PSs were varied from 300 mm/min to 1300 mm/min with 200 mm/min increments. The printing results are given in Fig. 4.10.

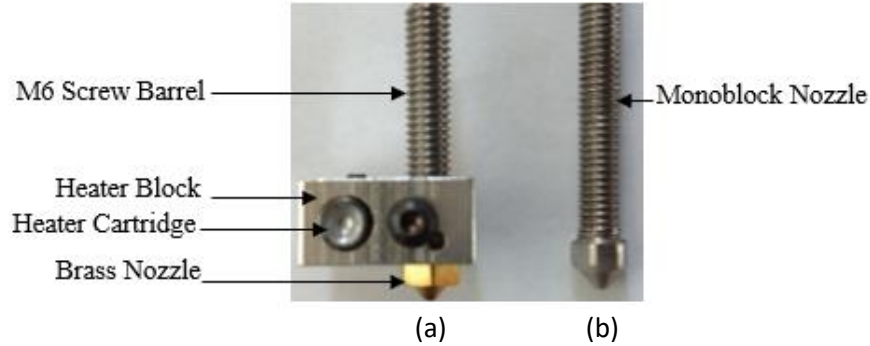


Figure 4.9. a) Standard (unmodified) extruder assembly with Stainless Steel screw barrel with heater cartridge and Brass nozzle, b) Mono-block Aluminum nozzle instead of using screw barrel and nozzle assembly

The printing results shown in Fig. 4.10 indicate that continuity of the printed structure was better for 300 mm/min printing speed. Continuity on the printed circle samples deteriorated due to the increase in PS. However, the results of printing also indicate how far away it is from the desired printing structure. In addition, noise and vibration occurred at the nozzle during the printing process due to insufficient heating, resulting in clogging.

TESTO 881 thermal imager was utilized to examine the AL nozzle's thermal condition. Firstly, the extruders' temperatures were set to 220 °C. Then thermal images were taken from both extruders throughout their heating. The obtained thermal images were given in Fig. 4.11.

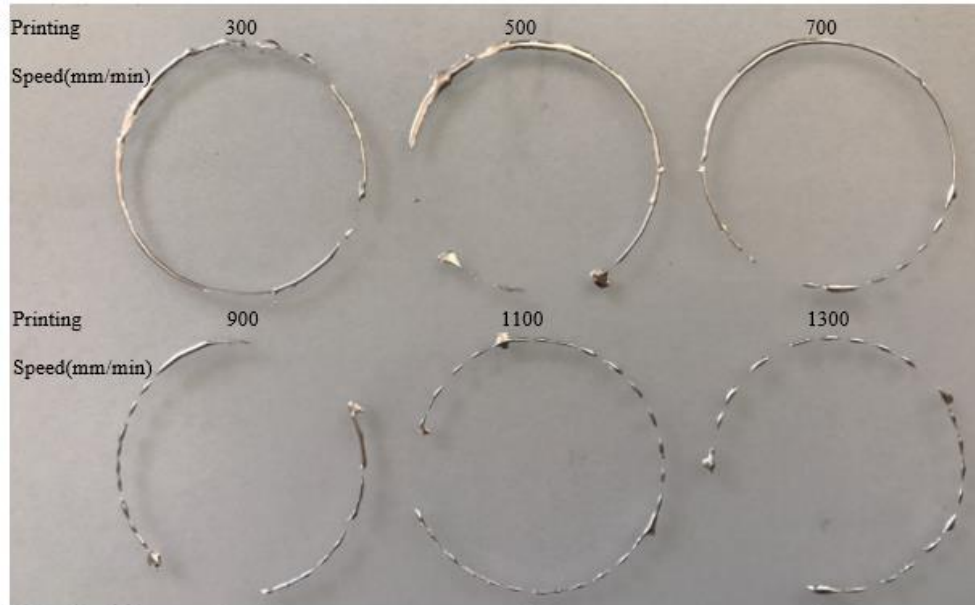


Figure 4.10. Printed circle pattern using the new nozzle made from AL 7075, PSs varied from 300 mm/min to 1300 mm/min

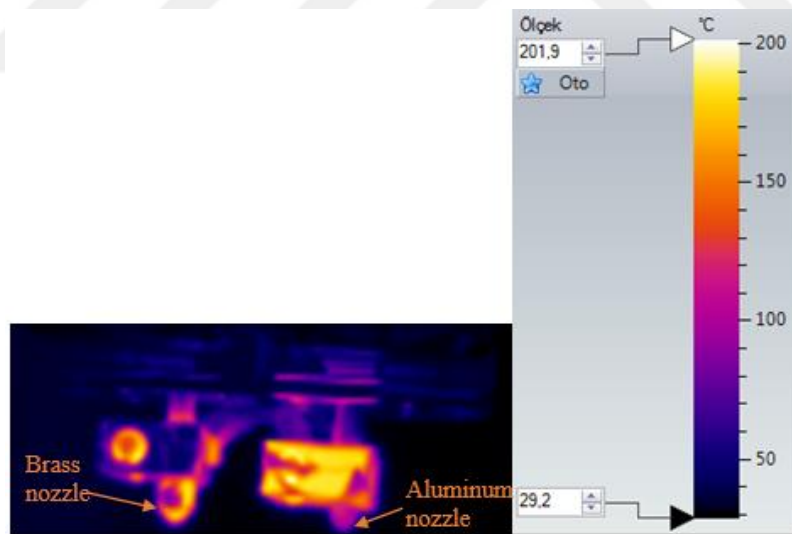


Figure 4.11. Thermal image of brass and aluminum nozzles from left to right, respectively

The thermal images showed that the filament feeding stepper motor was warmer at the right section where the aluminum nozzle mounted in Fig. 4.11.

Although Kapton tape was applied to the right extruder's heater block to decrease heat transfer between the heater block and ambient, the brass nozzle's temperature was higher than the aluminum nozzle, as seen from Fig. 4.11.

Thus, a thermal paste was also squeezed between the heater block and aluminum nozzle to improve heat transfer among the heater block and Al nozzle, as seen from figure 4.12a. Then, ET was set to 150 °C for both extruders.

The application of thermal paste increased heat transfer, and the temperature of the Al nozzle raised approximately to 130 °C, as seen in Fig. 4.12b.

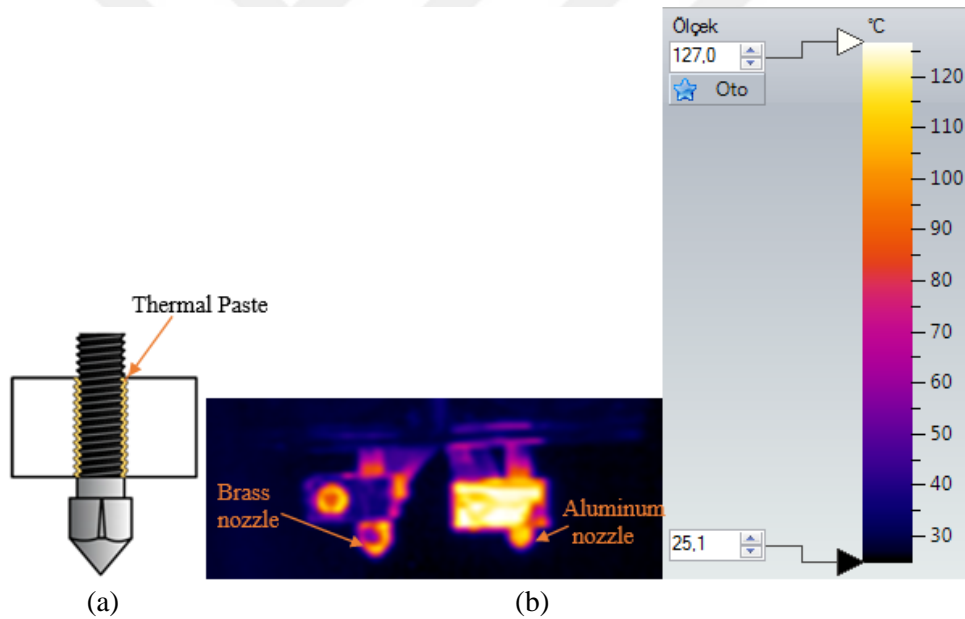


Figure 4.12. a) Thermal paste between the heater block and Aluminum nozzle b) Thermal image of brass and aluminum nozzle from left to right respectively after the thermal paste application of the assembly interfaces

However, the thermal paste applied to the assembly interfaces was found to be not an appropriate remedy. Because when the temperature measurement was

made with a K-type thermocouple on the aluminum nozzle tip, the measured temperature was still lower than the fusible alloy's melting point.

Therefore, the extrusion temperature was set to 200 °C in the machine control panel to achieve a higher temperature than the alloy's melting point on the Al nozzle tip. It was observed that the desired temperature was reached on the Al nozzle tip in the temperature measurement performed with the K-type thermocouple. Yet, the 3D printing process did not commence since the measured temperature by the thermistor was lower than the set temperature.

Also, it was seen from the 3D printer's LCD screen that the extrusion temperature fluctuated rather than reaching a steady-state regime. This situation was not acceptable for the proper printing of the alloy as this can easily change the filament build materials' phase from liquid to solid during the printing process.

In addition, overheating was observed in the extruders' feeding region that has to remain cold during printing process. This may adversely affect the feeding of the wire material during the printing process because heat softens the build material, causing loss of rigidity needed during feeding.

Moreover, when the extruder was disassembled, permanent deformation was detected in the build wire material (filament), which affected both filament movement through the extruder and the melt flow rate. An example of this situation is given in Fig. 4.13.



Figure 4.13. Deformed Bi58Sn42 filament due to the pushing and retraction movements during the printing process

Further, there were local deformations on the filament. As a result, the diameter was not uniform along the length of the wire material. The filament diameter, which is supposed to be 2 mm, was measured as 2.2 mm in some wire

sections. Therefore, this condition also causes fluctuations in melt flow rate and results in non-uniform road size (road-width and layer thickness) lines on the printed sample.

The Bi58Sn42 alloy was attempted to be printed using a commercial desktop type FDM 3D printer which is originally developed for 3D printing of polymer materials. The 3D printing trials were conducted to determine printing-set parameters using two nozzles made of brass and aluminum.

Firstly, line printing trials were carried out to obtain uniform and optimal lines. Afterward, free form and square structures were printed using the best results of the set parameters that were obtained during the line printing experiments.

The initial trials showed that the desired structures were not printed correctly. The reasons for this are as follows:

- The filament materials' diameter used in the printing experiments was not uniform as there was a 20% deviation in filament diameter through its length of 2000 mm while it must have been 2.86 % (Website, 2020d). Also, the built material was deformed during feeding, and as a result, it stuck inside the extruder's cold section, as shown in Fig. 4.13. Therefore, the melt flow rate was also adversely affected.
- Proper heating of the aluminum nozzle was found to be quite unstable due to its high thermal conductivity. The heat was not concentrated at the extruders' hot zone. Instead, the heat was evenly spread on the extruder block. As the extrusion temperature sometimes dropped below the Bi58Sn42 alloys' melting point during the 3D printing process, interruption in the melt flow occurred depending on the phase change of the Bi58Sn42 alloy.
- After determining the suitable print settings from the performed line printing experiments, single layer free form shoe and square shapes

were printed. However, the structural continuity of these shapes was not in acceptable form, as seen from Figs. 4.6, 4.7, and 4.8 due to the unstable melt flow rate during the 3D printing process. Fluctuations in melt flow rate at the nozzle during the printing caused both adherence of the melt material to the tip of the nozzle and non-uniform road size (LT and RW).

It was considered that high deviation on the filament diameter is the primary source of the problems encountered, such as fluctuation in the melt flow rate and extrusion temperature during the performed 3D printing experiments.

Therefore, fusible alloy wire with a tight diametric tolerance supplied from another manufacturer to achieve uniform road size (LT and RW) on printed samples.

Most importantly, the 1.67mm diameter filament was obtained so that the wire doesn't get stuck in the extruder during feeding.

The brass nozzle was preferred instead of the aluminum nozzle as the aluminum nozzle transfers the heat to the extruder's cold region.

Standard brass nozzle (E3D nozzle) was utilized without customization as the Bi58Sn42 filament's diameter is close to 1.75 mm, which is compatible with the current desktop type FDM 3D printer. In addition, nozzle diameter was reduced to 0.4 mm to decrease blob formation that adversely affects the printed parts' quality.

The extrusion temperature was increased to 185 °C to prevent phase change from liquid to solid that caused clogging in the nozzle during the 3D printing process.

While simple line geometry can be printed during the performed 3D printing trials, it was observed that the structures which required continuity could not be printed. Therefore, a maze structure was tried to be printed instead of printing simple lines. Maze structures' layout was given in Fig. 4.14 according to the PS of 150, 300, 450, 600, 750, 900 mm/min and different start points for printing represented by cyan circles.

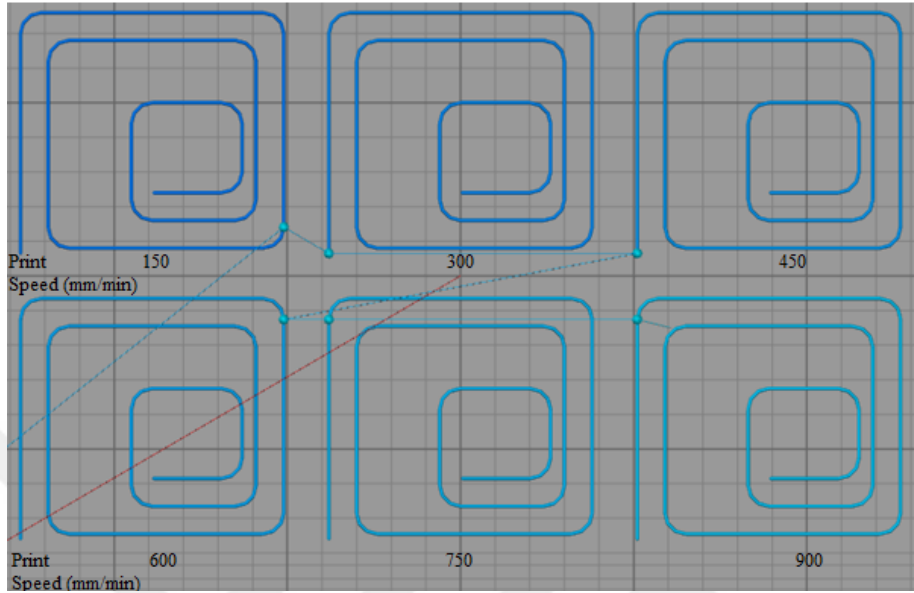


Figure 4.14. The layout of the desired maze structures on the build platform according to the different printing speeds and start point locations

While the maze structure is printed in one step for the printing speeds of 300 and 450 mm/min given in Fig. 4.14, the remaining maze structures were printed in two stages for the printing speeds of 150, 600, 750, and 900 due to their differing start point locations.

For instance, the maze structure that was printed with a printing speed of 600 mm/min, extrusion commenced from fillet at the upper right corner, continued to the direction of counterclockwise, and printed the outside edge of the wireframe. Then extrusion head returned to the start point of the fillet and printed the remaining section clockwise.

For the maze structure printed with 150 mm/min, printing started from the fillet at the right side of the wireframe and continued in the counterclockwise direction, so the wireframes' outer edge was obtained. Later print head turned back to the fillet, and the rest section was printed in the clockwise direction.

The printed maze structures using the ET of 185 °C, platform temperature (PT) of 80 °C, EM of 1, layer thickness (LT) of 0.2 mm, and PS of 150, 300, 450, 600, 750, 900 mm/min were presented in Fig. 4.15.

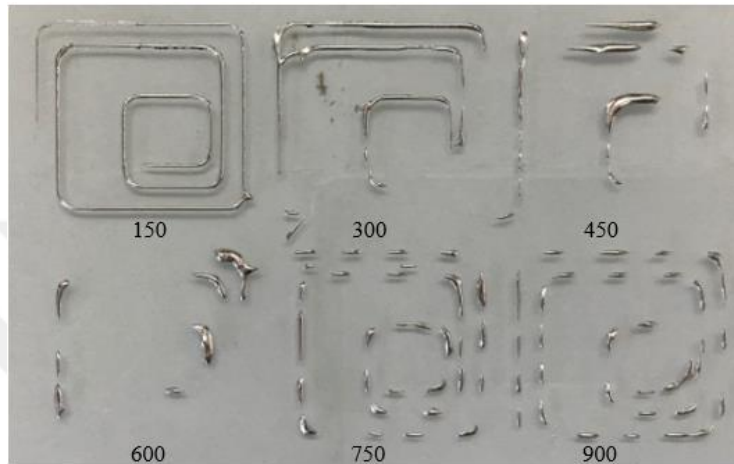


Figure 4.15. Printed maze structures based on 150, 300, 450, 600, 750, and 900 mm/min printing speeds

It was observed that the continuity in the printed maze structure was negatively affected by the increase in the printing speed, as seen from Fig. 4.15.

Increasing printing speed induced a rise in the fusible alloy wires' feeding speed. Therefore, blobs were formed in the printed geometry, as seen in Fig. 4.15. As a result, the maze structure printed with a PS of 150 mm/min was more complete than the others. However, since the maze structure was printed in two steps because of starting point location generated by the slicer for the PS of 150 mm/min, a deterioration was observed at the starting point. While there was a discontinuity in the extruded road during the printing of the mazes' outer edge at the first step, the continuous structure was seen on the printing of the rest section of the maze's at the second step as seen from Fig. 4.16. The reason that causes this situation can be explained by the lack of a feedback mechanism to stabilize the amount of melt in the extruder's hot zone (Ramanath et al., 2008).



Figure 4.16. Close-up of a printed wireframe with a printing speed of 150 mm/min at 185 °C

The maze printing experiment was repeated using the ET of 185 °C, PT of 80 °C, EM of 1, LT of 0.2 mm, and PS of 150 mm/min for all six maze objects as shown in Fig. 4.17. In addition, the effect of the start point on the continuity in the single-layer maze geometry was examined by arranging the start point locations. This helped to print the maze structure without any defect.

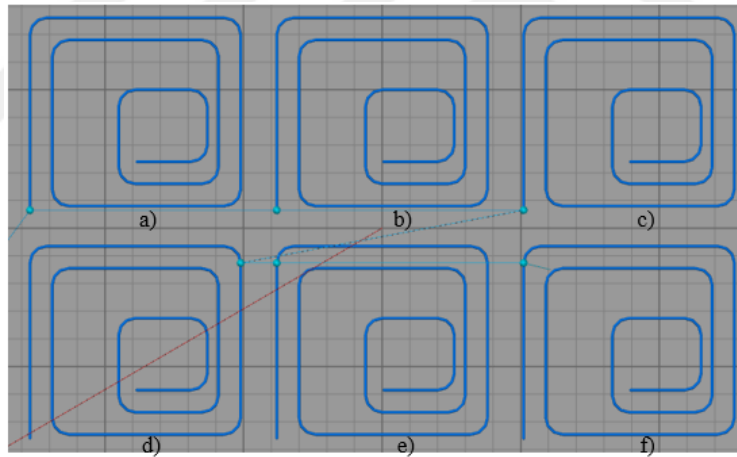


Figure 4.17. The desired layout of the maze structures on the build platform according to the exact and different start point locations

The maze objects printed at the end of the performed experiment were presented in Fig. 4.18. As the printing process was completed in one step for the maze structures at the Figs. 4.18 (a), (b) and (c), continuity in the printed structures of Figs. 4.18 (a) and (b) geometries was better than the object built-in Fig. 4.16.

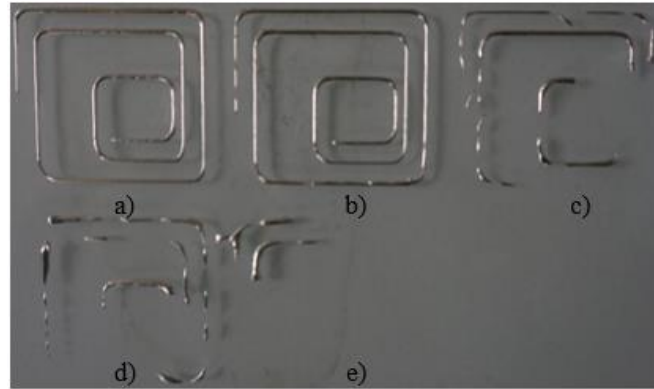


Figure 4.18. Printed maze structures based on the identical and different start point locations at ET of 185 °C

However, interruption in the melt flow was observed during the printing process. Accordingly, the melt accumulated inside the nozzle suddenly flowed into the build platform. As a result, it caused the formation of non-uniform layer thickness and road width on the printed maze geometry, as seen from Fig. 4.18 (d). Furthermore, the experiment was stopped before the 3D printing process was completed since the melt adhered to the nozzles' outer cone.

When the printed maze geometries at the Figs. 4.18 (a), (b) and (c) were compared, there was a difference in the printed shapes' continuity between the first and the third mazes, although they were printed using the same print settings.

It was considered that the problem might be related to leveling as no vibration or noise occurred on the extruder during the 3D printing process due to nozzle clogging. Therefore, the experiment was repeated by the same print settings after leveling the distance between the nozzle and build platform.

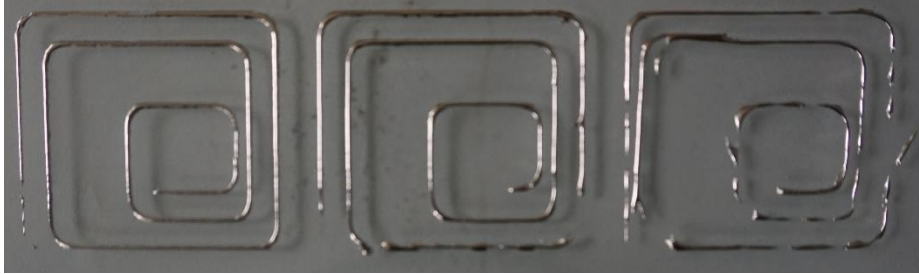


Figure 4.19. Printed maze structures based on the exact starting point locations at ET of 185 °C

A similar outcome like in Fig. 4.18 was also obtained in this performed experiment. Again, while the first printed maze structure was more complete (no interruption in the printed shape), the third one had discontinuity (dashed line), as seen from Fig. 4.19. The source of the problem was the leveling (adjustment of the distance between the nozzle and build platform). The nonoptimal distance between the nozzle and build platform caused the melt to adhere to the nozzle's outer cone. Correspondingly, dashed lines were formed on the third maze shape. Moreover, when the extruder passed over the printed maze shape a second time to improve adhesion between the object and the build platform, the nozzle was hitting and deteriorating the printed maze structure as the deposited layer thickness was higher than the distance between the nozzle and the build platform.

4.2.1.1. Multi-layered shell printing trials performed using the standard (unmodified) extruder

After all, it was inferred that a single layer continuous structure without any dashed line could be printed with a calibrated leveling between the nozzle and build platform at low printing speed.

An object can be 3D printed on start-stop or vase mode in Simplify3D. While extrusion is not interrupted during the vase mode, extrusion is interrupted in start-stop printing mode. Therefore, printing trials were carried on vase mode to print multilayer objects without dashed lines.

A ring with a diameter of 20 mm was tried to be printed in vase mode onto the adhesive (Pritt) applied glass build platform using EM of 1, PS of 100 mm/min, LT of 0.2, PT of 75°C, ET of 150 °C and using 0.4 mm brass nozzle. Although the first layer of the ring was partially slipped, as seen from Fig. 4.20b, the ring could be printed. But, when the height of the ring was increased, the printing quality was negatively affected due to the slippage of the ring, as seen from Fig. 4.20a.



Figure 4.20. Ring samples printed in vase mode

The fusible alloy was coated onto the copper clad board to print the upper layer successfully and improve adhesion between the part and the build platform. Then, an attempt was made to print a hollow cylinder with a diameter of 12.5 mm and a height of 25 mm onto the fusible alloy coated copper clad board.

Extrusion temperature (ET) was increased to 160 °C as the copper clad board temperature was lower than the glass platform temperature. The hollow cylinder's print quality was satisfactory, as seen from Fig. 4.21.

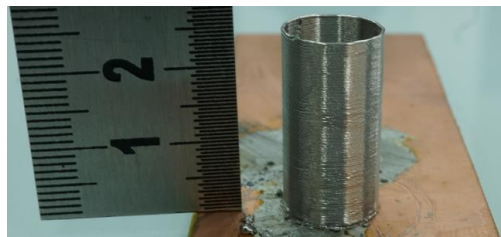


Figure 4.21. The hollow cylinder printed in vase mode

After the hollow cylinder geometry trials, more complex geometry was printed in the same print settings as the previous one. Only ET was increased to 180 °C for better bonding between the first layer of the part and the copper clad board. But the separation was seen at the printed part' middle section as seen from Fig. 4.22 since the leveling was not calibrated correctly. However, the printed part did not slip during the printing seventy-eighth layers.

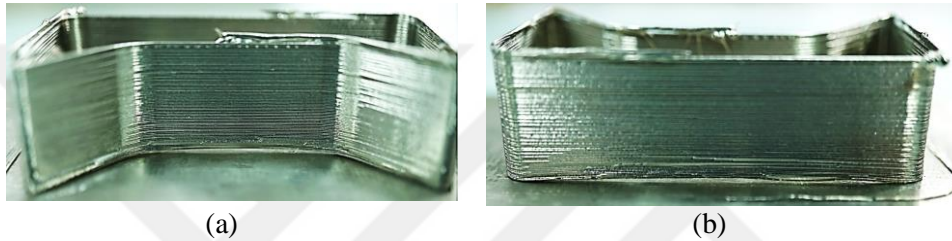


Figure 4.22. Separation of the printed part's first layer from the middle section of the copper-clad board due to the improper leveling during printing of a open shell box with 78 layers at ET of 180 °C ; a) front view and b) back view

Therefore, the distance between the copper clad board and the nozzle was appropriately leveled, then the experiment was repeated with the same printing settings. Also, hair spray was coated onto the board to improve bonding between the part' first layer and the copper clad board and consequently, the separation did not occur between the board and the printed part's first layer during the performed printing trial. However, layer separation was observed at the object's left edge during the printing process, as seen from Fig. 4.23.

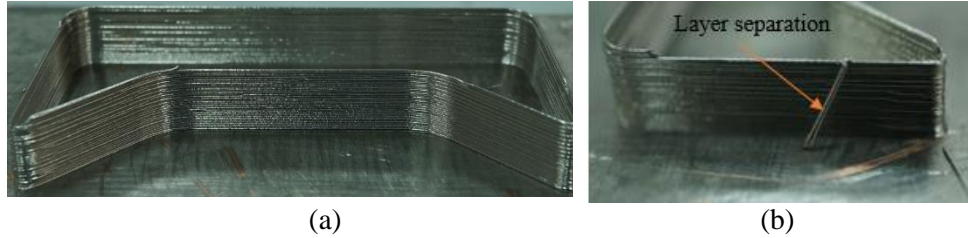


Figure 4.23. Layer separation on the printed structure; a) front view and b) side view

The reasons for the layer separation problem were outlined as too large layer height and low print temperature according to the Simplify3D troubleshooting guide (Website, 2021j) since both reasons induced poor bonding between each successive layer.

Neither the too large layer height nor the low print temperature were not the source of trouble experienced. There was no such separation on the printed ring samples using the 0.2 mm LT in Figs. 4.20 and 4.21. Also, as the set ET melted both the newly deposited and previously solidified layers during printing, it was inferred that the set ET was too high. Hence, the extrusion temperature was decreased to 160 °C, and the experiment was repeated. Printed male and female shell structures were given in Figs. 4.24 and 4.25, respectively.

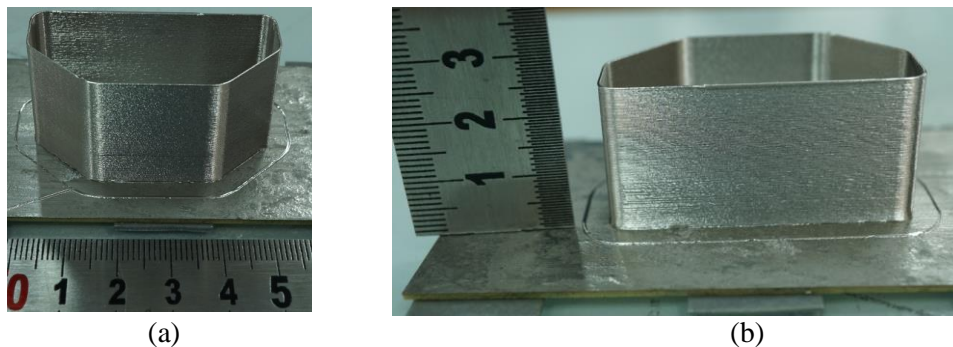


Figure 4.24. The printed male shell consists of 125 layers; a) front view and b) back view

It was seen that both road width and layer thickness was compatible with the values set in the Simplify3D when the measurements were performed on the printed samples in Figs. 4.24 and 4.25. Surface quality was satisfactory. There were no dashed or missing layer lines on the printed geometries during 3.5 hours of the printing process for the every printed shells.

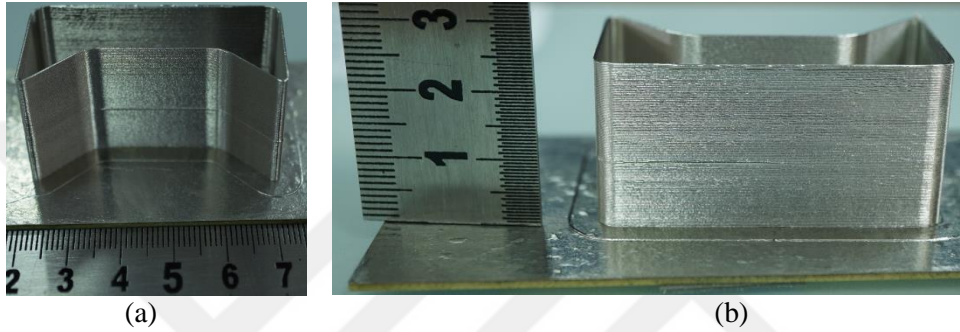


Figure 4.25. The printed female shell consists of 125 layers; a) front view and b) back view

In the next experiment, a shell structure with the curvilinear surface was printed using the same print settings employed on samples presented in Figs. 4.24 and 4.25. But the printing trials were adversely affected since the rough contour map of the copper-clad board surface-induced planar defect on the printing area. Hence, it was decided to use the glass build platform again. Instead of pritt, a hair spray was applied to the glass build platform to prevent part slippage during the printing process. However, the shell structure with a curvilinear surface could not be printed entirely in the performed experiments. Moreover, print failed in different percentages of the printing process during the repetitive experiments implemented in the same print settings (ET, LT, etc.), as seen from Fig. 4.26.

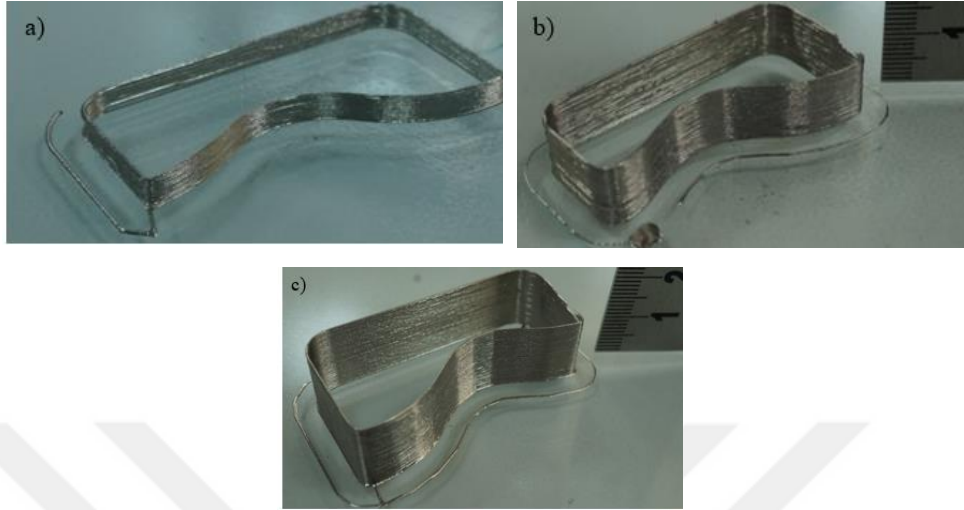


Figure 4.26. Images of the printed curvilinear shell specimens; a) Failed print at the initial stage of the process, b) Failed print at 47% of the print process, and c) Failed print at 70% of the print process

Moreover, fluctuation in road size (LT and RW) was observed on the printed samples in Fig. 4.26 due to the acceleration-deceleration on curvilinear surfaces, as observed in Fig. 2.5. For this reason, the printed curvilinear surfaces were rougher than the prismatic specimens in Figs. 4.24 and 4.25.

4.2.1.2. Infill printing trials performed using the standard (unmodified) extruder

As the aim of the study requires solid (100% infill) object printing of dies for sheet metal forming, infill printing trials were initiated in vase mode. In this context, an attempt was made to print a square object with dimensions 25x25 mm according to the extrusion temperature (ET) settings 160 °C, extrusion multiplier (EM) of 1, layer thickness (LT) of 0.2 mm, road width (RW) of 0.4 mm and printing speed (PS) of 100 mm/min.

Once again, fluctuation in extruded road's size (RW, LT) was observed in infill printing trials similar to printed layers of the curvilinear shell specimens. Dash

lines were also detected on printed infill samples. The printed infill samples can be seen from Fig. 4.27.

While the prismatic shell samples like in Figs 4.24 and 4.25 can be printed successfully using the same print settings. The structures involved in curved sections failed due to the acceleration-deceleration at turning points to print rounds within the part geometry seen from Figs. 4.26 and 4.27.

Furthermore, the quality of printed samples was not uniform in the repeated printing trials with the same print settings that were used during the infill printing experiments as seen from Fig. 4.27. Thus, the printer hardware's reliability and repeatability were poor and not acceptable. The main reason for this was the fluctuation in the melt's mass flow rate at the nozzle outlet during the printing. This was due to the inability to control the pressure in the extruder's hot zone (Ramanath et al., 2008).



Figure 4.27. Infill samples printed using EM of 1, PS of 100 mm/min, LT of 0.2, PT of 75°C, ET of 160 °C

Continuous Jetting (CJ) and Drop on Demand (DOD) systems were employed to control the pressure in the extruder. However, these systems also had

poor dimensional (LT, RW) control over the extruded road, as previously provided in Tables 2.5 and 2.6 for the commercial printer used in this work.

The printed parts' quality using a typical FDM printhead was better than those printed via CJ and DOD systems, as seen from Figs. 4.24 and 4.25.

Agarwala et al. (1996b) specified that viscosity is one of the critical variables for a successful FDM process. Gibson et al. (2018) determined that the ideal viscosity range must be between 40 and 40.10⁶ Pa.s for the filament material. On the other hand viscosity of the Bi58Sn42 alloy is relatively low. It is under 0.1 Pa.s, as seen from Fig. 3.2. It was also observed that the first printed object was more complete than the second and the remaining objects when printing multiple objects in a single process as given in Figs. 4.15, 4.18, and 4.19. Therefore, it was inferred that the extruder's hot region must be enlarged.

As described in section 3.2, a coil heater was mounted to the print head to have uniform temperature distribution and enormous melted volume of the bismuth alloy through the nozzle. In addition, a proportional, integral, and derivative (PID) type of controller was interfaced and adapted to the system to control the extrusion temperature sensitively. Finally, the K-type thermocouple was attached to the stainless-steel nozzle with a diameter of 0.66 mm to monitor the nozzle's temperature during the printing process. The customized extruder was presented in Fig. 3.3.

4.2.2. Printing trials performed using the customized extruder

In previous printing trials, initially, a smooth line was printed by regulation of print settings. Then the optimum print settings obtained in the performed line printing experiments were used for printing more complex shapes. Yet, it was observed that the complex structures which required continuity could not be printed while the simple line printing trials were reasonable successful. For this reason, instead of printing simple lines, a more continuous shape was tried to be printed as seen from Fig. 4.28.

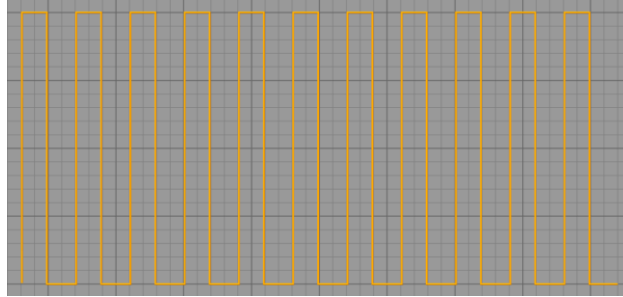


Figure 4.28. A maze shape to be printed to evaluate the continuity in the printed sample

As the alloy's melting point is 140 °C and the heated zone is larger than the standard extruder in the available FDM hardware, the extrusion temperature was set to 140 °C. The remaining parameters RW, EM, LT, PS, and PT were set as 0.66 mm, 1, 0.2 mm, 250 mm/min, and 75 °C, respectively, to print the pattern given in Fig. 4.28.



Figure 4.29. Printed maze geometry at an extrusion temperature of 140 °C

Melt flow was insufficient, as seen from Fig. 4.29. As a result, the printed line's widths were smaller than the 0.66 mm. In addition, blobs, dash lines, and unprinted sections were observed on printed maze geometry. In addition, as the printed line's road width is tiny and the adhesion between the printed line and platform is insufficient, the printed first layer separated from the build platform

during the printing of the second layer. Therefore, extrusion temperature (ET) increased to 150 °C, print speed (PS) decreased to 100 mm/min, and extrusion multiplier (EM) was set as 2 to achieve uninterrupted flow for the next printing experiment.

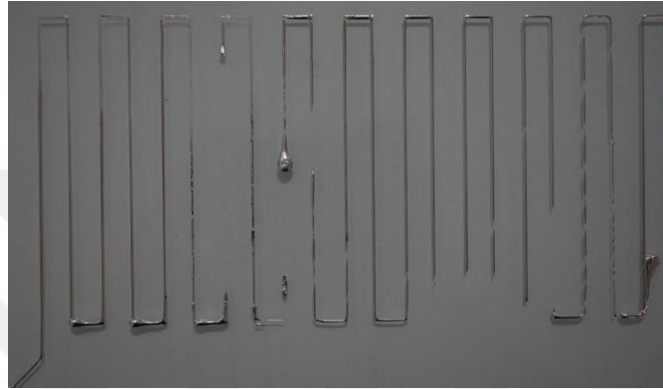


Figure 4.30. Printed maze geometry at an extrusion temperature of 150 °C

The printed maze pattern was more complete since both EM and ET were increased, as seen from Fig. 4.30. However, the extruded road's size was not uniform due to acceleration-deceleration on the maze structure's sharp turning points (Turner and Gold, 2015).

The layer thickness was getting smaller in some partitions of the build maze geometry and even zero. This source of the problem was related to the manual leveling between the platform and nozzle. Thus, the size of the maze geometry was decreased to obtain a more uniform focused distance between the nozzle and the built platform. Also, ET was set to 160 °C while the other print parameters remained constant. The layout of the new geometry and printed maze were given in Figs. 4.31 and 4.32, respectively.



Figure 4.31. The layout of the maze shape to be printed

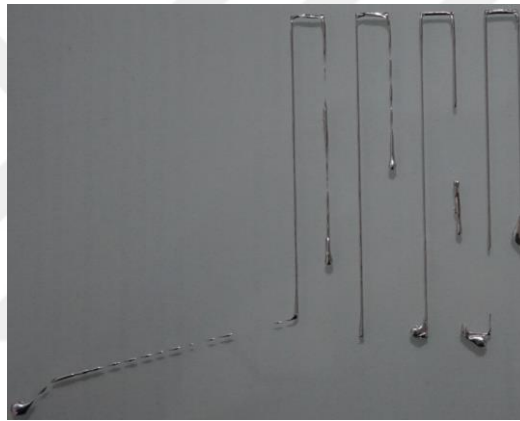


Figure 4.32. Printed specimen for EM:2, PS: 100 mm/min, Temp:160 °C, LT:0,2 and table temp: 75 °C

It was expected that complete geometry could be printed as the set ET value was higher than the previous one. However, interruptions and blobs were seen on printed geometry in Fig. 4.32. The resulting structure was unacceptable. Ooze (leakage) was seen before the extruder started printing. Therefore, ET was decreased to 150 °C to prevent ooze, and the extrusion multiplier (EM) was increased to 4 for the subsequent printing trial. Melt flow was less due to the previous experiment during the performed printing trial. Increased feed quantity and set ET were not compatible with each other. Hence in the same experiment conditions (for printing speed: 100, extrusion multiplier: 4, layer thickness: 0,2, table temp: 75 °C), only

extrusion temperature was increased to 170 °C, and the experiment was repeated. The top and side views of the printed maze sample were presented in Fig. 4.33.

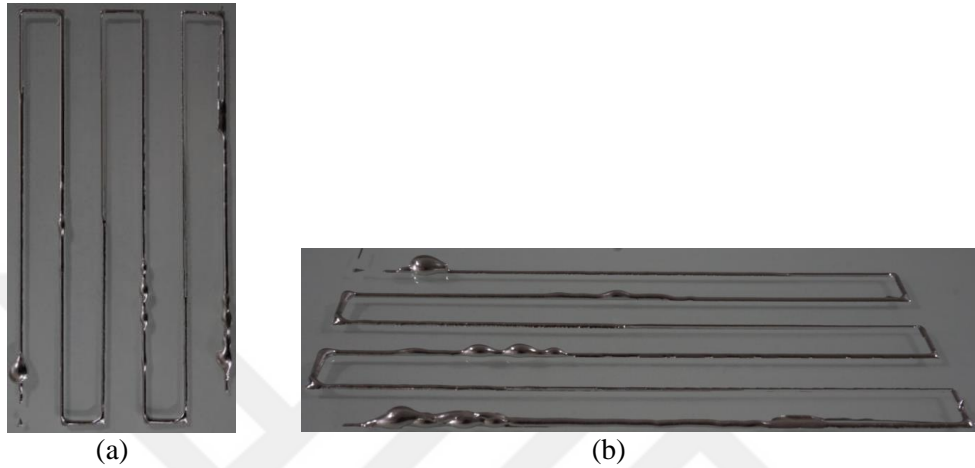


Figure 4.33. Image of the sample printed at printing speed: 100 mm/min, extrusion multiplier: 4, layer thickness: 0,2 mm, table temp: 75 °C and extrusion temperature 170 °C a) top view and b) side view

There was fluctuation on deposited road size, as seen from Fig. 4.33. The main reason was explained by Ramanath et al. (2008) as the absence of a pressure drop feedback mechanism on the extruder. The increase in extrusion multiplier (EM) also affected this fluctuation. Especially, deflection in layer thickness was greater than the other performed printing experiments. Therefore, the extrusion multiplier decreased to 1 to prevent non-uniform layer thickness on the printed extruded road. The extrusion temperature was set to 200 °C to obtain continuous melt flow. Thus, it was expected that the desired maze geometry could be printed.

The extrusion temperature fluctuated between 191 °C and 195 °C during the printing process. The printed sample in Fig 4.34 was more complete according to the models in Figs. 4.29, 4.30, 4.32, and 4.33. Interruption in the continuity of the printed geometry was observed in a small region at the upper corner sections.



Figure 4.34. Sample printed at printing speed: 100 mm/min, extrusion multiplier: 1, layer thickness: 0,2 mm, table temp: 75 °C and extrusion temperature 200 °C

The maze printing experiment was repeated by increasing only the extrusion multiplier from 1 to 4 to obtain a more continuous (uninterrupted) line structure. In addition, the temperature was decreased to 192 °C during the printing process. As a result, non-uniform layer thickness and road width were obtained as seen at some sections of the printed geometry in Fig. 4.35, due to an increase in the extrusion multiplier.

4.2.2.1. Infill printing trials performed using the customized extruder

It was seen that continuous geometric shapes could be printed by optimizing extrusion temperature, printing speed, and the extrusion multiplier. Therefore, experiments were extended to print a solid single-layer sample.

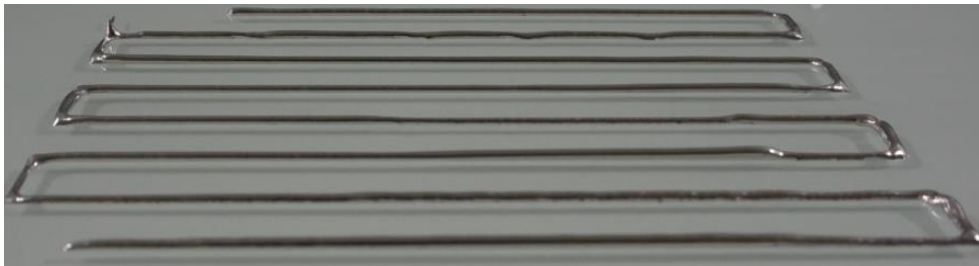
In this context, it was aimed to print a single-layer solid (%100 infill rate) square sample using the ET of 200 °C, platform temperature (PT) of 75 °C, EM of 4, layer thickness (LT) of 0.2 mm, and PS of 100 mm/min. However, the deposited (solidified) road's width was larger than the set road width in Simplify3D due to the spreading of extruded road at an extrusion multiplier of 4. Correspondingly, the spreading of extruded road filled the next adjacent partition before the extruder

commenced printing in that section. Thus, when the extruder began printing in that partition, the printing process was adversely affected, and the printed structure was degraded.

Therefore, the infill rate (IR) was reduced to %50 while the other parameters were kept constant then the experiment was repeated. Finally, a printed square sample was printed and given in Fig. 4.36.



(a)



(b)

Figure 4.35. Sample printed at printing speed: 100 mm/min, extrusion multiplier: 4, layer thickness: 0,2 mm, platform temp: 75 °C and extrusion temperature 200 °C; a) top view and b) side view



Figure 4.36. Square sample printed at printing speed of 100 mm/min, extrusion multiplier of 4, the layer thickness of 0,2 mm, platform temp of 75 °C, extrusion temperature 200 °C, and %50 infill

The high extrusion multiplier (EM) value and the infill and outline coalescence adversely affected the printed sample's dimensional accuracy and surface roughness. Deposited (solidified) road couldn't maintain its shape when the extruder prints near the deposited road. The same problem was mentioned by Mireles et al. (2013). Therefore, EM decreased to 1 for the next solid square sample printing experiment. In addition, the infill rate was raised to %75 as the EM was reduced. Also, the square's edge length was lowered to 20 mm to shorten the experiment duration. Simplify3D image of the part to be printed and printed sample were given in Fig. 4.37, respectively.

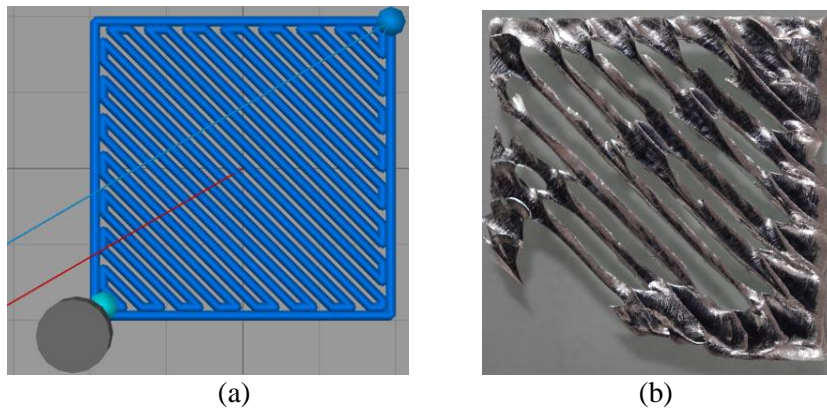


Figure 4.37. a) The process simulation image of the part to be printed and b) Square sample printed at printing speed of 100 mm/min, extrusion multiplier of 1, the layer thickness of 0,2 mm, platform temp of 75 °C, extrusion temperature 200 °C, and %75 infill

A solid square sample could not be obtained for EM of 1 and IR of 75 % in the performed printing experiment. Hence, the test was repeated with an infill rate of 100% to print the solid square sample. Process simulation image and the printed square model were presented in Fig. 4.38, respectively.

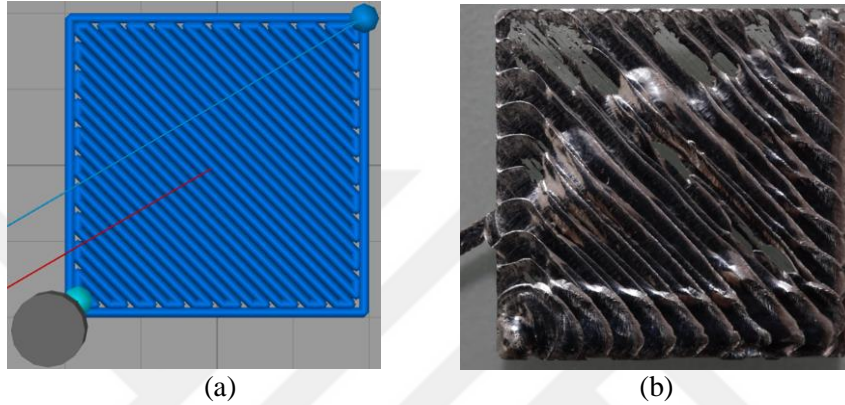


Figure 4.38. a) Simplify3D image of the object and b) the obtained result for the solid square sample using extrusion temperature 200 °C and table temperature 75 °C with a printing speed of 100 mm/min, extrusion multiplier 1 and % 100 infill rate, respectively

As seen from the process simulation image in Fig 4.38 (a), the extruder moved to the right upper corner of the square sample to begin the printing process. During this movement of the tool head, melt flowed freely (leakage or ooze) from the nozzle onto the built platform before the feeding stepper started to push filament material into the nozzle. When the extruder moved to the region where the ooze occurred and started printing the square sample's internal area, solidified ooze caused the tool head to move up and down. Accordingly, both the printed sample's flatness and printing process were adversely affected.

Therefore, the printing process's starting point was altered to the left bottom corner of the square sample to prevent any solidified leakage in the region where the part would be printed. Then printing experiment was repeated with the same parameters (ET of 200 °C, PS of 100 mm/min, EM of 1, and IR of %100).

The printed part's flatness in Fig. 4.39 was better than the sample in Fig. 4.38 since the leakage was not formed in the region where the part would be printed. However, although the print settings were the same for the printed two samples, the finish part quality on repeated attempts at the same print settings was not uniform, as seen from Figs 4.38 and 4.39. This was mainly due to the absence of a feedback mechanism controlling the amount of melt in the hot zone of the extruder in FDM systems. This also stated by Ramanath et al. (2008).



Figure 4.39. Obtained results for the solid square sample using extrusion temperature of 200 °C and table temperature of 75 °C with a printing speed of 100 mm/min, extrusion multiplier 1, and % 100 infill rate, respectively

Therefore, it was planned to increase the number of cycles for extruder (tool head) motions in the internal region (infill) of the object so that a solid structure could be printed due to overlap during the printing. Thus, road width (RW) was decreased from 0.66 mm to 0.5 mm in this context, while the remaining print settings were not changed. Rising in the number of fibers within the square sample's internal region can be seen from the process simulation image in Fig. 4.40.

Non-uniform road size (LT and RW) was obtained due to fluctuations in the melt's mass flow rate. This was mainly related to the absence of a pressure drop feedback mechanism in the extruder. In some regions, deposited LT was higher than the distance between the nozzle and build platform. When the extruder (tool head)

deposited near this region, the extruder moved up and down (reciprocating motion). Therefore, there were unprinted sections on the printed geometry, as seen from Fig. 4.40.

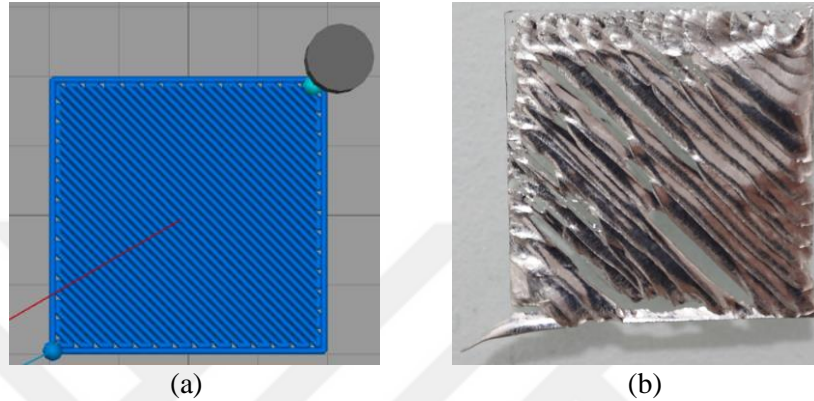


Figure 4.40. a) The process simulation image of the part to be printed and b) The solid square sample was 3D printed using an extrusion temperature of 200 °C, table temperature of 75 °C, printing speed of 100 mm/min, extrusion multiplier of 1, extrusion width of 0.5 mm, and % 100 infill rate

Experiments were continued by reducing RW to print solid (IR of 100%) square sample. Firstly, RW was adjusted as 0.2 mm so that extruder's reciprocating motion would be prevented and a solid object could be printed. But the Simplify3D gave a warning message that there might be poor strength. So, RW was set to 0.3 mm.

Infill printing was successful at the beginning of the printing process, but then infill printing failed since the adjusted RW of 0.3 mm was too small for a nozzle whose diameter equals to 0.66 mm. Deposited RW was larger than 0.3 mm. When the tool head moved with the small step of 0.3 mm to print the internal region of the object, there was solidified material in the print region. This induced extruder to move up and down during the process. Again, unprinted sections occurred on the

printed sample due to the no contact between the nozzle and build platform during the tool head's reciprocating motion, as seen from Fig. 4.41.

Therefore, the extrusion temperature was set to 180 °C to reduce the extruded road's spreading and minimize the tool head's reciprocating motion accordingly. Then the experiment was repeated. But, reciprocating motion on the nozzle was seen like in previous attempts during the performed experiment. Therefore, printing was adversely affected, as seen from Fig. 4.42.

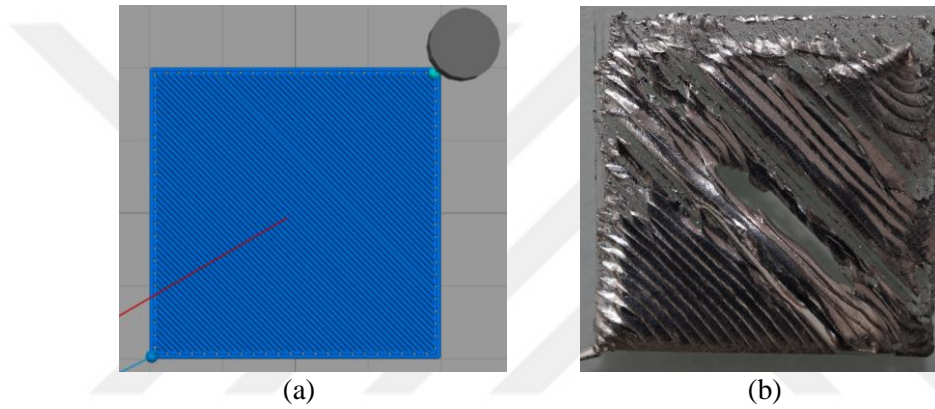


Figure 4.41. a) The process simulation image of the part to be printed and b) The solid square sample was 3D printed at an extrusion temperature of 200 °C, platform temperature of 75 °C, printing speed of 100 mm/min, extrusion multiplier of 1, extrusion width of 0.3 mm, and 100 % infill rate.



Figure 4.42. The solid square sample was 3D printed at an extrusion temperature of 180 °C, platform temperature of 75 °C, the printing speed of 100 mm/min, extrusion multiplier of 1, extrusion width of 0.3 mm, and 100% infill

Following findings were achieved during the performed single layer solid square printing attempts:

- The fluctuation in extruded road's size (LT and RW) increased further due to the rising of EM, as seen from Fig. 4.35.
- Deposited road couldn't maintain its shape, especially in the part geometry's sharp turning locations as seen in Figs 4.35 - 4.42. When the newly deposited road contacted with the deposited one (solidified road), solidified road fused with the newly deposited road as the printed alloy was eutectic in contrast to semi-solid polymers. Correspondingly, there was a fluctuation in road size (LT and RW) at the coalescence region. This might cause the failure of the multilayer object printing process since the problem in one layer affected the printing of successive layers cumulatively.
- There was leakage from the nozzle in some printing experiments before the feeding stepper pushed the filament into the nozzle. This situation adversely affected the printing process, as seen from Fig. 4.38. Although the experiment was repeated with the same print settings after

the leakage was prevented, the printed sample's quality was worse, as seen from Fig. 4.39. Hence, the process repeatability was poor due to the absence of a feedback mechanism controlling the amount of melt in the hot zone of the extruder in FDM systems.

- When the desired result was not achieved in the performed printing trials, the number of extruder movements in the object's internal region had been increased by decreasing RW setting to print a solid (IR of %100) object. But, this alternative approach didn't give the desired result because the extruded road's spreading made the extruder move up and down (reciprocating motion) during the printing process.

Therefore, it was planned to decrease the extruder's number of sharp turning movements by selecting an alternative infill pattern to minimize the acceleration-deceleration and coalescence of the deposited road with the newly deposited one at sharp turning points.

In this context, the concentric infill pattern was considered instead of the rectilinear pattern. Moreover, print geometry was altered from square to circular geometry since there is no sharp turning movement on the circular geometry in contrast to square geometry.

Then the process simulation was generated to build a single-layer solid circular object with a diameter of 30 mm for both concentric and rectilinear infill patterns, as seen from Fig. 4.43. It can be seen in Fig. 4.43 that the number of sharp turning points in the concentric infill is less than the rectilinear infill.

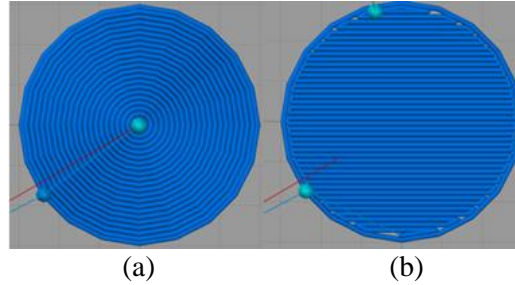


Figure 4.43. Image of the infill patterns: a) concentric infill, b) rectilinear infill

The single-layer solid circular sample (% 100 infill rate) printing experiment was initiated using the ET of 170 °C, platform temperature (PT) of 75 °C, layer thickness (LT) of 0.2 mm, PS of 100 mm/min, EM of 1 for both concentric and rectilinear infill patterns. Unfortunately, there was too much unprinted area on the printed geometries for the EM of 1. Therefore, the experiment was repeated by increasing EM to 2. The 3D Printed circular samples using concentric and rectilinear infill patterns were given respectively in Fig. 4.44.

According to the rectilinear infilled circle, the circle with the concentric infill was more complete, as seen in Fig. 4.44. The measurements made with ImageJ software determined the infill rates (IR) as 97.451 % and 88.383 % for samples printed with concentric and rectilinear infill patterns, respectively.

Maximum road (extrusion) width was measured as 2.6 mm for sample printed with rectilinear infill pattern. The measured value was 3.94 times the set road width value in Simplify3D due to the EM of 2 and coalescence of infill and outline.

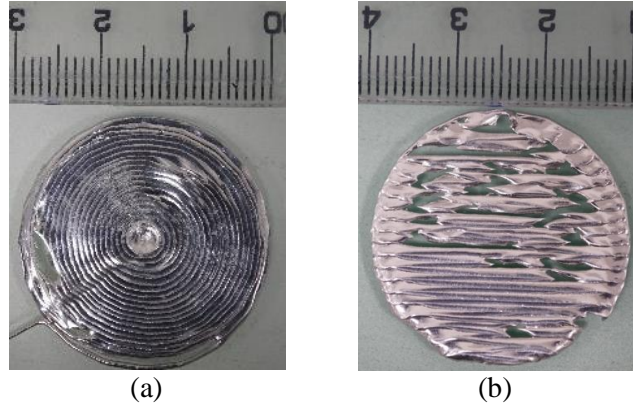


Figure 4.44. Images of the 3D printed single-layer solid circle with a) concentric and b) rectilinear infill patterns, respectively

On the other hand, maximum road width was measured as 4 mm in the innermost circle for the sample printed with the concentric infill pattern. However, the measured road width deviation was lower according to the model printed with the rectilinear infill pattern as the road width was 2.28 mm for the innermost circle in the generated simulation file, as seen from Fig. 4.43a. Furthermore, the maximum road width was 2.08 mm in measurements made in other regions except for the innermost circle. This value is 20 % less than the sample printed with a rectilinear infill pattern because there were no sharp turning movements and coalescence between the infill and outline.

Layer thickness (LT) was varied between 0.2 and 0.9 mm for the samples printed with rectilinear and concentric infill patterns. Therefore, the measured maximum layer thickness value was 4.5 times the set LT value in Simplify3D. The main reasons were related to the alloy's shear-thinning feature (Lee et al., 2008a) and the absence of any pressure drop feedback system (Ramanath et al., 2008). As seen from Fig. 4.44, this increase in layer thickness caused the printhead to move up and down. Correspondingly, porosities (unprinted regions) were formed on printed samples.

During the single-layer solid sample printing experiments, the highest infill rate was obtained in the circle printed with the concentric infill pattern. Accordingly, the printing trials were continued for multi-layered solid hemisphere production. Thus, it was planned to use the printed solid hemisphere as a male mold for the sheet metal forming process.

As the mold's surface quality is crucial, the hemisphere was first tried to be printed in continuous printing (vase) mode. Later, it was aimed to print the multilayer solid hemisphere in start-stop mode. In this context, process files were generated in Simplify3D to print the hemisphere for both in vase mode and start-stop mode. Simplify3d images of the hemispheres for both vase mode (0% infill rate) and start-stop mode were illustrated in Fig. 4.45a and 4.45b, respectively.

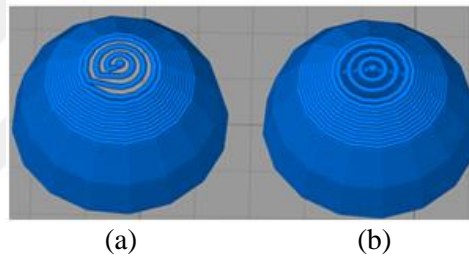


Figure 4.45. Simplify3d images of the hemisphere for a) vase mode and b) start-stop mode.

An attempt was made to print the hemisphere with a diameter of 20 mm in vase mode onto the adhesive (Pritt) applied glass build platform using PS of 100 mm/min, LT of 0.2 mm, PT of 75°C, ET of 170 °C, and 0.66 mm stainless steel nozzle. EM was decreased to 1 since the EM of 2 caused non-uniform layer thickness in printing a single-layer solid circle sample. The printed specimen was presented in Fig. 4.46. Unprinted region occurred on the printed hemisphere shell's top surface due to the lack of contact between the melt flowing from the nozzle and the printed sample. Nevertheless, it was predicted that the hemisphere could be printed with these print settings.

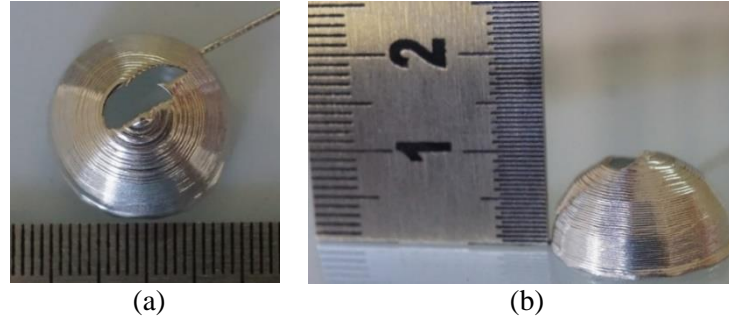


Figure 4.46. Hemisphere sample with a diameter of 20 mm printed in vase mode using PS of 100 mm/min, LT of 0.2 mm, PT of 75°C, ET of 170 °C, and EM of 1; a) top view and b) side view

As the printing of a 20 mm solid hemisphere prolongs the duration of the experiment, the sphere diameter was decreased to 10 mm, and the solid hemisphere was printed using the print settings in the previous experiment. The excessive increase in the layer thickness within the infill region caused the extruder to move up and down. Accordingly, the sphere's contours could not be printed. Therefore, the process was canceled at 51 percent. While the height of the finished sphere should be 5 mm, the sphere height was 3.23 mm when the process was still at 51 percent. The printed sample was presented in Fig. 4.47.

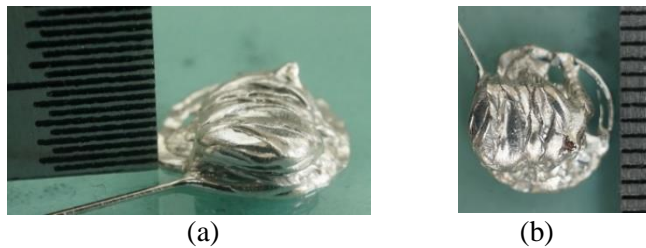


Figure 4.47. Solid hemisphere sample with a diameter of 10 mm printed in start-stop mode using PS of 100 mm/min, LT of 0.2 mm, PT of 75°C, ET of 170 °C, IR of 100 %, and EM of 1; a) isometric view and b) top view

The infill rate (IR) was reduced to 50 percent to prevent an excessive increase in layer thickness within the infill area. Then the experiment was performed. In this experiment, as in the previous one, the layer thickness adversely affected the

printing process. Therefore, the printing speed was increased from 100 mm/min to 500 mm/min to reduce the rise in layer thickness further, and the experiment was repeated with the other print settings remaining the same. As seen from Fig. 4.48, the printed hemisphere was more successful than other trials. However, the printed sample was not a exactly sphere since the deposited (solidified) road could not keep its shape when the extruder deposits adjacent section to the deposited terminal.



Figure 4.48. Solid hemisphere sample with a diameter of 10 mm printed in start-stop mode using PS of 500 mm/min, LT of 0.2 mm, PT of 75°C, ET of 170 °C, IR of 50%, and EM of 1; a) isometric view and b) side view

Finally, a hemisphere with a diameter of 20 mm was printed using the same print settings used to print a sample in Fig. 4.48. The fluctuation in layer thickness caused the nozzle to move up and down during the printing process. Therefore, porosity occurred in the printed sample. The printed hemisphere sample was given in Fig. 4.49.

While the deposited (solidified) road melted and fused with the newly deposited road during the printing of the sample in Fig. 4.48, the same situation was not observed for the printing of the model in Fig. 4.49. As a result, it was inferred that there was not enough cooling time for sample printing in Fig 4.48. However, both samples did not retain their shape during the printing as the printed alloy was eutectic. Accordingly, the printed geometry was adversely affected.

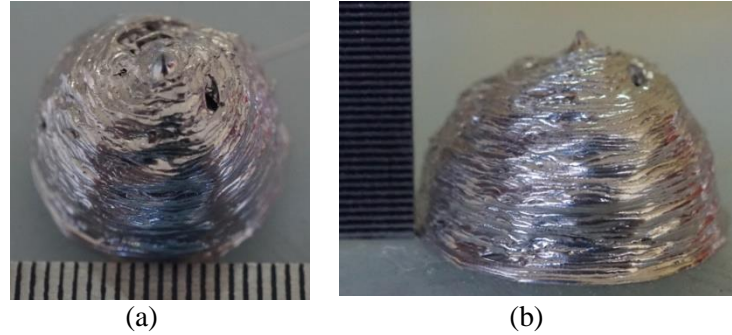


Figure 4.49. Solid hemisphere sample with a diameter of 20 mm printed in start-stop mode using PS of 500 mm/min, LT of 0.2 mm, PT of 75°C, ET of 170 °C, IR of 50%, and EM of 1; a) isometric view and b) side view

4.3. The effect of print settings on 3D printed sample geometry

The effect of print settings on the printed sample geometry was given in Table 4.1.

Table 4.1. Print settings and their effects on the printed sample geometry

ET	The melt flow was insufficient for the ET of 140 °C. Therefore, dash lines were formed on the printed sample. While the simple line could be printed in ET of 143 °C, it was insufficient for the longer size structures. No any dashed lines were seen on printing of multi-layered shell structure for the ET > 150 °C.
PS	While the any dashed line was not observed on printed sample for the PS of 100 and 150 mm/min. Blobs and dashed lines were occurred on the printed sample geometry due to the shear thinning behaviour of the Bi58Sn42 alloy at PS > 300.
EM	Uniformity on the extruded road's size was the best for the EM of 1. For the EM > 1, There was fluctuation on extruded road's size. Also, blobs occurred on the printed sample geometry.
RW	As the RW increased, the ooze also increased. Accordingly, the printing process was adversely affected. While there was ooze in ET of 143 °C for the RW of 1.02 mm, ooze was not observed for the RW of 0.4 and 0.66 mm until the 200 °C.
IR	The densest structure was printed with the combination of the EM of 2 and IR of 100 %. But, LT of the printed single-layer solid circle was varied between 0.2 mm and 0.9 mm as the EM > 1. On the other hand for the lower EM and IR combinations, dense structure couldn't be printed.

Printing mode	Printing in vase mode gave better results according to printing in start-stop mode. Uninterrupted uniform extruded road size was formed as the cohesive bond between the deposited road and melt inside the nozzle was not broken in vase mode. However , this uniformity was not obtained for the sample that had sharp turning geometric features since the acceleration and deceleration in these regions caused fluctuation in extruded road's size.
---------------	--

4.4. The performance evaluation of the 3D printed mold in low volume sheet metal part production

The diameter of the 3D printed male hemisphere mold in Fig. 4.48 was measured as 9.032 mm using a coordinate measurement machine (CMM) before starting the press forming operation. Then the female mold was cast as mentioned in section 3.3.3, and a press forming operation was commenced for forming the 0.2 mm AL 8006 sheets. However, the sheet metal forming process couldn't be performed as the molds did not fit perfectly. The reason was that the 3 mm probe of the CMM could not fully grip the sphere's base. Therefore, diameter measurement was remade using a digital caliper with a precision of 10 microns, and 3D printed male sphere mold's diameter was measured as 10.68 mm. Accordingly, female mold was recast, and the press forming operation was performed for forming the 0.2 mm AL 8006 sheets. Diameter of the cast female mold was measured as 11.08 mm. The shrinkage rate was 0.18 percent. After completing the 101 pressing operations, 3D printed male sphere mold's diameter was measured as 10.54 mm. Thus, the maximum deviation in the 3D printed hemisphere mold's diameter was 0.14 mm. In addition, measurements were taken from the 10th, 20th, 30th, 40th, 50th...100th formed sheet metal components with the increment of 10 , and 101st AL8006 sheets shaped in pressing operation and presented in Fig. 4.50. Maximum deviation among the shaped 0.2 mm thick sheet metal parts was 0.15 mm as seen from Fig. 4.50.

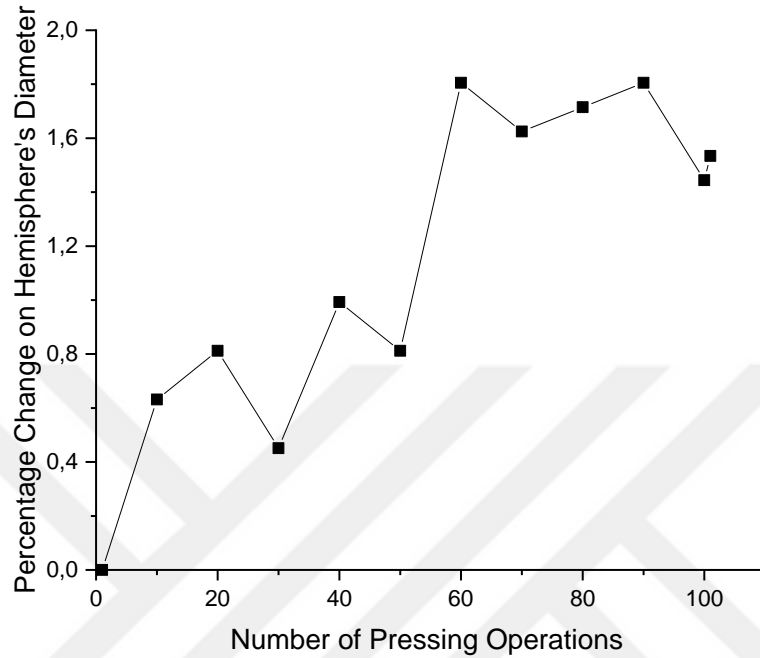


Figure 4.50. Deviation in the stamped 0.2 mm thickness Aluminum 8006 sheets' diameter

The press forming operation was continued for forming the 0.3 mm AL 8006. Again, a female semi-sphere mold was cast according to the 10.54 mm diameter 3D printed male hemisphere mold as mentioned in section 3.3.3. Diameter of the cast female mold was measured as 11.14 mm. The shrinkage rate was 0.089 percent. After completing the 101 pressing operations, 3D printed male sphere mold's diameter was measured as 10.12 mm. Therefore, the maximum deviation in the 3D printed hemisphere mold's diameter was 0.42 mm. Also, measurements were taken from the 10th, 20th, 30th, 40th, 50th, 100th, with the increment of 10 and 101st AL8006 sheets shaped in pressing operation and presented in Fig. 4.51. Maximum deviation among the shaped 0.3 mm thick sheet metal parts was 0.41 mm as seen from Fig. 4.51.

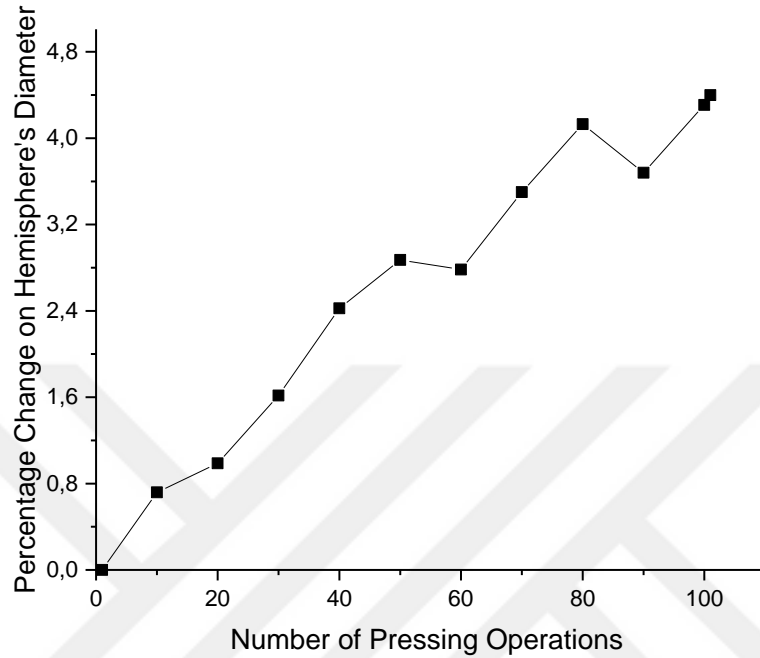


Figure 4.51. Deviation in the stamped 0.3 mm thickness Aluminum 8006 sheets' diameter

The purpose of the study was production of sheet metal forming mold for low volume sheet metal parts production using open source desktop type FDM 3D printer. Thus, it was aimed to realize inexpensive and fast mold production.

Total deviation on the 3D printed hemisphere mold's diameter was 0.56 mm after 101 pressing operations performed to shape 0.2 and 0.3 mm thick Aluminum 8006 sheets. The 3D printed sheet metal forming mold experimentally proved to be adequate for low volume sheet metal parts production. The sheet metal formed components were illustrated in Fig. 4.52.



Figure 4.52. Sheet metal formed components



5. CONCLUSION

In this study, a sheet metal forming mold was 3D printed using the Additive Manufacturing (AM) methodology, and then the performance of the 3D printed sheet metal forming mold was evaluated for low volume sheet metal parts production.

The Fused Deposition Modelling (FDM) method has been used in mold production as it is less costly and allows customization among the existing AM methods.

However, the limited heating power in the FDM system is applicable for the printing of materials with a low melting point. For this reason, Bi58Sn42 eutectic alloy, which has both low melting point and required strength to shape sheet metal plate, was found suitable for utilizing in this study.

Similar studies in the literature made to print fusible (low melting point) alloys using FDM type 3D printers, were explored. Customizations made in hardware and optimizations in software (print settings) were examined. Accordingly, the method that will be applied during the printing experiments for the production of sheet metal forming mold was determined.

Printing experiments were performed for the 3D printing of sheet metal forming mold using both standard extruder and customized extruder. The customizations made on the available FDM system were presented in detail at section 3.2.

The printing experiments were initiated to print simple line and maze shapes by optimizing print settings such as extrusion temperature (ET), printing speed (PS), extrusion multiplier (EM) and the experiments were continued until the 3D solid mold is built.










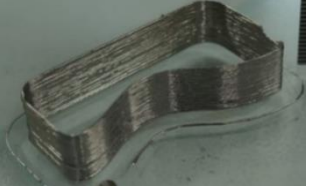
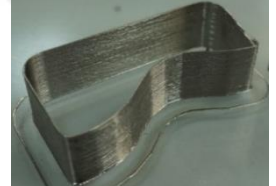
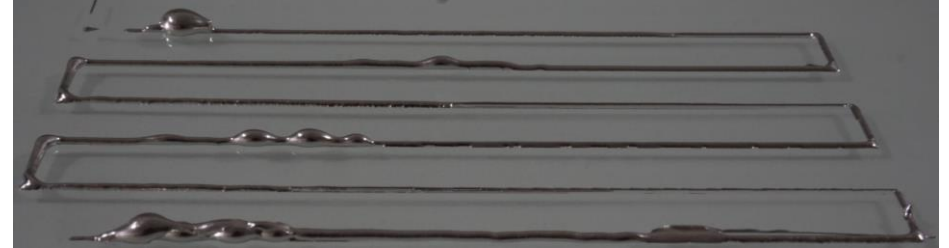


The printing experiments showed that the best surface quality was obtained using standard extruder in vase mode for layer thickness of 0.2 mm, printing speed of 100 mm/min, extrusion multiplier of 1, extrusion temperature of 160 °C, platform temperature of 75 °C, and road width of 0.4 mm. Therefore, solid dense structure

was tried to be printed in the same print settings using standard extruder. However, the desired solid object couldn't be printed. Main reasons were presented in table 5.1.

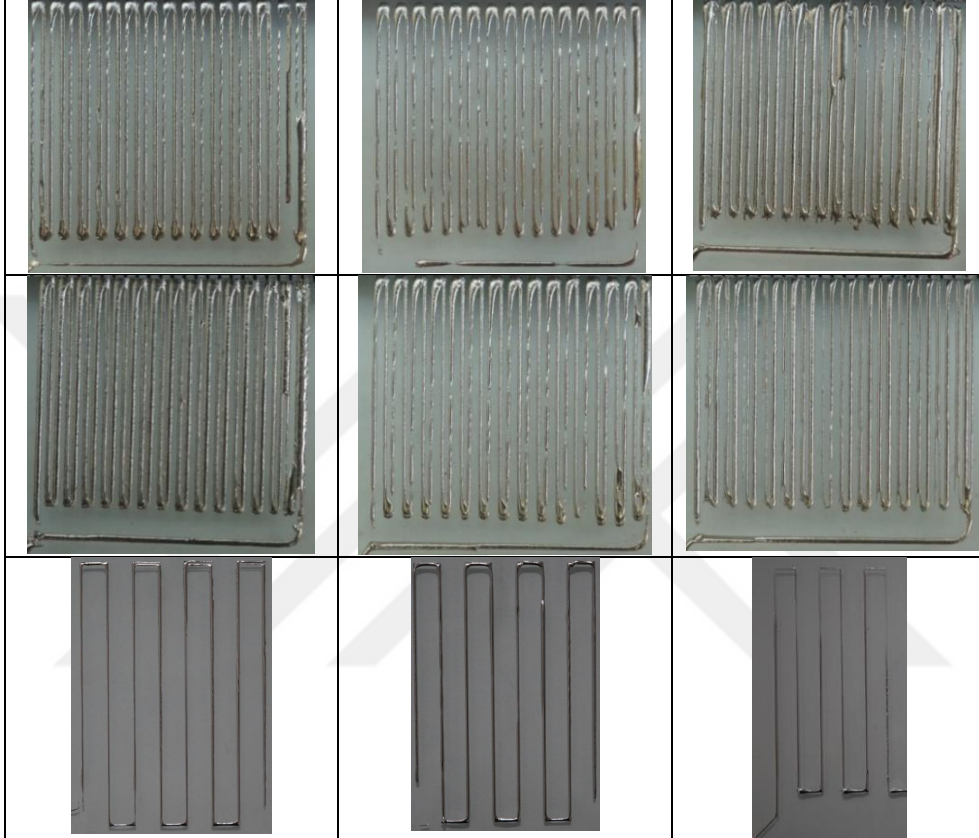
Similar result was also observed in customized extruder too. Print quality was better during the printing of an object in vase mode. But it was getting worse for the printing of solid objects. The problems experienced in customized extruder as in standard extruder can be seen in table 5.1.

In addition, during the printing experiments performed for extrusion multiplier (EM) > 1 and (PS) > 150 mm/min using both standard and customized extruders, dash lines and blobs were formed. The reason for this can be explained by low viscosity of the Bi58Sn42 alloy.

Table 5.1. Issues experienced during the performed printing trials

Issue 1 (Eutectic phase and low viscosity): Deposited (solidified) road doesn't maintain its shape. It fuses with the newly deposited road. For this reason, dimensional accuracy and surface roughness of the 3D printed parts are adversely affected.			
			
			
Issue 2 (No pressure drop feedback in the extruder): Deviations on the extruded road's size affected the printed part's quality due to the inability to control the pressure within the nozzle in the FDM system. Therefore, the final parts obtained in repeated 3D printing experiments using the same print settings are not uniform.			
			
			
			

Issue 3 (Deviations in extruded road's size during the extruder's sharp turning movements): Depending on the part geometry, the change in printing speed (acceleration or deceleration) causes deviations in the extruded road's size during the extruder's sharp turning movements.



While no solution is available for issue 1 (Eutectic phase and low viscosity) and 2 (No pressure drop feedback in the extruder) mentioned in Table 5.1, partial solution is possible for issue 3 (Deviations in extruded road's size during the extruder's sharp turning movements). As minimizing the extruder's sharp turning movements can decrease deviation in extruded road's size, a circular object that doesn't involve any sharp turning geometric feature tried to be printed. In this context a male hemisphere mold with concentric infill pattern was 3D printed from Bi58Sn42 alloy filament using the customized open-source desktop type FDM 3D

printer that is originally developed for printing of polymer materials such as ABS, PLA and etc.

On the other hand, the female hemisphere mold required to shape sheet metals was produced by casting as mentioned in section 3.3.3 due to the FDM hardware's low reliability (no pressure drop feedback in the extruder) and poor material characteristics of Bi58Sn42 alloy (eutectic phase and low viscosity) adversely affected the printing of the Bi58Sn42 alloy.

After mounting the produced molds (3D printed male hemisphere mold and cast female hemisphere mold) into the Instron 8801 axial fatigue test device, pressing process was applied 101 times on aluminum 8006 sheets with a thickness of both 0.2 mm and 0.3 mm, respectively. While the deviation in 3D printed hemisphere mold's diameter was 0.14 mm for 0.2 mm thick aluminum sheets, it was 0.42 mm for 0.3 mm thick aluminum sheets. The performance of the 3D printed mold was sufficient for low volume sheet metal parts production. However, as explained above, printability of the Bi58Sn42 alloy undermines the reliability of the proposed sheet metal forming mold production methodology. Hence, following topics can be considered for future studies in FDM type 3D printers;

- Metallic glasses can be researched for applications require high strength. They are more suitable candidates as a filament material for 3D printing since their flow behavior similar to polymer materials or composite filaments that involve binder and metal powder can be developed then secondary processes such as debinding and sintering are performed to obtain fully dense metal parts.
- Alternative polymer filaments like unfilled polyetherimide (ULTEM), Polycarbonate (PC) that have high strength can be synthesized.



REFERENCES

- Afroze, M.F., Masood, S., Iovenitti, P., Nikzad, M. and Sbarski, I. (2016), "Effects of part build orientations on fatigue behaviour of FDM-processed PLAmaterial", *Progress in Additive Manufacturing*, Vol. 1 Nos 1/2, pp. 21-28, doi: 10.1007/s40964-015-0002-3
- Agarwala, M. K., Bandyopadhyay, A., Weeren, R. V., Langrana, N. A., Safari, A., Danforth, S. C., ... & Pollinger, J. (1996b). Fused deposition of ceramics (FDC) for structural silicon nitride components. In 1996 International Solid Freeform Fabrication Symposium
- Agarwala, M. K., Jamalabad, V. R., Langrana, N. A., Safari, A., Whalen, P. J., & Danforth, S. C. (1996a). Structural quality of parts processed by fused deposition. *Rapid Prototyping Journal*, 2(4), 4–19. <https://doi.org/10.1108/13552549610732034>
- Agarwala, M. K., Van Weeren, R., & Bandyopadhyay, A. (1996c). Fused deposition of ceramics and metals: an overview. *Proceedings of Solid Freeform Fabrication Symposium*, 385–392. Retrieved from <https://sffsymposium.engr.utexas.edu/Manuscripts/1996/1996-47-Agarwala.pdf>,
- Agarwala, M. K., Van Weeren, R., Vaidyanathan, R., Bandyopadhyay, A., Carrasquillo, G., Jamalabad, V., ... Ballard, C. (1995). Structural Ceramics by Fused Deposition of Ceramics. *Solid Freeform Fabrication Symposium*, 1–8
- Agarwala, M. K., Weeren, R. V., Bandyopadhyay, A., Safari, A., Danforth, S. C., & Priedeman, W. R. (1996d). Filament Feed Materials for Fused Deposition Processing of Ceramics and Metals. *Proceedings Ofthe Solid Freeform Fabrication Symposium*, 712, 451–458. Retrieved from <https://sffsymposium.engr.utexas.edu/Manuscripts/1996/1996-53-Agarwala.pdf>

- Anitha, R., Arunachalam, S., & Radhakrishnan, P. (2001). Critical parameters influencing the quality of prototypes in fused deposition modelling. In *Journal of Materials Processing Technology* (Vol. 118, pp. 385–388). [https://doi.org/10.1016/S0924-0136\(01\)00980-3](https://doi.org/10.1016/S0924-0136(01)00980-3)
- Annoni, M., Giberti, H., & Strano, M. (2016). Feasibility Study of an Extrusion-based Direct Metal Additive Manufacturing Technique. *Procedia Manufacturing*, 5, 916–927. <https://doi.org/10.1016/j.promfg.2016.08.079>
- Anonymous (1981). "The alternatives to conventional tool making. Low melt alloys cut press tool costs." *Production Engineer* 60(12): 32.
- Arif, M. F., Kumar, S., Varadarajan, K. M., & Cantwell, W. J. (2018). Performance of biocompatible PEEK processed by fused deposition additive manufacturing. *Materials & Design*, 146, 249-259,
- Attaran, M. (2017). "The rise of 3-D printing: The advantages of additive manufacturing over traditional manufacturing." *Business Horizons* 60(5): 677-688.
- Bagherifard, S., Beretta, N., Monti Riccio, M., Bandini, M., & Guagliano, M. (2018)., S., On the fatigue strength enhancement of additive manufactured AlSi10Mg parts by mechanical and thermal post-processing. *Materials & Design*, 145, 28-41.
- Bandyopadhyay, A., Das, K., Marusich, J., & Onagoruwa, S. (2006). Application of fused deposition in controlled microstructure metal-ceramic composites. *Rapid Prototyping Journal*, 12(3), 121–128. <https://doi.org/10.1108/13552540610670690>
- Bandyopadhyay, A., Gualtieri, T. P., & Bose, S. (2015). Global engineering and additive manufacturing. *Additive Manufacturing*, 1, 9-11.
- Baumers, M., Dickens, P., Tuck, C., & Hague, R. (2016). The cost of additive manufacturing: machine productivity, economies of scale and technology-push. *Technological forecasting and social change*, 102, 193-201.

- Bellehumeur, C., Li, L., Sun, Q., & Gu, P. (2004). Modeling of bond formation between polymer filaments in the fused deposition modeling process. *Journal of manufacturing processes*, 6(2), 170-178.
- Bryden, B. G., Pashby, I. R., Wimpenny, D. I., & Adams, C. (2000). Laminated steel tooling in the aerospace industry. *Materials & Design*, 21(4), 403-408.
- Cantrell, J.T.S., Rohde, D., Damiani, R., Gurnani, L., DiSandro, J., Anton, A., Young, A., Jerez, D., Steinbach, C. and Kroese, (2017). Experimental characterization of the mechanical properties of 3D-printed ABS and polycarbonate parts. *Rapid Prototyping Journal*, Vol. 23No. 4, pp. 811-824, doi: 10.1108/RPJ-03-2016-0042
- Carneiro, O. S., Silva, A. F., & Gomes, R. (2015). Fused deposition modeling with polypropylene. *Materials & Design*, 83, 768-776,
- Chacón, J. M., Caminero, M. A., García-Plaza, E., & Núñez, P. J. (2017). Additive manufacturing of PLA structures using fused deposition modelling: Effect of process parameters on mechanical properties and their optimal selection. *Materials & Design*, 124, 143-157.,
- Chen, W., Thornley, L., Coe, H. G., Tonneslan, S. J., Vericella, J. J., Zhu, C., ... & Pascall, A. J. (2017). Direct metal writing: Controlling the rheology through microstructure. *Applied Physics Letters*, 110(9), 094104
- Chohan, J. S., & Singh, R. (2017). Pre and post processing techniques to improve surface characteristics of FDM parts: A state of art review and future applications. *Rapid Prototyping Journal*. Emerald Group Publishing Ltd. <https://doi.org/10.1108/RPJ-05-2015-0059>
- Cohen, A., Chen, R., Frodis, U., Wu, M. T., & Folk, C. (2010). Microscale metal additive manufacturing of multi-component medical devices. *Rapid Prototyping Journal*, 16(3), 209–215. <https://doi.org/10.1108/13552541011034889>
- Cunico, M. W. M., & De Carvalho, J. (2013). Optimization of positioning system of FDM machine design using analytical approach. *Rapid Prototyping Journal*

- Daalkhaijav, U., Yirmibesoglu, O. D., Walker, S., & Mengüç, Y. (2018). Rheological Modification of Liquid Metal for Additive Manufacturing of Stretchable Electronics. *Advanced Materials Technologies*, 3(4). <https://doi.org/10.1002/admt.201700351>
- Desai, B. V., et al. (2014). Die-Less rapid prototyping process: Parametric investigations. *Procedia materials science* 6: 666-673.
- Durgun, I., Kus, A., Sakin, A., Unver, E., Jagger, B., Doruk, E., & Findık, F. (2016). Experimental investigation of sheet metal forming using a recyclable low melting point alloy tool. *Materials Testing*, 58(5), 475-480.
- Durgun, I.R. and Ertan, (2014), “Experimental investigation of FDM process for improvement of mechanical properties and production cost”, *Rapid Prototyping Journal*, Vol. 20 No. 3, pp. 228-235, doi: 10.1108/RPJ-10-2012-0091
- Fang, X., Du, J., Wei, Z., He, P., Bai, H., Wang, X., & Lu, B. (2017). An investigation on effects of process parameters in fused-coating based metal additive manufacturing. *Journal of Manufacturing Processes*, 28, 383–389. <https://doi.org/10.1016/j.jmapro.2017.01.008>
- Fang, X., Du, J., Wei, Z., He, P., Bai, H., Wang, X., & Lu, B. (2017). An investigation on effects of process parameters in fused-coating based metal additive manufacturing. *Journal of Manufacturing Processes*, 28, 383–389. <https://doi.org/10.1016/j.jmapro.2017.01.008>
- Fernandez-Vicente, M., Calle, W., Ferrandiz, S., & Conejero, A. (2016). Effect of infill parameters on tensile mechanical behavior in desktop 3D printing. *3D printing and additive manufacturing*, 3(3), 183-192
- Finke, S., & Feenstra, F. K. (2002). Solid freeform fabrication by extrusion and deposition of semi-solid alloys. *Journal of Materials Science*, 37(15), 3101–3106. <https://doi.org/10.1023/A:1016137723481>

- Gao, W., Zhang, Y., Ramanujan, D., Ramani, K., Chen, Y., Williams, C. B., ... & Zavattieri, P. D. (2015). The status, challenges, and future of additive manufacturing in engineering. *Computer-Aided Design*, 69, 65-89.
- Garzon-Hernandez, S., Garcia-Gonzalez, D., Jérusalem, A., & Arias, A. (2020). Design of FDM 3D printed polymers: An experimental-modelling methodology for the prediction of mechanical properties. *Materials & Design*, 188, 108414.
- Gebhardt, A. (2011). Understanding additive manufacturing.
- Gibson, I., Rosen, D. W., & Stucker, B. (2010). Additive manufacturing technologies: Rapid prototyping to direct digital manufacturing. *Additive Manufacturing Technologies: Rapid Prototyping to Direct Digital Manufacturing* (pp. 1–459). Springer US. <https://doi.org/10.1007/978-1-4419-1120-9>
- Gibson, I., Rosen, D. W., Stucker, B., & Khorasani, M. (2021). Additive manufacturing technologies (Vol. 17). Cham, Switzerland: Springer.
- Gibson, M. A., Mykulowycz, N. M., Shim, J., Fontana, R., Schmitt, P., Roberts, A., ... Schroers, J. (2018). 3D printing metals like thermoplastics: Fused filament fabrication of metallic glasses. *Materials Today*, 21(7), 697–702. <https://doi.org/10.1016/j.mattod.2018.07.001>
- Gilmer, E. L., Miller, D., Chatham, C. A., Zawaski, C., Fallon, J. J., Pekkanen, A., ... & Bortner, M. J. (2018). Model analysis of feedstock behavior in fused filament fabrication: Enabling rapid materials screening. *Polymer*, 152, 51-61.
- Gleadall, A., Visscher, D., Yang, J., Thomas, D., & Segal, J. (2018). Review of additive manufactured tissue engineering scaffolds: relationship between geometry and performance. *Burns & Trauma*, 6. <https://doi.org/10.1186/s41038-018-0121-4>
- Gnanasekaran, K., Heijmans, T., Van Bennekom, S., Woldhuis, H., Wijnia, S., de With, G., & Friedrich, H. (2017). 3D printing of CNT-and graphene-based

- conductive polymer nanocomposites by fused deposition modeling. *Applied materials today*, 9, 21-28
- Greul, M., Pintat, T., & Greulich, M. (1995). Rapid prototyping of functional metallic parts. *Computers in Industry*, 28(1), 23–28. [https://doi.org/10.1016/0166-3615\(95\)00028-5](https://doi.org/10.1016/0166-3615(95)00028-5)
- Groover, M. P. (2012). *Fundamentals of modern manufacturing: materials, processes, and systems*. John Wiley & Sons.
- H. Li, T. Wang, J. Sun, Z. Yu, The effect of process parameters in fused deposition modelling on bonding degree and mechanical properties, *Rapid Prototyp. J.* 24 (1) (2018) 80–92 <https://doi.org/10.1108/RPJ-06-2016-0090>
- H. Valkenaers , F. Vogeler , A. Voet , J.P. Kruth, 2013.” Screw Extrusion Based 3D Printing, a Novel Additive Manufacturing Technology”, *International Conference on Competitive Manufacturing*
- Harris, M., Potgieter, J., Archer, R., & Arif, K. M. (2019, May 1). Effect of material and process specific factors on the strength of printed parts in fused filament fabrication: A review of recent developments. *Materials*. MDPI AG. <https://doi.org/10.3390/ma12101664>
- Herzog, D., Seyda, V., Wycisk, E., & Emmelmann, C. (2016). Additive manufacturing of metals. *Acta Materialia*, 117, 371-392.
- Iancu, C., Iancu, D., & Stăncioiu, A. (2010). FROM CAD MODEL TO 3D PRINT VIA " STL" FILE FORMAT. *Fiability & Durability/Fiabilitate si Durabilitate*, (1).
- J. Torres, M. Cole, A. Owji, Z. DeMastry, A.P. Gordon, An approach for mechanical property optimization of fused deposition modeling with polylactic acid via design of experiments, *Rapid Prototyp. J.* 22 (2) (2016) 387–404
- Jabbari, A., & Abrinia, K. (2018). A metal additive manufacturing method: semi-solid metal extrusion and deposition. *International Journal of Advanced Manufacturing Technology*, 94(9–12), 3819–3828. <https://doi.org/10.1007/s00170-017-1058-7>

- Jibin, Z. (2005, December). Determination of optimal build orientation based on satisfactory degree theory for RPT. In Ninth International Conference on Computer Aided Design and Computer Graphics (CAD-CG'05) (pp. 6-pp). IEEE.
- Kamal, M., Mazen, S., Bakr El-Bediwi, A., & Kashita, E. (2006). Microstructure, electrical, mechanical and thermal properties of melt-spun bismuth–tin eutectic alloy. *Radiation Effects and Defects in Solids*, 161(2), 143-148
- Kimball E. Andersen, Optimization of a Low-melting Alloy for Fused Filament Fabrication (Master's Thesis) [Thesis in Canada]. 2015.
- Kumbhar, N. N., & Mulay, A. V. (2018). Post processing methods used to improve surface finish of products which are manufactured by additive manufacturing technologies: a review. *Journal of The Institution of Engineers (India): Series C*, 99(4), 481-487.
- Le Duigou, A., Castro, M., Bevan, R., & Martin, N. (2016). 3D printing of wood fibre biocomposites: From mechanical to actuation functionality. *Materials & Design*, 96, 106-114
- Leary, M., Merli, L., Torti, F., Mazur, M., & Brandt, M. (2014). Optimal topology for additive manufacture: A method for enabling additive manufacture of support-free optimal structures. *Materials & Design*, 63, 678-690
- Leary, M., Merli, L., Torti, F., Mazur, M., & Brandt, M. (2014). Optimal topology for additive manufacture: A method for enabling additive manufacture of support-free optimal structures. *Materials & Design*, 63, 678-690.
- Lee, T. M., Kang, T. G., Yang, J. S., Jo, J., Kim, K. Y., Choi, B. O., & Kim, D. S. (2008a). Gap adjustable molten metal DoD inkjet system with cone-shaped piston head. *Journal of manufacturing science and engineering*, 130(3).
- Lee, T. M., Kang, T. G., Yang, J. S., Jo, J., Kim, K. Y., Choi, B. O., & Kim, D. S. (2008b). Drop-on-demand solder droplet jetting system for fabricating microstructure. *IEEE Transactions on Electronics Packaging Manufacturing*, 31(3), 202-210.

- Leutenecker-Twelsiek, B., Klahn, C., & Meboldt, M. (2016). Considering part orientation in design for additive manufacturing. *Procedia Cirp*, 50, 408-413.
- Li, J., Xie, Z., Zhang, X., Zeng, Q., & Liu, H. (2010). Study of metal powder extrusion and accumulating rapid prototyping. In *Key Engineering Materials* (Vol. 443, pp. 81–86). <https://doi.org/10.4028/www.scientific.net/KEM.443.81>
- Liu, Z., Wang, Y., Wu, B., Cui, C., Guo, Y., & Yan, C. (2019, June 19). A critical review of fused deposition modeling 3D printing technology in manufacturing polylactic acid parts. *International Journal of Advanced Manufacturing Technology*. Springer London. <https://doi.org/10.1007/s00170-019-03332-x>
- Mahmood, S., Qureshi, A. J., Goh, K. L., & Talamona, D. (2017). Tensile strength of partially filled FFF printed parts: experimental results. *Rapid Prototyping Journal*
- Masood, S. H., & Song, W. Q. (2004). Development of new metal/polymer materials for rapid tooling using Fused deposition modelling. *Materials and Design*, 25(7), 587–594. <https://doi.org/10.1016/j.matdes.2004.02.009>
- Mazzanti, V., Malagutti, L., & Mollica, F. (2019). FDM 3D printing of polymers containing natural fillers: A review of their mechanical properties. *Polymers*. MDPI AG. <https://doi.org/10.3390/polym11071094>
- Melgoza, E. L., Vallicrosa, G., Serenó, L., Ciurana, J., & Rodríguez, C. A. (2014). Rapid tooling using 3D printing system for manufacturing of customized tracheal stent. *Rapid Prototyping Journal*, 20(1), 2–12. <https://doi.org/10.1108/RPJ-01-2012-0003>
- Mireles, J., Espalin, D., Roberson, D., Zinniel, B., Medina, F., & Wicker, R. (2012). Fused deposition modeling of metals. In *23rd Annual International Solid Freeform Fabrication Symposium - An Additive Manufacturing Conference, SFF 2012* (pp. 836–845). University of Texas at Austin (freeform).

- Mireles, J., Kim, H.-C., Hwan Lee, I., Espalin, D., Medina, F., MacDonald, E., & Wicker, R. (2013). Development of a Fused Deposition Modeling System for Low Melting Temperature Metal Alloys. *Journal of Electronic Packaging*, 135(1), 11008. <https://doi.org/10.1115/1.4007160>
- Müller, H., & Sladojevic, J. (2001). Rapid tooling approaches for small lot production of sheet-metal parts. *Journal of Materials Processing Technology*, 115(1), 97-103.
- Nasr, E. S. A., Al-Ahmari, A., & Moiduddin, K. (2014). CAD Issues in Additive Manufacturing. In *Comprehensive Materials Processing* (Vol. 10). <https://doi.org/10.1016/B978-0-08-096532-1.01015-3>
- Nikzad, M., Masood, S. H., & Sbarski, I. (2011). Thermo-mechanical properties of a highly filled polymeric composites for Fused Deposition Modeling. *Materials and Design*, 32(6), 3448–3456. <https://doi.org/10.1016/j.matdes.2011.01.056>
- Peng, A., Xiao, X., & Yue, R. (2014). Process parameter optimization for fused deposition modeling using response surface methodology combined with fuzzy inference system. *The International Journal of Advanced Manufacturing Technology*, 73(1-4), 87-100
- Pinto, M., Santos, A. D., Teixeira, P., & Bolt, P. J. (2008). Study on the usability and robustness of polymer and wood materials for tooling in sheet metal forming. *Journal of Materials Processing Technology*, 202(1-3), 47-53.
- Rahmati, S. (2014). Advances in Additive Manufacturing and Tooling. *Compr. Mater. Process*, 10, 303-344.
- Ramanath, H. S., Chua, C. K., Leong, K. F., & Shah, K. D. (2008). Melt flow behaviour of poly-ε-caprolactone in fused deposition modelling. *Journal of Materials Science: Materials in Medicine*, 19(7), 2541-2550
- Rane, K., & Strano, M. (2019). A comprehensive review of extrusion-based additive manufacturing processes for rapid production of metallic and ceramic parts. *Advances in Manufacturing*, 1-19

- Rankouhi, B.S., Javadpour, F., Delfanian, T. and Letcher, (2016), “Failure analysis and mechanical characterization of 3D printed ABS with respect to layer thickness and orientation”, *Journal of Failure Analysis and Prevention*, Vol.16 No. 3, pp. 467-481, doi: 10.1007/s11668-016-0113-2
- Ren, L., Zhou, X., Song, Z., Zhao, C., Liu, Q., Xue, J., & Li, X. (2017). Process parameter optimization of extrusion-based 3D metal printing utilizing PW-LDPE-SA binder system. *Materials*, 10(3). <https://doi.org/10.3390/ma10030305>
- Rezayat, H.W., Zhou, A., Siriruk, D., Penumadu, S. and Babu, (2015), “Structure–mechanical property relationship in fused deposition modelling”, *Materials Science and Technology*, Vol.31 No. 8, pp. 895-903., doi: 10.1179/1743284715Y.0000000010
- Rinaldi, M., Ghidini, T., Cecchini, F., Brandao, A., & Nanni, F. (2018). Additive layer manufacturing of poly (ether ether ketone) via FDM. *Composites Part B: Engineering*, 145, 162-172
- Rosochowski, A., & Matuszak, A. (2000). Rapid tooling: the state of the art. *Journal of materials processing technology*, 106(1-3), 191-198.
- Ryder, M. A., Lados, D. A., Iannacchione, G. S., & Peterson, A. M. (2018). Fabrication and properties of novel polymer-metal composites using fused deposition modeling. *Composites Science and Technology*, 158, 43–50. <https://doi.org/10.1016/j.compscitech.2018.01.049>
- S. Scott Crump, APPARATUS AND METHOD FOR CREATING THREE-DIMENSIONAL OBJECTS, US Patent, Jun. 9, 1992, US 5 121 329.
- Sabourin, E., Houser, S. A., & Bøhn, J. H. (1996). Adaptive slicing using stepwise uniform refinement. *Rapid Prototyping Journal*
- Sahu, R. K., Mahapatra, S. S., & Sood, A. K. (2013). A study on the dimensional accuracy of fused deposition modeling (FDM) processed parts using fuzzy logic. *Journal for Manufacturing Science & Production*, 13(3), 183-197.

- Singh, H., Sidhu, T. S., Kalsi, S. B. S., & Karthikeyan, J. (2013). Development of cold spray from innovation to emerging future coating technology. *Journal of the Brazilian Society of Mechanical Sciences and Engineering*, 35(3), 231-245
- Sood, A. K., Ohdar, R. K., & Mahapatra, S. S. (2010). Parametric appraisal of mechanical property of fused deposition modelling processed parts. *Materials & Design*, 31(1), 287-295
- Sood, A.K.R.K., Ohdar, S.S. and Mahapatra, (2010), "Parametric appraisal of mechanical property of fused deposition modelling processed parts", *Materials&Design*, Vol. 31No. 1, pp. 287-295, doi: 10.1016/j.matdes.2009.06.016.
- Tlegenov, Y., San Wong, Y., & Hong, G. S. (2017). A dynamic model for nozzle clog monitoring in fused deposition modelling. *Rapid Prototyping Journal*
- Turner, B. N., & Gold, S. A. (2015, April 20). A review of melt extrusion additive manufacturing processes: II. Materials, dimensional accuracy, and surface roughness. *Rapid Prototyping Journal*. Emerald Group Publishing Ltd. <https://doi.org/10.1108/RPJ-02-2013-0017>
- Turner, B. N., Strong, R., & Gold, S. A. (2014). A review of melt extrusion additive manufacturing processes: I. Process design and modeling. *Rapid Prototyping Journal*. Emerald Group Publishing Ltd. <https://doi.org/10.1108/RPJ-01-2013-0012>
- Vaezi, M., Drescher, P., & Seitz, H. (2020). Beamless Metal Additive Manufacturing. *Materials*, 13(4), 922
- Venkataraman, N., Rangarajan, S., Matthewson, M.J., Harper, B., Safari, A., Danforth, S.C., Wu, G., Langrana, N., Gucer, S. and Yardimci, A. (2000), "Feedstock material property-process relationships in fused deposition of ceramics (FDC)", *Rapid Prototyping Journal*, Vol. 6, pp. 244-252

- Vyavahare, S., Teraiya, S., Panghal, D., & Kumar, S. (2020, January 6). Fused deposition modelling: a review. *Rapid Prototyping Journal*. Emerald Group Publishing Ltd. <https://doi.org/10.1108/RPJ-04-2019-0106>
- Wang, L., & Liu, J. (2014). Compatible hybrid 3D printing of metal and nonmetal inks for direct manufacture of end functional devices. *Science China Technological Sciences*, 57(11), 2089–2095. <https://doi.org/10.1007/s11431-014-5657-3>
- Wang, T. M., Xi, J. T., & Jin, Y. (2007). A model research for prototype warp deformation in the FDM process. *International Journal of Advanced Manufacturing Technology*, 33(11–12), 1087–1096. <https://doi.org/10.1007/s00170-006-0556-9>
- Warrier, N., & Kate, K. H. (2018). Fused filament fabrication 3D printing with low-melt alloys. *Progress in Additive Manufacturing*, 3(1–2), 51–63. <https://doi.org/10.1007/s40964-018-0050-6>
- Website, 2012. <https://aml3d.com/technology/>. Accessed: 12/07/2020.
- Website, 2015. <https://fit.technology/content.php?newsid=273>. Accessed: 07/06/2015.
- Website, 2019a. <https://optomec.com/a-better-tool-for-3d-metal-repair/>. Accessed: 07/06/2019.
- Website, 2019b. <https://3dprintingindustry.com/news/u-s-army-develop-ultra-strong-3d-printed-steel-parts-to-revolutionize-battlefield-logistics-150367/>. Accessed: 07/06/2019.
- Website, 2019c. https://www.army.mil/article/217433/3d_printing_technology_enhancing_logistics_for_army. Accessed: 07/06/2019.
- Website, 2019d. <http://rokithealthcare.com/manual/>. Accessed: 02/12/2021.
- Website, 2020a. <https://www.lboro.ac.uk/research/amrg/about/the7categoriesofadditivemanufacturing/>. Accessed: 04/28/2020.

Website, 2020b. <https://www.3dhubs.com/knowledge-base/additive-manufacturing-technologies-overview/>. Accessed: 04/28/2020.

Website, 2020c. <https://www.additively.com/en/learn-about/stereolithography>. Accessed: 04/28/2020.

Website, 2020d. <https://www.custompartnet.com/wu/fused-deposition-modeling>. Accessed: 04/28/2020.

Website, 2020e. <https://xjet3d.com/technology/>. Accessed: 04/28/2020.

Website, 2020f. <https://add-man-tech.com/binder-jetting/>. Accessed: 04/28/2020.

Website, 2020g. <https://www.ge.com/additive/de/who-we-are/concept-laser>. Accessed: 04/28/2020.

Website, 2020h. <https://www.mazakeu.com/AM/>. Accessed: 04/28/2020.

Website, 2020i. <https://www.3diligent.com/prodex/technologies/3d-printing/directed-energy-deposition/>. Accessed: 04/28/2020.

Website, 2020j. <https://www.custompartnet.com/wu/laminated-object-manufacturing>. Accessed: 04/28/2020.

Website, 2020k. <https://fabrisonic.com/technology/>. Accessed: 12/07/2020.

Website, 2020l. <http://meldmanufacturing.com/technology-overview/>. Accessed: 12/07/2020.

Website, 2020m. <https://markforged.com/x7/>. Accessed: 12/08/2020.

Website, 2020n. <http://bootsindustries.com/the-importance-of-high-quality-3d-printer-filament/>. Accessed: 12/08/2020.

Website, 2020o. <https://www.stratasys.com/materials/search>. Accessed: 12/08/2020.

Website, 2020p. <https://www.desktopmetal.com/products/studio>. Accessed: 12/08/2020.

Website, 2020r. <https://www.desktopmetal.com/materials>. Accessed: 12/08/2020.

Website, 2020s. <https://markforged.com/materials>. Accessed: 12/08/2020.

Website, 2020t. <http://apt.mit.edu/am-process-comparisons>. Accessed: 04/28/2020.

- Website, 2020u. https://www.ronald-simmonds.de/wp-content/uploads/2018/03/20078101_Gesamtprospekt_Screen.pdf. Accessed: 04/28/2020.
- Website, 2021a. <https://www.5nplus.com/low-melting-point-alloys.html>. Accessed: 02/12/2021.
- Website, 2021b. <https://top3dshop.com/product/anycubic-405nm-clear-uv-resin-1l>. Accessed: 12/15/2021.
- Website, 2021c. <https://e3d-online.com/collections/nozzles>. Accessed: 02/12/2021.
- Website, 2021d. <https://www.emkoelektronik.com.tr/en/products/eco-pid>. Accessed: 12/15/2021.
- Website, 2021e. <https://www.simplify3d.com/>. Accessed: 02/12/2021.
- Website, 2021f. https://www.anycubic.com/products/anycubic-photon-s?_pos=12&_sid=6331daf49&_ss=r. Accessed: 12/15/2021.
- Website, 2021g. <https://wanhao.store/products/wanhao-curing-box>. Accessed: 12/15/2021.
- Website, 2021h. <https://www.instron.us/en-us/products/testing-systems/dynamic-and-fatigue-systems/servo-hydraulic-fatigue/8801---8802>. Accessed: 02/12/2021.
- Website, 2021i. <https://www.hexagonmi.com/tr-tr/products/portable-measuring-arms/romer-absolute-arm-compact>. Accessed: 02/12/2021.
- Website, 2021j. <https://www.simplify3d.com/support/print-quality-troubleshooting/layer-separation-and-splitting/>. Accessed: 03/12/2021.
- Wittbrodt, B.J.M. and Pearce, (2015), “The effects of PLA color on material properties of 3-D printed components”, *Additive Manufacturing*, Vol. 8, pp. 110-116, doi: 10.1016/j.addma.2015.09.006
- Wu, G., Langrana, N. A., Sadanji, R., & Danforth, S. (2002). Solid freeform fabrication of metal components using fused deposition of metals. *Materials and Design*, 23(1), 97–105. [https://doi.org/10.1016/s0261-3069\(01\)00079-6](https://doi.org/10.1016/s0261-3069(01)00079-6)

- Wu, G., Langrana, N., Rangarajan, S., Sadangi, R., Safari, A., & Danforth, S. C. (1998). Feasibility of Fabricating Metal Parts from 17-4PH Stainless Steel Powder. In Proceedings of Solid Freeform Fabrication Symposium (pp. 479–486)
- Yan, Y., Zhang, R., Hong, G., & Yuan, X. (2000). Research on the bonding of material paths in melted extrusion modeling. *Materials & Design*, 21(2), 93-99





CURRICULUM VITAE

He graduated from the Mechanical Engineering Department of Çukurova University in 2009. He started his Master of Science education in Mechanical Engineering Department of Çukurova University in 2009 and graduated in 2012. Later, he started his Doctor of Philosophy in the same department in 2013.

